DETAILED THIN-BEDDED FACIES ANALYSIS OF THE UPPER MANCOS SHALE, NEW MEXICO

By MATTHEW LEUNG, B.Sc. (Hons.)

A Thesis Submitted to the School of Graduate Studies in Partial Fulfilment of the Requirements

for the Degree Master of Science

McMaster University MASTER OF SCIENCE (2018) Hamilton, Ontario (School of Geography and Earth Sciences)

TITLE: Detailed Thin-bedded Facies Analysis of the Upper Mancos Shale, New Mexico

AUTHOR: Matthew Leung, Honours B.Sc. (McMaster University)

SUPERVISOR: Dr. Janok Bhattacharya

NUMBER OF PAGES CXXX: 130

Abstract

Our understanding of fine-grained sediment regarding the processes in which they are transported and deposited is rapidly evolving. However, developing a depositional model and characterizing the vertical variability within mud-dominated deposits has seldom been done. A 103m Upper Mancos Shale core retrieved from the San Juan Basin, New Mexico was analysed with detailed thin-bedded facies analysis to observe vertical variability in lithology, sedimentary structures, bioturbation intensity, and depositional processes. Lithological variation suggests there are 3 full sequences, 9 system tracts, and 92 parasequences. Facies observed revealed multiple facies successions indicating depositional processes including ignitive turbidite, storms (tempestite), wave enhanced sediment gravity flows (WESGFs), tidal, biogenic reworking, fluid mud, suspension settling, and general bedload transport. Relationships between lithology, bioturbation intensity, sedimentary structures and depositional processes were observed to be interrelated in that energetic processes (i.e., storms, ignitive turbidite) were associated with coarser deposits and low bioturbation intensity; whereas lower energy processes (i.e., biogenic reworking, suspension settling, WESGFs) were associated with finer deposits and relatively higher bioturbation intensities. Furthermore, lithological variability integrated with depositional models indicated temporal changes in environment of deposition across shelf.

Acknowledgments

First and foremost, I would like to thank my research supervisor, Dr. Janok Bhattacharya for his guidance and support throughout this project. The care he has for his students is well demonstrated by his willingness to help, especially during the many edits this paper needed to go through. Furthermore, I am truly grateful for all the field work and conference opportunities he had provided me.

I would like to thank the McMaster Sedimentological Research team. Each and everyone one of you had helped me in some way, shape, or form. Special thanks to Nick Randazzo and Cristina Genovese for assisting me collect the data that I needed for this project.

I would also like to thank the staff at New Mexico Bureau of Geology and Mineral Resources in Socorro, New Mexico. Specifically, I would like to thank Ron Broadhead and Annabelle Lopez for their continual support during my stay there. Furthermore, I would like to thank the staff at the USGS core research center in Denver, Colorado, for providing me the cores for observation.

Finally I would like to thank my family and friends for providing endless support, especially during the times I needed it the most.

Table of Contents

1. Introduction..... 1-2

1.1 Objective..... 2

2. Geologic Background and Study Area..... 3-7
3. Methodology..... 8-15
3.1 Age and Stratigraphic Context..... 8
3.2 Thin-Bedded Facies Analysis..... 8-9
3.2.1 Identification of Core Properties..... 10-11
4. Facies and Facies Association Identification and Interpretation..... 16-52
4.1 Facies Identification and Observations..... 17-39
4.2 Facies Association Identification and Interpretation..... 40-49
4.3 Distinction between Depositional Processes and Sedimentary Structures..... 50-51
5. Results: Macro-, Meso-, Micro-scale Analysis..... 53-86
5.1 Macro-Scale Analysis..... 53-58
5.2 Meso-Scale Analysis..... 59-61
5.2.1 Parasequence Observations and Interpretation..... 61-77
5.3 Micro-Scale Analysis.....78-86
5.3.1 Photomicrograph Observations and Interpretations..... 79-86
6. Discussion..... 87-96
6.1 Identifying Vertical Variability from Integration of all Three Scales of Analysis. 87
6.1.1 Vertical Variability Indications from Well Log..... 87-88
6.2 Comparison to Other Thin-Bedded Facies Study..... 88-89
6.3 Comparison to Other Existing Depositional Models..... 90
6.4 Contribution to Debatable Topics..... 91
6.5 Cyclicity..... 92-93
6.6 Industry Implications..... 93-96

7. Conclusion..... 97-98

7. References..... 99-112

Appendix…… 113-130

List of Figures

Figure 1: A). Middle Turonian paleogeographic map showing the maximum extent of the Western Interior Seaway (Blakey, 2014). B). Middle Coniacian paleogeographic map showing the Western Interior Seaway during the deposition of the Upper Mancos. The red star indicates location of core analysed in this study…….…….……...….4

Figure 2: Stratigraphic column of the Mancos Shale in the San Juan Basin (taken from Broadhead, 2015) with ages interpreted using the time stratigraphic cross-section from Ridgley et al. (2013).)……...…….……..……..6

Figure 3: A). Plan view map of New Mexico, including San Juan basin and location of the core shown as the red star. The short dashed line is the seaward extent of subaerial-plain deposits during the early Coniacian. The solid line is the landward extent of shoreline deposits during the early late Turonian. B). Close up plan view map of the San Juan basin. The blue lines highlight the county boundaries. The location of the core is shown by the red star (modified after Molenaar, 1983; Broadhead, 2015).……...….7

Figure 4. Photographs of the core from the Davis Federal 3 No. 15 well in Rio Arriba County, New Mexico. The base begins at 7416ft and the top ends at 7076ft. Parasequences examined are highlighted in the red boxes. Surfaces are marked by the red, blue and green lines, corresponding with the sequence boundary, transgressive surface and maximum flooding surface respectively……12

Figure 5: Well Log for Davis Fed Com. 3-15. Formations are separated by the thick red lines on the left, suggested by Broadhead (2015). Light blue rectangle shows the length of the core examined in this study. The thin red, blue, and green lines on the well log corresponds to the

sequence boundary, transgressive surface and maximum flooding surface respectively. System tract interpretation is on the right.……..……13

Figure 6: Macro-scale analysis of the core, including a stratigraphic log, identified parasequences, marked by zig-zag lines, lithology graphic log, BI log, lithofacies column, and a system tract column. Parasequences examined are marked by red lines with a labeled "P#" in between. The thin red, blue, and green lines transecting the columns correspond to the sequence boundary, transgressive surface and maximum flooding surface respectively. Sequences are shown by the red arrows on the right of each column. Link to figure is given below.…….14

Figure 7: Bed and lamina classification, defined by Campbell (1967). (taken from Passey et al., 2006).…… …… ……..……..15

Figure 8: Facies key with symbols and colours used for sedimentary structures, trace fossils, lithofacies, facies associations, and surfaces. The 11 facies in this study are also list.…….....16

Figure 9: Photographs highlighting structureless facies. A) Heterolithic with alternating sand and mud laminations. Structureless mud with *Planolites* burrows are found in between sand layers. Found at 7103.5ft B). Structureless mudstone bed at 7327ft. C). Structureless sandstone bed from 7086ft. D). Structureless mudstone lamination highlighted in white outline at 7123.25ft. E). Structureless sandstone beds highlighted in white outline at 7103.95ft…...…….19

Figure 10: Photographs highlighting bioturbated facies. A). Bioturbated sandy mudstone (BI:5) showing *Chondrities (Ch),Cylindricus (Cy), Planolites (Pl), Phycosiphon (Ph), Scolicia (Sc), Teichichnus (Te*), and *Zoophycos (Z)* trace fossils. Taken from 7351.50ft . B). A pervasively bioturbated sandy mudstone (BI:6). Taken from 71374.50ft. C). A pervasively bioturbated muddy sandstone (BI:6). Taken from 7341.30ft…….21

Figure 11: Examples of generic ripples. A). Thin starved ripples with asymmetrical crests and unobservable foresets, at 7315ft. Red arrows point to the generic ripples B). Starved ripple with an irregular crest and few observable foresets at 7147.95ft. C) Starved ripple with no observable foresets or laminations at 7136.20ft. Deformation of ripple crest and internal foresets renders it undistinguishable. Few *Planolites* burrows can be seen. A'-C'). Line drawings highlighting this faces in A-C respectively…….....23

Figure 12: Photographs highlighting wave rippled facies. Sole marks are shown by the red circles. A). Wave rippled lamination at 7137ft. B). Amalgamated wave ripple lamination at 7123.80ft. C). Amalgamated wave ripple bed at 7135ft At. D). Starved wave ripple laminations and wave ripple laminations at 7094.10ft E). Starved wave ripple lamination at 7207.99ft. F). Thin wavy laminations. A'-F') Line drawings of A-F respectively. Labelled red arrows point to features observed.……..25

Figure 13: Photographs highlighting combined-flow ripple facies A). Combined-flow ripple laminations with foresets dipping to the left at 7134.99ft. B). Starved combined-flow ripple laminations with foresets dipping to the left and right at 7094.05ft. C). Starved combined-flow ripple laminations with foresets dipping to the left and one dipping to the right at 7136.10ft. D). Starved combined-flow ripple laminations with foresets dipping to the left and one dipping to the right at 7134.80ft. E). Starved combined-flow rippled lamina with forests dipping to the left at 7136.80ft. F). Starved combined-flow ripple lamination with foresets dipping to the right at 7092.99ft……....28

Figure 14: Different combined-flow ripple profiles (taken from Dumas et al., 2005).……28

Figure 15: Photographs highlighting the different types of current rippled (CR) laminations seen in this study. A). Deposit with combined-flow rippled (CFR) laminations, CR laminations, generic rippled laminations and wavy laminae at 7092.50ft. CR shown have the conventional straight asymmetric ripple crests, and gently sloping stoss and steep lee sides. The respective line drawing highlights both current rippled (CR) laminations and combined-flow rippled (CFR) laminations B). Current rippled laminations with observable downlapping foresets and straight asymmetrical crest. Found at 7263.50ft. C). Compacted current rippled laminations, portraying scouring, low-angle downlapping foresets and straight asymmetrical crests. Found at 7318.60ft. The respective line drawing highlights the foresets and crests seen……..30

Figure 16: Photographs highlighting parallel laminations and normal grading with line drawings. A). Silt and very fine lower sand parallel planar laminations at 7263.70ft. B). Very fine lower sand and silt planar laminations with normal grading at 7225.20ft. Normally graded laminations are marked by the white triangles. C) Very fine lower sand and silt parallel planar laminations with normally graded laminations at 7225.20ft. Normal grading is marked by white triangles. D) Very fine lower generic ripples with one normally graded laminae marked by the white triangle at 7094.20ft. E) Very fine lower sand and silt parallel wavy laminations with normally graded laminations marked by the white triangles at 7181.10ft…….. 32

Figure 17: Photographs highlighting A). Relatively thick inoceramid fragments in structureless mudstone at 7230.40ft. B). A concentrated mass of inoceramid fragments found with silt and sand laminations at 7192.95ft C). Few thin inoceramid fragments found within silt laminations at 7229.90ft. D). A mixture of fossil fragments at 7208.50ft E) Massive bioturbated sandstones, cemented with calcium carbonate, and interbedded with thin wavy sand laminations. Generic sandy ripples occur within muddy intervals.....35

Figure 18: Photographs highlighting flaser and wavy bedding. A). Wavy bedding, showing bipolar current ripple orientations at 7091.90ft. B). Wavy flaser bedding. Showing double mud-drapes and bipolar current ripples at 7085.80ft.……...….37

Figure 19: Photographs highlighting bentonite ash layers A). A bentonite ash layer, sharply overlying silty and sandy parallel planar laminated mudstone at 7231.00ft. B). Fractured pieces of bentonite found at 7322.55ft……..39

Figure 20: Slope angles and potential offshore reach of processes for tempestites, wave/tide/current aided hyperpycnal flow, wave and current enhanced sediment gravity flows, and turbidites. Vertical red lines represent slope angles of seaway in this study from most proximal to distal (modified from Schieber, 2016).…… …….....41

Figure 21: Conceptualized model for the vertical succession of sedimentary structures in a wave-modified turbidite deposit, also known as a tempestite deposit. The model was observed in this study. Modified on the right are the depositional processes for associated sedimentary structures seen on the left (modified from Myrow et al., 2002)..……..42

Figure 22: Example and line drawing of a tempestite deposit showing from an upward succession a basal wave scour, wave rippled laminations, combined-flow ripple laminations, wavy lamina set, and normally graded lamination. Taken from 7137ft.....…43

Figure 23: Example of a WESGF deposit. Unit A exhibits combined-flow ripple cross lamination. Unit B has a wavy lamina set of intercalated silt and clay laminae. Unit C is a normally graded bed that is bioturbated (taken from Macquaker et al., 2010)….....……...44

Figure 24: Example of a WESGF deposit found in this study. A complete Macquaker et al. (2010) WESGF triplet facies succession is seen. Unit A, B and C are present…….45

Figure 25: A). Flaser bedding. B). Wavy bedding. C). Lenticular Bedding (modified after Reineck and Wunderlich, 1968).……...47

Figure 26: Example and line drawing of a tidal wavy bedding. Clear bipolar current ripple cross laminations can be seen. Taken from 7134.80'…..……...…47

Figure 27: The Bouma Sequence exhibiting normal grading. Divisions T_A, T_B, T_C, T_D, T_E can be seen. The additional TE subdivision as proposed by Piper (1978) is illustrated as subdivisions $T_{E-1,}$ T_{E-2}, and T_{E-3} (taken from Li et al., 2015)…… ……...……..49

Figure 28: A). Example of an ignitive turbidite deposit exhibiting the $T_{A,}$ $T_{C,}$ T_D Bouma divisions from 7085.00'…….……49

Figure 29: Chart summarizing facies associations interpreted for each facies seen in this study. Colours correspond to colours in facies key. ……...52

Figure 30: Depositional model for Tununk Shale in the CWIS. The four lithofacies observed in their study are assigned to a depositional environment across shelf. Calcareous content is shown to increases further basinward; whereas preservation potential of wave ripple and clastic dilution decreases. The green, yellow and blue arrows indicate LST, HST, and TST respectively in the core. The bottom represents the bottom of the core and top represents the top of the core. Chart portrays the change lithofacies and environment of deposition transition throughout the core within each system tract (modified after Li and Schieber, 2018). ……...….57

Figure 31: Depositional model of the CWIS. The red arrows show the processes that transport sediment across the seaway. The most proximal deposit (shoreline sandstone) is dominated by coarse grained siliciclastic sediments. The most proximal mudstone deposit (siliciclastic mudstone) is dominated by clay, silt, and quartz. Further offshore siliciclastic input decreases

and biogenic sediment increases forming calcareous mudstones. Marlstone and pelagic limestone are formed near the basincenter where biogenic production are highest. Marine organic matter (MOM) zones are labeled as 1-3, where 1 has low preservation potential for MOM, 2 have good MOM preservation potential, and 3 have low MOM content (taken from Hart, 2016).……. ….58

Figure 32: Chart summarizing the relative distribution in percentages of facies through each of the ten parasequences. The facies association for each facies is also included. The green, yellow and red indicate the primary, secondary, and tertiary facies observed, respectively…….62

Figure 33: Chart summarizing the relative distribution in percentages of facies association throughout each of the ten parasequences. The green, yellow and red indicate the dominant, influenced, and affected depositional process, respectively. Process classification is given, to show which processes dominated, influenced, or affected the deposition of the parasequence....66

Figure 34: Two ternary diagrams illustrating the classification of dominant depositional processes. Suspension settling, Biogenic reworking, and bedload transport are classified in the first ternary diagram. Bedload transport is further divided into generic, wave, and tidal processes……....67

Figure 35: Stratigraphic column, facies chart, facies association column, lithology graphic log, and BI log for parasequence 9. Sample 1 used for micro-scale analysis is highlighted by red bracket on the left. Parasequence 9 is from 7386’-7383’……..……..68

Figure 36: Stratigraphic column, facies chart, facies association column, lithology graphic log, and BI log for parasequence 21. Sample 2 used for micro-scale analysis is highlighted by red bracket on the left. Parasequence 21 is from 7344’-7340.05’……69

Figure 37: Stratigraphic column, facies chart, facies association column, lithology graphic log, and BI log for parasequence P24. Sample 2 used for micro-scale analysis is highlighted by red bracket on the left. Parasequence 24 is from 7334'-7331'…….……...70

Figure 38: Stratigraphic column, facies chart, facies association column, lithology graphic log, and BI log for parasequence 30. Sample 4 used for micro-scale analysis is highlighted by red bracket on the left. Parasequence 30 is from 7315.20'-7311.10'…….71

Figure 39: Stratigraphic column, facies chart, facies association column, lithology graphic log, and BI log for parasequence 33. Sample 5 (S5) used for micro-scale analysis is highlighted by red bracket on the left. Parasequence 33 is from 7303.15'-7300.05'……72

Figure 40: Stratigraphic column, facies chart, facies association column, lithology graphic log, and BI log for parasequence 43. Sample 6 used for micro-scale analysis is highlighted by red bracket on the left. Parasequence 43 is from 7264.30'7261.95.…….73

Figure 41: Stratigraphic column, facies chart, facies association column, lithology graphic log, and BI log for parasequence 54. Sample 7 used for micro-scale analysis is highlighted by red bracket on the left. Parasequence 54 is from 7208.95'-7206.10'….....74

Figure 42: Stratigraphic column, facies chart, facies association column, lithology graphic log, and BI log for parasequence 80. Sample 8 used for micro-scale analysis is highlighted by red bracket on the left. Parasequence 80 is from 7136.90'-7130.1...….....75

Figure 43: Stratigraphic column, facies chart, facies association column, lithology graphic log, and BI log for parasequence 88. Sample 9 used for micro-scale analysis is highlighted by red bracket on the left. Parasequence 88 is from 7100.50'-7090.90'…….76

Figure 44: Stratigraphic column, facies chart, facies association column, lithology graphic log, and BI log for parasequence 89. Sample 10 used for micro-scale analysis is highlighted by red bracket on the left. Parasequence 89 is from 7090.90'-7084.40'……. 77

Figure 45: Chart summarizing the three components with each abundance end member categorized in micro-scale analysis. The "H" represents "high abundance" and the "L" represents "low abundance". The "S", "C", and "D" represent "siliciclastic", "calcareous", and "diagenetic" respectively. The interpretation of each component and associated abundance is given on the right…….…….…..83

Figure 46: Chart summarizing the relative proportions of siliciclastic, calcareous, and diagenetic components in the samples examined in each parasequence. The relative position of the sampling within each parasequence is also noted. An interpretation of the shoreline migration relative to the first sample is given in the bottom row…….…...84

Figure 47: Sample 1. Plain light photomicrographs of a thin section in parasequence 9. A general view is at the top and detailed view is at the bottom.…….....85

Figure 48: Sample 2. Plain light photomicrographs of a thin section in parasequence 21. A general view is at the top and detailed view is at the bottom...…….....86

Figure 49: Example of facies observed in Li and Schieber (2018). The facies observed in their study are analogous to the ones observed in this study (taken from Li and Schieber, 2018)…....89

Figure 50: Graphical representation of TOC values throughout the core. The y-axis is the TOC value and x-axis is depth. TOC values sharply increase at 7269ft and gradually decreases correlated to decrease in depth. All data is provided by Weatherford Laboratories…….....96

1. Introduction

Our understanding of the processes that govern production, transport and deposition of sediment in mud-dominated systems has been rapidly evolving over the past decade. It is well established that muds do not exclusively deposit in quiescent waters as previously thought (e.g. Mutti, 1977; Potter et al., 2005), but also in waters with flow velocities similar to velocities that transport sands (Schieber, 2007; Schieber and Southard, 2009; Schieber et al., 2016; Plint et al., 2012; Yawar and Schieber, 2017). Furthermore, "monotonous" successions of mud are not homogenous but are rather complex as shown by their wealth of physical sedimentary structures. This was achieved by the integrated efforts of experimental flume studies, scrupulous analysis of muddy outcrops/core and geochemical analysis (e.g., Pasley et al., 1993; Schieber et al., 2007; Bhattacharya and MacEachern, 2009; Li et al., 2015; Hart, 2016; Schieber et al., 2016; Li and Schieber, 2018).

Despite these advances, there have only been a few studies that have attempted to characterize the variability found in vertical successions that associate facies with depositional environments (e.g., Hart, 2016; Schieber et al., 2016; Birgenheier et al., 2017; Li and Schieber, 2018). This lack of studies is partially due to the difficulty of outcrop analysis, as mud sections are susceptible to weathering, which makes it difficult to conduct a detailed facies analysis (Macquaker and Gawthorpe, 1993; Schieber, 1999; Lazar et al., 2015, Li and Schieber, 2018). However, the major factor is due to the inherent complexity of mud-dominated deposits with regards to their high variability of sedimentary structures, bioturbation intensity/style and lithology. In order to complete a quantitative study on mudstones, it is mandatory to examine them in high-resolution (i.e. mm- to cm- scale), to not neglect any lamination/bed they are vital to understanding the relative proportions of depositional processes throughout a deposit. This

method can be time consuming and tedious. The importance of this detailed examination and analysis are twofold. First, the petroleum industry is in need of models that can be used to predict lateral and vertical variations, thickness, mineralogy, porosity, fabric, and organic content within mudstones based on sedimentological parameters (Hart et al., 2013; Hart, 2016). It is important to understand these properties because they are directly related to source-rock reservoirs, and can be used to predict hydrocarbon type, porosity, permeability and fracturing properties (Hart et al., 2013). Secondly, it is of academic importance to address debatable concepts between sedimentologists, organic geochemists, and paleontologists on the processes governing the deposition of mud; such as our past understanding of the deposition of organic rich muds, presence of bedload transport of flocculated muds in mud-dominated shelves, the provenance of mud clasts, and controversy regarding Cretaceous oceanic anoxic events (Jenkyns, 1980; Schieber et al., 2007; Schieber and Southard, 2009; Plint, 2014; Schieber, 2015; Hart, 2016). It is shown in this study, that a majority of the fine-grained sediment were not deposited by suspension settling as previously thought, but were deposited by energetic bedload processes composed of flocculated muds. Such energetic processes mix the water column, which refutes the idea of long-term oceanic anoxic events during the Cretaceous; notably at the sediment-water interface. Furthermore, flocculated clays are observed in this study, suggesting that bedload transport played a role in contributing to the formation of mud clasts (Schieber, 2015).

1.1 Objective

This study focuses on sedimentological data collected from a slabbed core through the upper Mancos Shale and its associated geochemical data provided by Weatherford Laboratories. This project has three main objectives. (1) To document the facies variability within the upper Mancos Shale (i.e., candidate sequences, system tracts, parasequences, intra-parasequence) and

understand the dominant processes that govern the deposition of the upper Mancos Shale, (2) to propose a depositional model, which can help conceptualize and synthesize various shelf depositional environments and processes depending on the distribution of facies in the upper Mancos Shale, and (3) to discuss the industry implications of the findings in this study.

2. Geological background and study area

During the late Jurassic, the Western Cordilleran orogenic belt took form as the Farallon plate began to subduct beneath the North American Plate (Livaccaria, 1991; Kauffman and Caldwell, 1993; DeCelles, 2004). Magmatic arcs developed in conjunction with subduction-induced conductive heating, consequently reducing lithospheric integrity and propelling crustal thickening and the formation of the Sevier fold-thrust belt (Livaccaria, 1991; DeCelles, 2004). Flexural loading from the Sevier orogeny eventually gave rise to an immense foreland basin east of the orogenic belt, known as the Western Interior Basin (WIB) (Kauffman and Caldwell, 1993; DeCelles, 2004; Liu et al., 2011). At the same time, the Mogollon highlands were uplifted and tilted, structurally controlling the WIB from the south-west (Bilodeau, 1986; Kirkland, 1991)

At the end of the early Cretaceous (Aptian-Albian), the WIB was flooded in response to the culmination of both load-induced subsidence and large-scale tectono-eustatic sea level fluctuations; creating the Cretaceous Western Interior Seaway (CWIS) (Kauffman, 1977; Kauffman and Caldwell, 1993; Sageman and Arthur, 1994). The CWIS reached its peak eustatic highstand in the late Cretaceous, connecting the Gulf of Mexico and the Northern Boreal sea (Fig. 1). At its deepest, the epeiric seaway never exceeded a few hundred meters, but was ~1500 km wide (Haq et al., 1987; Weimer, 1984; Kauffman, 1984, 1985; Sageman and Arthur, 1994). The circulation of the seaway in the Late Cretaceous was mainly dominated by the activity of storms and river processes, producing southerly currents, transporting sediment along the

western margin of the CWIS (Barron, 1989; Ericksen and Slingerland, 1990; Slingerland and Keen, 1999, Li and Schieber, 2018). The Sevier orogenic belt supplied an immense amount of Paleozoic lithic sediment to the east, while arkosic sediment was being supplied from the Mogollon highlands from the south-west (Molenaar 1983; Dickinson et al., 1988; Kirkland, 1991). During the Coniacian, the Upper Mancos was deposited (Fig. 1). Subsequently, the Laramide orogeny created a mosaic of smaller structural basins within the WIB, preserving much of the Cretaceous sediment that was deposited (Brown, 1988; Dickinson et al., 1988; DeCelles, 2004). Today, a majority of the Cretaceous mud-dominated sediment deposited in the CWIS can be found in the Mancos Shale Formation, within the Laramide structural San Juan Basin, New Mexico.

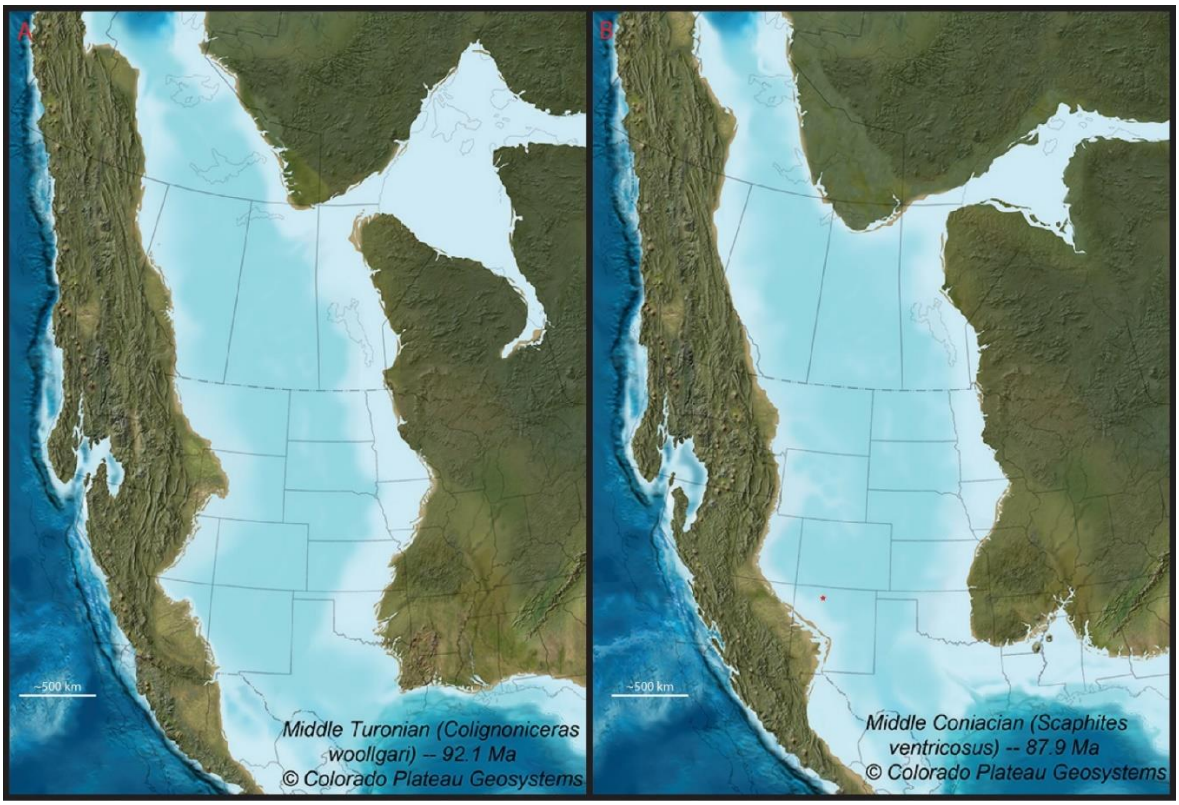

Fig. 1. A). Middle Turonian paleogeographic map showing the maximum extent of the Western Interior Seaway (Blakey, 2014). B). Middle Coniacian paleogeographic map showing the Western Interior Seaway during the deposition of the Upper Mancos. The red star indicates location of core analysed in this study.

The Mancos Shale in the San Juan basin is subdivided into the Lower and Upper Mancos Shale, which are separated by the regional basal Niobrara unconformity (Fig. 2) (Dane 1960; Pentilla, 1964; McPeek, 1965; Lamb, 1968; Molenaar, 1973, 1977; Molenaar and Baird, 1992; Ridgely et al, 2013). The Lower Mancos comprises from base to top the Graneros Shale, Greenhorn Limestone, lower Carlile Shale, Juana Lopez Member, and the upper Carlile Shale (Fig. 2). The Gallup Sandstone can be found above, intertongueing with the lower Carlile Shale, Juana Lopez and upper Carlile shale members in the northeastern parts of the San Juan Basin (Molenaar, 1973, 1977; Broadhead, 2015). Unconformably overlying the Lower Mancos Shale (except where the Gallup Sandstone can be found), is the Upper Mancos which has been informally divided into Mancos C, B, and A from bottom to top. The subdivisions are based on prominent, laterally extensive markers on gamma-ray and resistivity logs in response to changes in sand, silt, and carbonate content (Broadhead, 2015). The Upper Mancos is approximately 900-1550ft (274-457m) thick, where generally the thinnest sections are toward the southwest and thickest toward the northeast. The only exception to this trend, is the Mancos C, as it is thinnest in the southeast and thickest in the northwest (Broadhead, 2015). Adjacent to the southwestern flank of the basin is the Tocito sandstone, found within the lower parts of the Mancos C. Above the Tocito Sandstone and within the east of the basin, lies the interbedded sandstone, siltstone and mudstone succession known as the El Vado Sandstone Member (Fasset and Jentegen, 1978; Ridgley et al., 2013).

The core examined in this study was obtained from the Davis Federal 3 No. 15 well in Rio Arriba County, New Mexico (Fig. 3). Paleogeographic reconstruction and regional correlations indicate that the cored interval was approximately 220km offshore at the most distal,

and approximately 110km offshore at the most proximal (Fig. 1 and 3). Given that sediment was deposited in water depths of ~100m (Sageman and Arthur, 1994; Schieber, 2015), the slope of the shelf is estimated to have been around 0.026° (absolute value: $4.5x10^{-4}$) and 0.04° (absolute value: $7x10^{-4}$) for the most distal and proximal respectively.

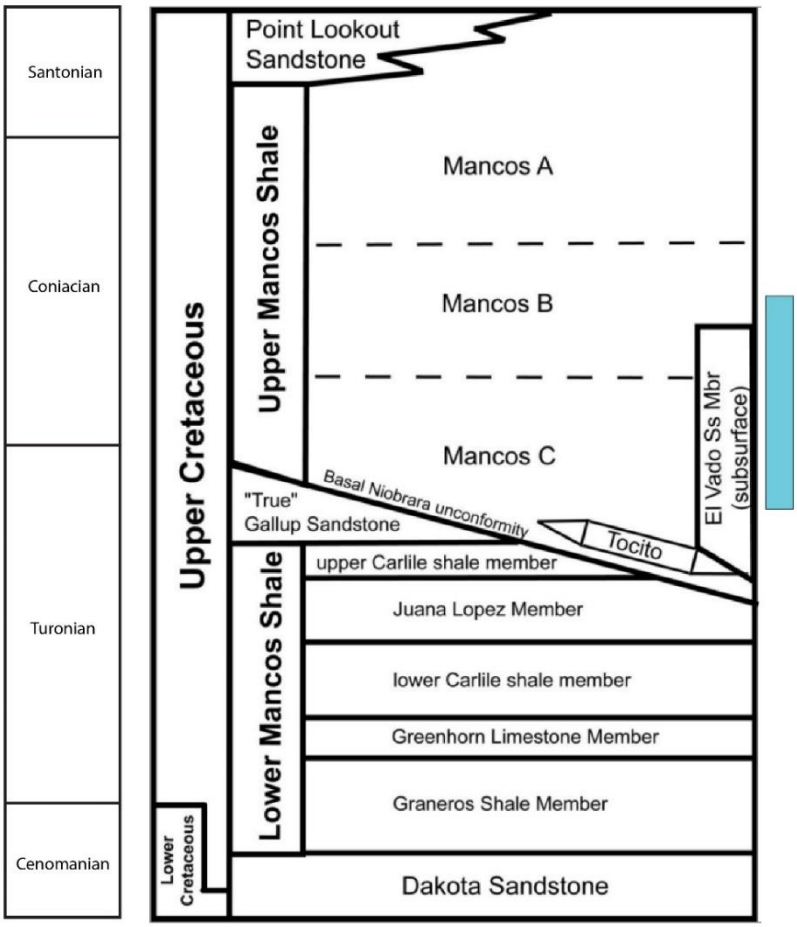

Fig. 2. Stratigraphic column of the Mancos Shale in the San Juan Basin (taken from Broadhead, 2015) with ages interpreted using the time stratigraphic cross-section from Ridgley et al. (2013).

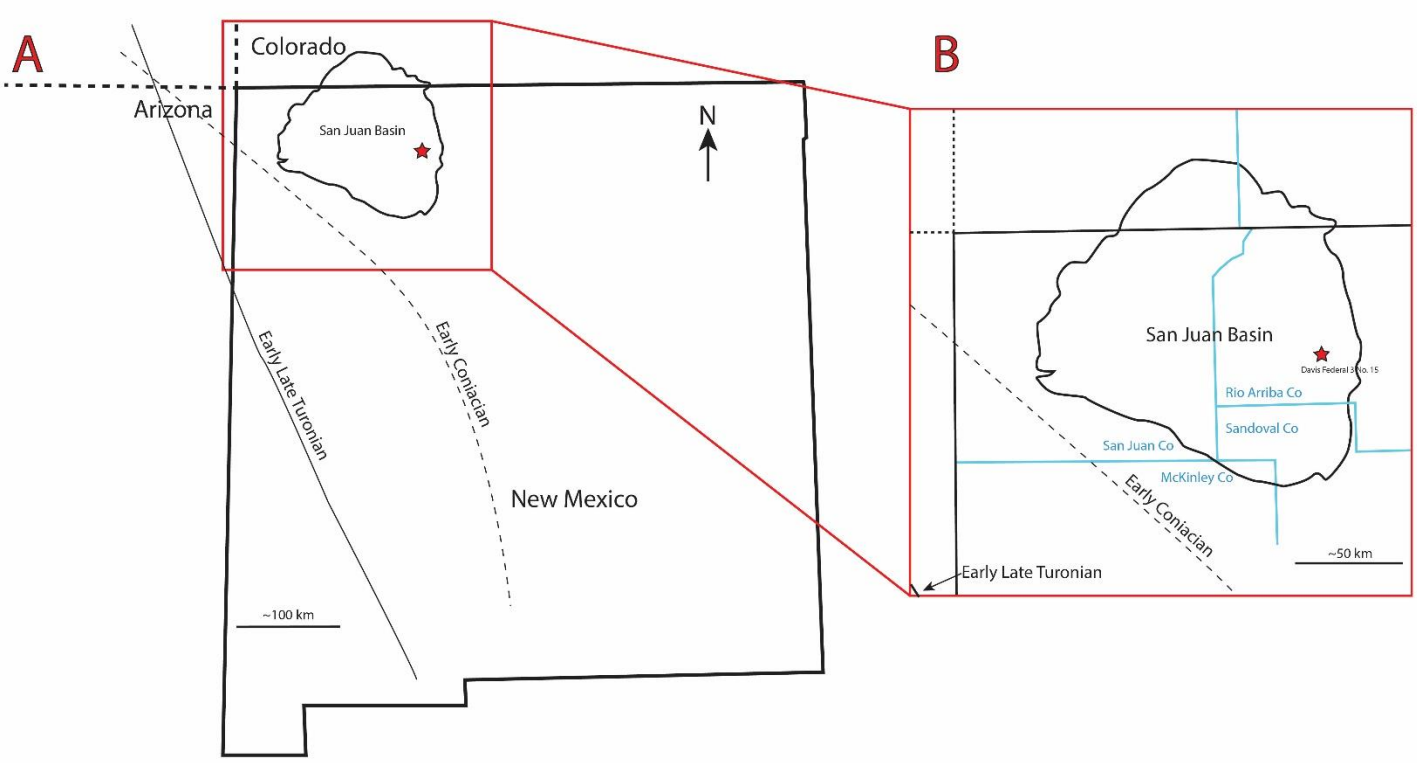

Fig. 3. A). Plan view map of New Mexico, including San Juan basin and location of the core shown as the red star. The short dashed line is the seaward extent of subaerial-plain deposits during the early Coniacian. The solid line is the landward extent of shoreline deposits during the early late Turonian. B). Close up plan view map of the San Juan basin. The blue lines highlight the county boundaries. The location of the core is shown by the red star (modified after Molenaar, 1983; Broadhead, 2015).

3. Methodology

3.1 Age of Core and Stratigraphic Context

A continuous 340ft (~103m) core was analysed, from depths of 7416-7076ft (~2260-2157m) (Fig. 4). In order to determine the age of the core and which formations it includes, the well log and a time stratigraphic map from Ridgely et al. (2013) was used (Fig. 5 and 6). The formations picked from the well log was based on significant changes in gamma and conductivity that marks the contacts between formations (Fig. 4). A depth shift between the core and well log was observed. This was solved by correlating the resistivity kick at 7160' in the well log with the contact found at 7165' in the core photographs. Therefore, there is an approximate shift of 5 feet, where the log appears shallower than the core. After tying the core to the well log, it was observed that the core runs from middle Mancos C to middle Mancos B (Fig. 2 and 5). The age of this interval was determined by referring to a time stratigraphic cross section modified by Ridgley et al. (2013), revealing that the core was deposited from late Turonian to Middle Coniacian (Fig. 2).

3.2 Thin-bedded Facies Analysis

The analysis of the core was divided into two parts. The first part was done in the core lab, and the second was done remotely by analysing photographs. Data collection in the core lab involved various tools consisting of a hand lens, measuring tape, grain size card, 10% HCl acid, binocular microscope, and a camera. The objective was to document properties that could not be resolved remotely, such as grain size, clay content, and lithology. Sedimentary structures, bioturbation intensity, fossils, trace fossils, and mineralogy were crudely examined as they were analysed in greater detail through photographs during the second part. The second part of the

analysis was completed at three different resolutions; macro- meso-, and micro-scale. Photographs of the entire core were taken at a meter-scale and stacked vertically for macro-scale analysis. Macro-scale analysis was used to identify candidate surfaces, parasequences, system tracts and sequences; as well as broad changes in lithology, sedimentary structures, bioturbation intensity, fossils, and trace fossils throughout the core (Fig. 4). Additional photographs were taken at the centimeter-millimeter scale for meso-scale analysis. Meso-scale analysis of the core was conducted on ten individual parasequences to resolve intra-parasequence variability regarding lithology, sedimentary structures, bioturbation intensity, fossils, and trace fossils. The ten parasequences were chosen partially based on the availability of ten photomicrographs from a Weatherford Laboratories' report, each found in their own respective parasequence. However, the ten parasequences were mainly chosen because the parasequences of the ten photomicrographs and SEM images were well distributed throughout the core, to allow analysis on compositional and depositional process variability. Lastly, photomicrographs and SEM images from the Weatherford Laboratories' report were used for micro-scale analysis. Micro-scale analysis was done to resolve the mineralogy and microfossils at a specific section within a parasequence. Abundances of calcareous, siliciclastics and diagenetic components were observed in each photomicrograph. When interpreting beds and laminations, the classification by Campbell (1967) was used (Fig. 7). In this study, the range of thicknesses observed include very thin lamina (i.e., <3mm) to medium beds (i.e., <30cm). The most ubiquitous thicknesses were very thin lamina and thin lamina.

3.2.1 Identification of Core Properties

Grain Size and Clay Content

The Wentworth classification was used to determine grain sizes visible to the naked eye. However, for grain sizes that cannot be resolved by a hand lens (i.e. silt and clay), the rock was chewed and observed for colour variations to determine percentage of clay content (e.g., Li and Bhattacharya, 2015). Mudstone samples with a lower clay content will exhibit a more gritty texture, while samples with a higher clay content will have a smooth "toothpaste" texture (Lundegard and Samuels, 1980). Furthermore, clays are usually darker and contain darker grains, whereas silts are commonly lighter and are more greyish in colour.

Lithology

Lithology was determined with a hand lens. However, at intervals where carbonate and lithic grains were difficult to differentiate, a binocular microscope was used. Aside from basic lithological facies observations, this study did not focus on the geochemical properties of the core. However, the results from a detailed geochemical study from a Weatherford Laboratories' report were used in this study. Their data consisted of a continuous lithology log of the core, and the examination of ten samples by X-ray diffraction (XRD), scanning electron microscopy (SEM), and detailed thin section modal analysis (DTSA).

Bioturbation Intensity/Style

The Taylor and Goldring (1993) Bioturbation Index (BI) was used to determine bioturbation intensity. Depending on the percent of bioturbation, a grade from zero to six was assigned, wherein a zero indicates no bioturbation and a six indicates complete bioturbation.

Each bed associated with a BI can be plotted and connected, creating a curve known as the BI log, which reveals the vertical variability of bioturbation intensity throughout the core.

Photomicrograph Analysis

Visual abundances of calcareous, siliciclastic, and diagenetic components of photomicrographs were based on the identification of grains and mineralogy provided by Weatherford Laboratories. Interpretations that were concluded were made from the abundances of these three components observed in this study. For each photomicrograph, the three components were assessed on a relative scale of high, medium or low. Furthermore a ratio between framework grains and matrix was given.

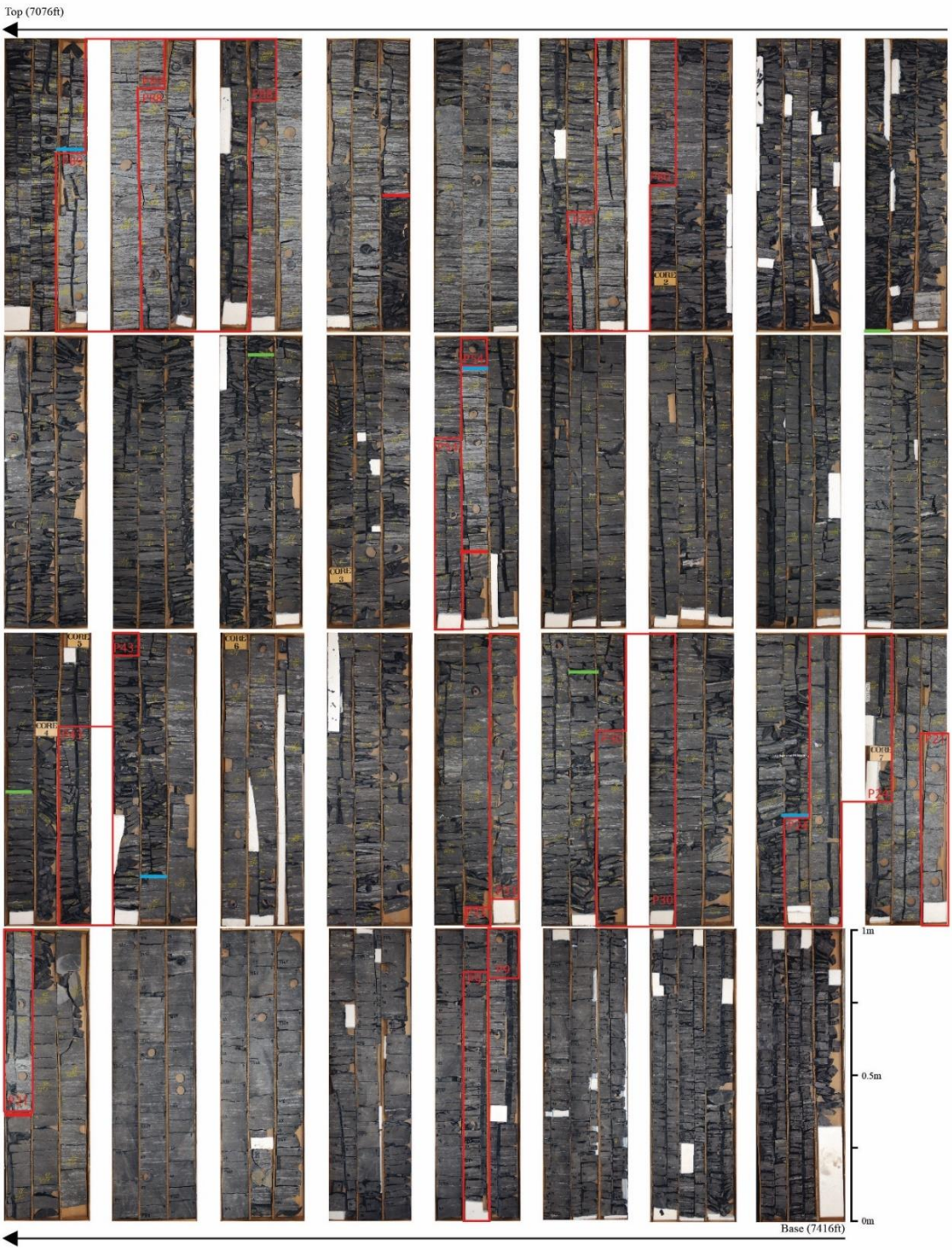

Fig. 4. Photographs of the core from the Davis Federal 3 No. 15 well in Rio Arriba County, New Mexico. The base begins at 7416ft and the top ends at 7076ft. Parasequences examined are highlighted in the red boxes. Surfaces are marked by the red, blue and green lines, corresponding with the sequence boundary, transgressive surface and maximum flooding surface respectively.

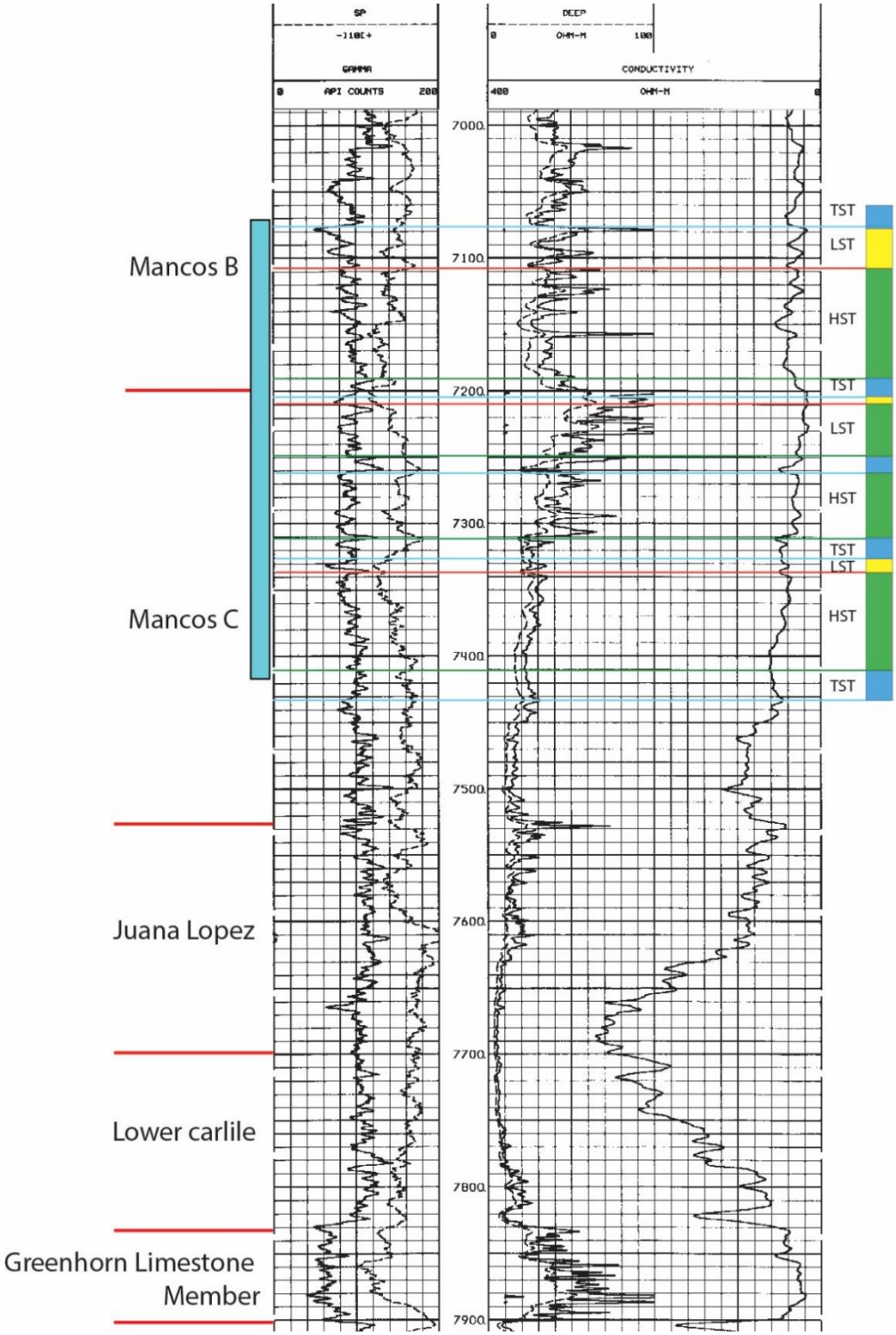

Fig. 5. Well Log for Davis Fed Com. 3-15. Formations are separated by the thick red lines on the left, suggested by Broadhead (2015). Light blue rectangle shows the length of the core examined in this study. The thin red, blue, and green lines on the well log corresponds to the sequence boundary, transgressive surface and maximum flooding surface respectively. System tract interpretation is on the right.

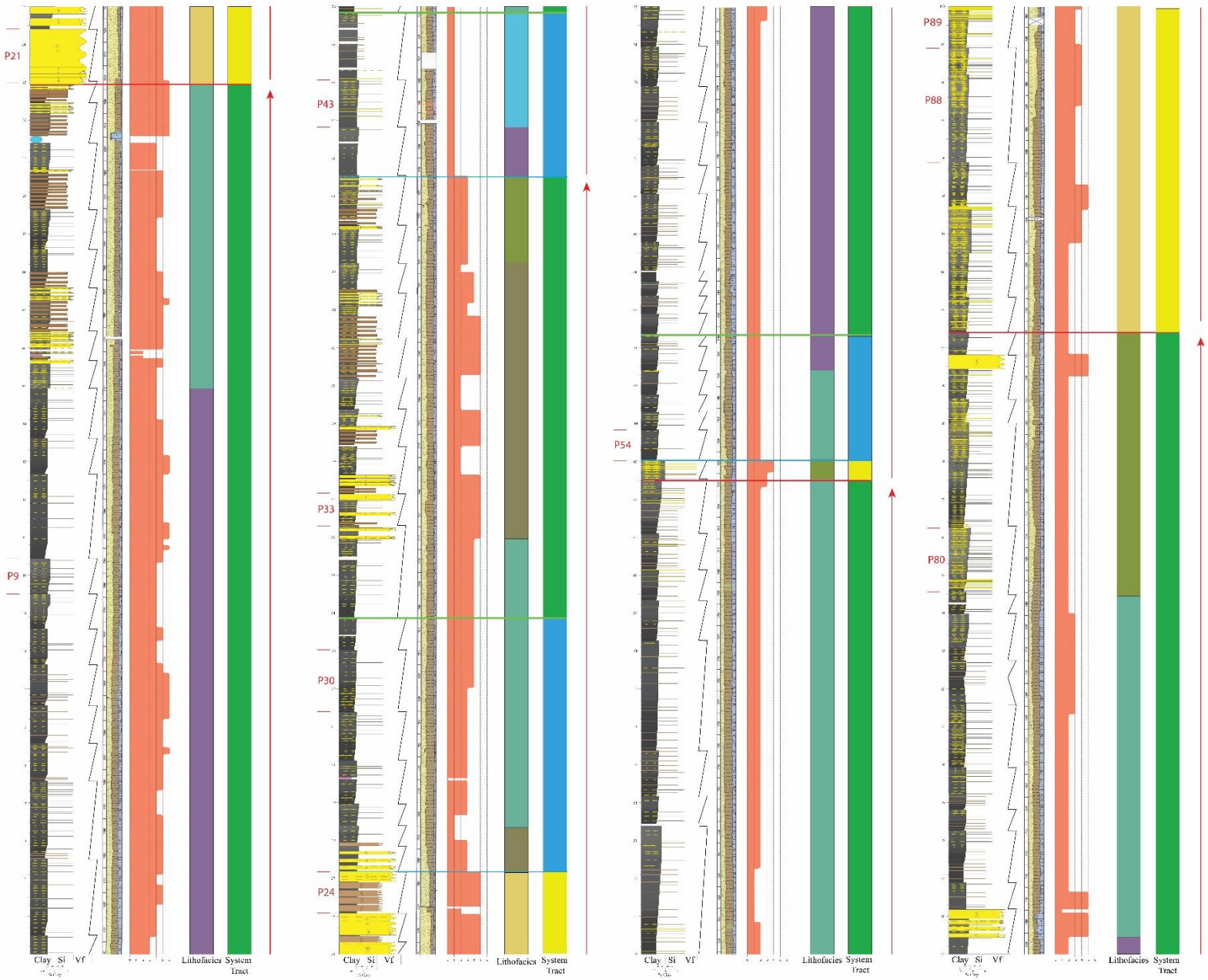

Fig. 6. Macro-scale analysis of the core, including a stratigraphic log, identified parasequences, marked by the black zig-zag lines, lithology graphic log, BI log, lithofacies column, and a system tract column. Parasequences are numbered, 1 at the base to 92. Only parasequences selected for more detailed meso-scale analysis are actually labelled. Parasequences examined are marked by red lines with a labeled "P#" in between. The thin red, blue, and green lines transecting the columns correspond to the sequence boundary, transgressive surface and maximum flooding surface respectively. Sequences are shown by the red arrows on the right of each column.

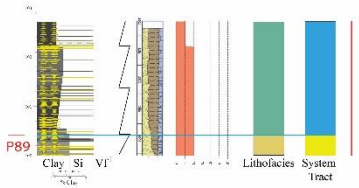

Fig. 7. Bed and lamina classification, defined by Campbell (1967). (taken from Passey et al., 2006).

4. Facies and Facies Association Identification and Interpretation

Eleven main facies were observed in meso-scale analysis; they include: structureless mudstone, structureless sandstone, bioturbated mudstone/sandstone, generic ripple laminations, wave ripple laminations, combined-flow ripple laminations, current ripple laminations, parallel laminations, normal grading, muddy carbonate, flaser and wavy bedding, and bentonite ash layer. The facies key is provided in figure 8.

Fig. 8. Facies key with symbols and colours used for sedimentary structures, trace fossils, lithofacies, facies associations, and surfaces. The 11 facies in this study are also listed.

4.1 Facies Identification and Interpretation

Facies 1: Structureless

Facies 1a: Structureless Mudstone with Bioturbation

Structureless mudstones with bioturbation contain trace fossils, but have no internal sedimentary structures (Fig. 9A). Thicknesses of this facies ranges from very thin laminations to medium beds that were tens of centimeters (Fig. 9B). Mudstone beds were found in various sections of the core, commonly with other muddy intervals. Mudstone laminations were commonly found in between other facies (i.e., wave ripple, combined-flow ripple, current ripple) (Fig. 9A). Structureless mud with light to medium bioturbation suggests deposition from suspension settling. Suspension settling has a relatively low sedimentation rate, which allows organisms to colonize the sediment (MacEachern and Stelck, 1999).

Facies 1b: Structureless Mudstone without Bioturbation

Structureless mudstones without bioturbation showed no trace fossils nor internal sedimentary structures (Fig. 9B, D). Thicknesses of this facies ranged from very thin laminations (Fig. 9A) to medium beds (Fig. 9B). The absence of internal structures suggests rapid deposition. This facies was most likely deposited by fluid mud flow (Ichaso and Dalrymple, 2009). Fluid muds are any mobile bottom hugging fine-grained sediment with a solid concentration of >10g/L (Kirby and Parker, 1983; Ichaso and Dalrymple, 2009). Fluid mud flows are geologically instantaneous, capable of depositing within hours. At this depositional rate, organisms do not have enough time to colonize the sediment. Furthermore, grading or laminations are rare because of the flow's high viscosity inhibiting grain segregation to form such features (Ichaso and Dalrymple, 2009).

Facies 1c: Structureless Sandstone

Structureless sandstones showed no internal sedimentary structures. The thicknesses of this facies were variable, ranging from very thin laminations to medium beds. Sandstone beds were usually found with other sandy intervals (Fig. 9C) and sandstone laminations were commonly found with adjacent sandy areas with differentially compacted sediment (Fig. 9E). The absence of internal structures suggests rapid deposition. This facies was most likely deposited by ignitive turbidites, as this process deposits sand rapidly from a liquefied debris flow (Lowe, 1982; Kneller and Branney, 1995; Talling et al., 2012).

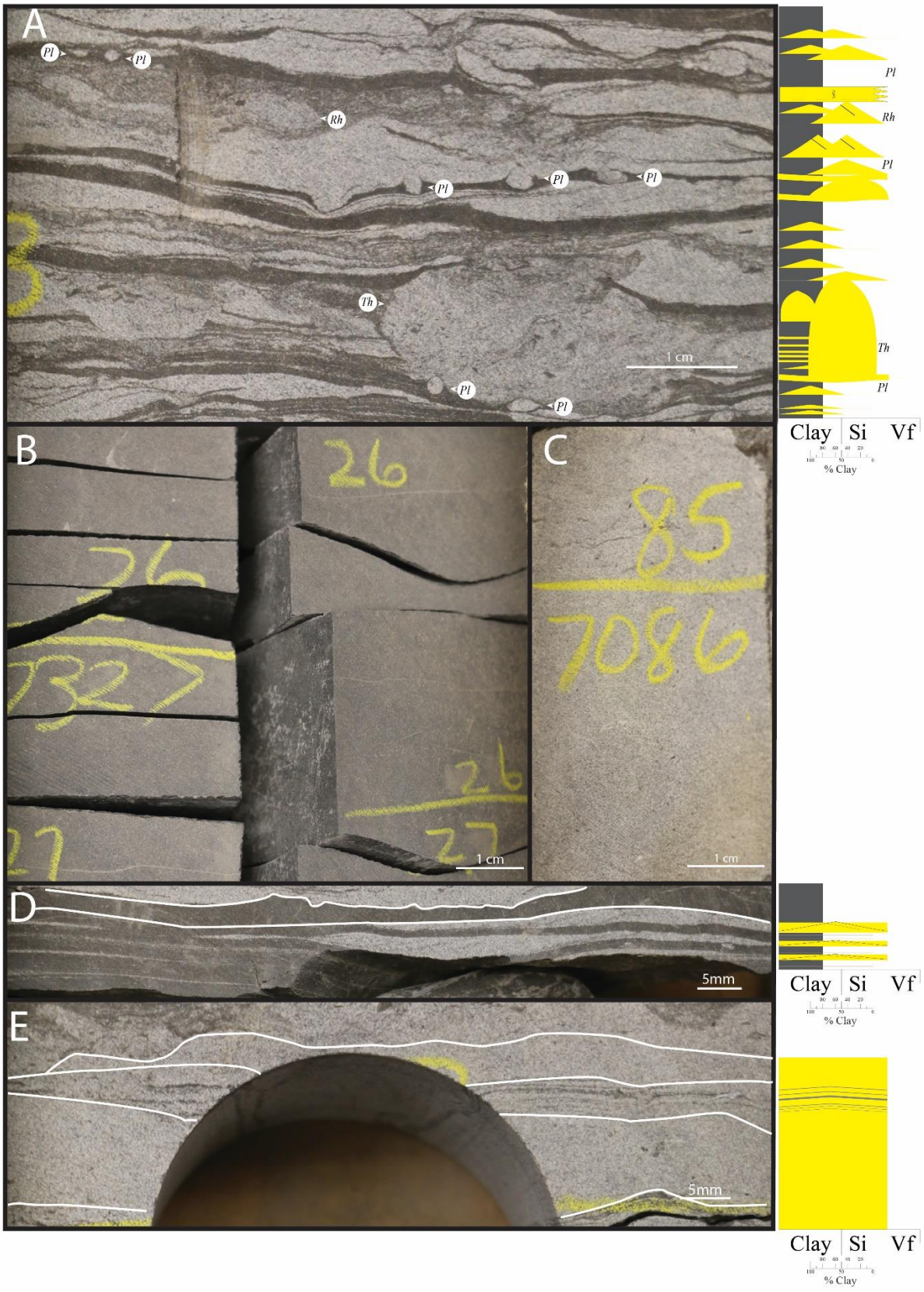

Fig. 9. Photographs highlighting structureless facies. A) Heterolithic with alternating sand and mud laminations. Structureless mud with *Planolites* burrows are found in between sand layers. Found at 7103.5ft B). Structureless mudstone bed at 7327ft. C). Structureless sandstone bed from 7086ft. D). Structureless mudstone lamination highlighted in white outline at 7123.25ft. E). Structureless sandstone beds highlighted in white outline at 7103.95ft.

Facies 2: Bioturbated Mudstone and Sandstone

Highly bioturbated mudstones and sandstones (BI: 5-6) show very little to no decipherable sedimentary structures or trace fossils (Fig. 10). Thicknesses of this facies were variable throughout, ranging a few millimeters to tens of centimeters. In deposits with a BI: 5, trace fossils include *Chondrities, Cosmorhaphe, Cylindricus, Planolites, Phycosiphon, Scolicia, Teichichnus, Thalassinoides, Rhizocorallium,* and *Zoophycos* (Fig. 10A). Deposits with a BI: 6 are completely bioturbated and any pre-existing sedimentary structures or trace fossils have been entirely disrupted (Fig. 10B, C).

Interpretation

High levels of bioturbation disrupt any pre-existing laminations, creating a convoluted deposit of both mud and sand. High bioturbation is indicative of oxygenated waters and slow sedimentation rates, allowing organisms to thrive (Howard, 1975; MacEachern et al., 2005). Analysis of rarely preserved trace fossils in deposits with a BI: 5 represent mostly a distal *Cruziana* to proximal *Zoophycos* ichnofacies. Identification of ichnofacies reveals that this facies is deposited in a marine setting, far below fair-weather wave base. Deposits with a BI: 6 were sometimes observed to have “fuzzy” cryptic bioturbation (e.g., Pemberton et al., 2008) (Fig 10B, C).

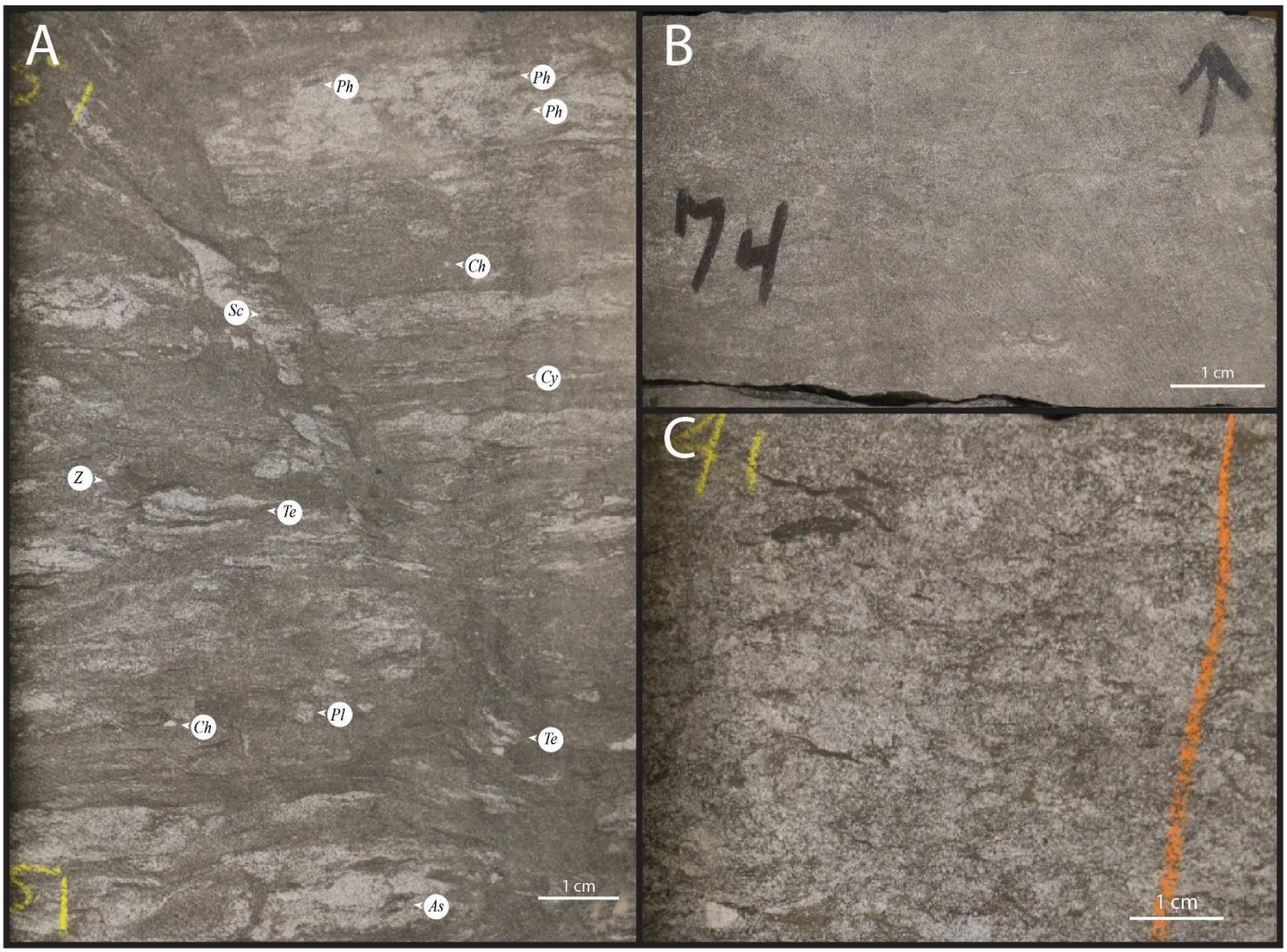

Fig. 10. Photographs highlighting bioturbated facies. A). Bioturbated sandy mudstone (BI:5) showing *Chondrities (Ch)*,*Cylindricus (Cy)*, *Planolites (Pl)*, *Phycosiphon (Ph)*, *Scolicia (Sc)*, *Teichichnus (Te*), and *Zoophycos (Z)* trace fossils. Taken from 7351.50ft . B). A pervasively bioturbated sandy mudstone (BI:6). Taken from 71374.50ft. C). A pervasively bioturbated muddy sandstone (BI:6). Taken from 7341.30ft.

Facies 3: Generic Ripple Laminations

This facies is characterized by discontinuous laminae with an erosive base, lacking any observable foresets to distinguish ripple type (Fig. 11). The thickness of this facies ranges from very thin lamina of 0.1mm (Fig. 11A, B) to very thin beds of 1cm (Fig. 11C). Bioturbation intensity can be low, as seen in figure 11A, or moderate as seen in figure 11C.

Interpretation

The lack of foresets may be from compressional forces after burial of sediment (Yawar and Schieber, 2017). Without foresets, it is difficult to precisely identify the type of ripple (i.e., current or wave), and hence cannot be attributed to a depositional process. Therefore this facies is interpreted to have been deposited by a bedload transport process, and provide evidence of energetic events along the seabed as result of currents and/or waves.

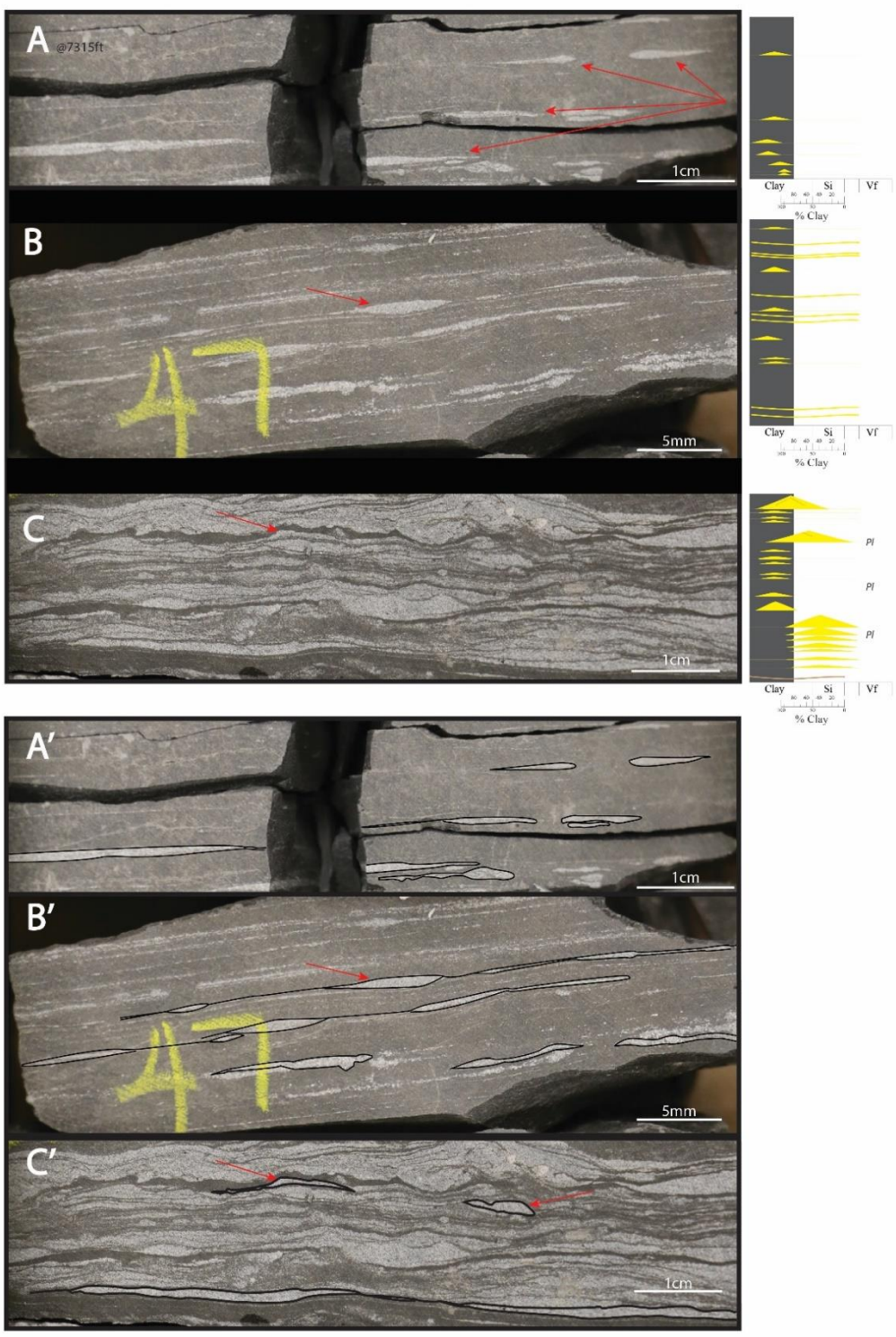

Fig. 11. Examples of generic ripples. A). Thin starved ripples with asymmetrical crests and unobservable foresets, at 7315ft. Red arrows point to the generic ripples B). Starved ripple with an irregular crest and few observable foresets at 7147.95ft. C) Starved ripple with no observable foresets or laminations at 7136.20ft. Deformation of ripple crest and internal foresets renders it undistinguishable. Few *Planolites* burrows can be seen. A'-C'). Line drawings highlighting this faces in A-C respectively.

Facies 4: Wave Ripple Laminations

Wave ripples were identified by their rounded symmetrical crests and laminations (Campbell 1966; Jopling and Walker, 1968) (Fig, 12). Thicknesses range from very thin wavy parallel laminations that are 0.1mm (Fig. 12F) to amalgamated wave ripples resembling thin bedded HCS deposits that are a few centimeters thick (Fig. 12C). Amalgamated wave ripples are similar to HCS deposits but at a smaller scale (i.e., <5cm thick) (Fig. 12C). Basal scours, soles marks and the overlapping of hummock and swaley laminae were observed (Fig. 12C, D, C', D') (Walker et al., 1983; Prave and Duke, 1990; Cheel and Leckie, 1993; Dumas and Arnott, 2006). Bioturbation is generally low, to absent.

Interpretation

Wave ripples are caused by oscillatory flows that are produced during storms (Leckie, 1988). Depending on the storm magnitude and water depth, various thicknesses of wave ripples or wavy laminae can be formed (Harms, 1979; Dott, 1982). It is expected that inner-shelf environments will develop wave rippled laminations/beds with greater amplitude and wavelengths than middle- to outer-shelf environments, because oscillatory energy decreases as water becomes deeper. Furthermore, the amplitude and wavelength of wave rippled laminations/beds will also decrease when storm energy beings to wane. The low wavelength of these facies suggests a medial to distal shelf environment in depths probably less than 100m.

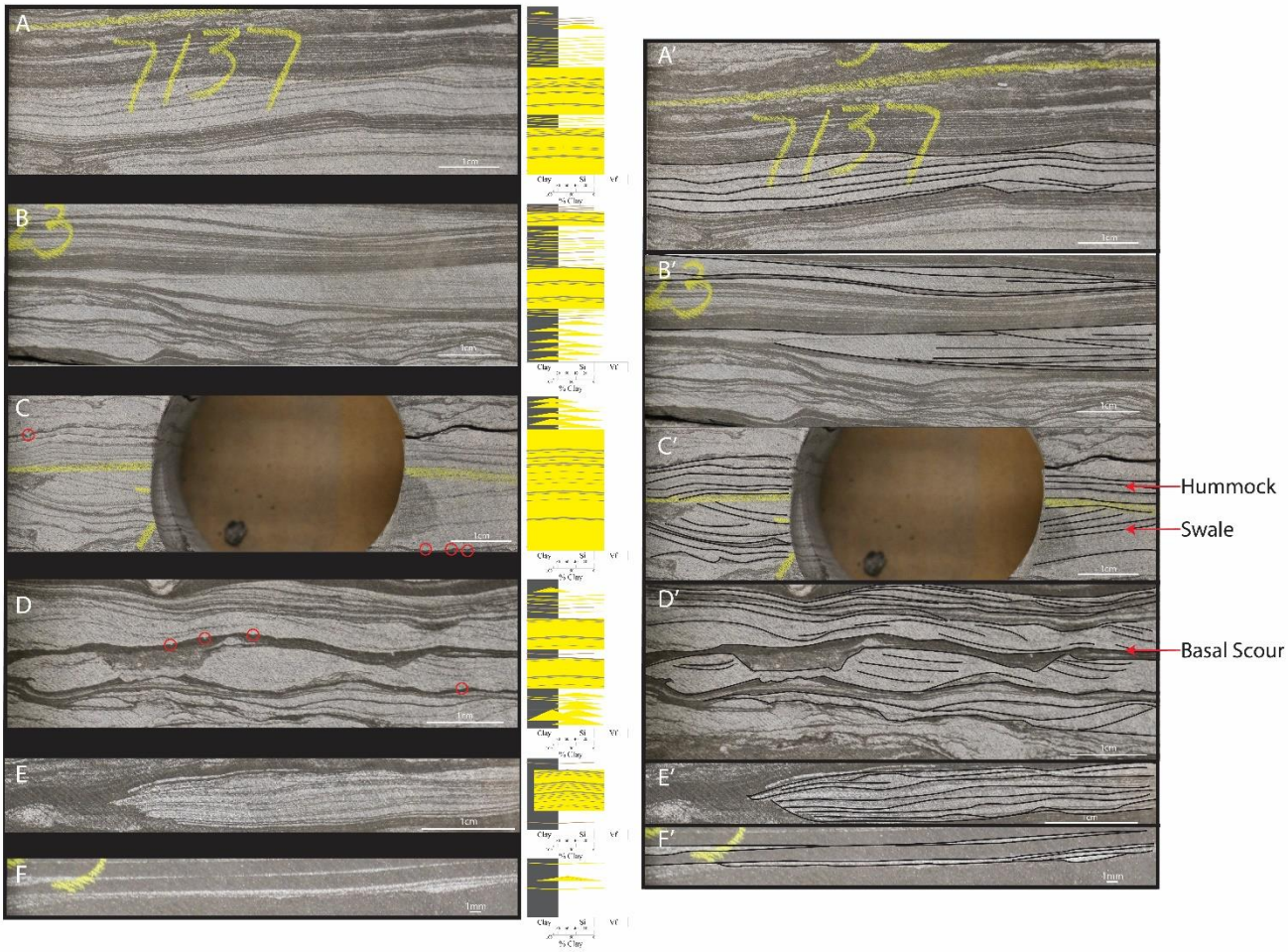

Fig. 12. Photographs highlighting wave rippled facies. Sole marks are shown by the red circles. A). Wave rippled lamination at 7137ft. B). Amalgamated wave ripple lamination at 7123.80ft. C). Amalgamated wave ripple bed at 7135ft At. D). Starved wave ripple laminations and wave ripple laminations at 7094.10ft E). Starved wave ripple lamination at 7207.99ft. F). Thin wavy laminations. A'-F') Line drawings of A-F respectively. Labelled red arrows point to features observed.

Facies 5: Combined-Flow Ripples

Combined-flow rippled laminations/beds are represented by rounded, wavy and/or symmetrical ripple crests with downlapping foresets in one direction onto a basal scour (Dumas et al., 2005) (Fig. 13). The thickness of this facies ranges from very thin lamina of 0.5mm to very thin beds of 1cm. Figure 13A illustrates a few combined-flow rippled laminations, with foresets dipping to the left as highlighted by its respective line drawing. The rippled crests, and stoss and lee sides are rounded. Other features including wavy laminae and generic ripples can be seen. Figure 13C, D both contain combined-flow ripples with two different foreset downlapping directions. As shown in their respective line drawings, the foreset direction of a succession of beds are different. Figure 13E shows a symmetrical rounded ripple crest with foresets downlapping to the left. Bioturbation was often found within mudstone laminations in between the sandstone combined-flow rippled laminations.

Interpretation

Dumas et al. (2005) described the properties of a combined-flow ripple, such as steepness of lee faces, roundness, and shape of crest and stoss and lee sides. Combined-flow ripples generally exhibit a gentler lee side dip angle (<~24°) compared to unidirectional current ripples (>30°). Their study also coincides with the findings in Harms (1969), which showed that lee side dip angles of combined-flow ripples range from ~23-34°. The roundness of the combined-flow ripple crest was recognized to be diagnostic in identifying this type of ripple (Bucher 1919; Harms 1969; Dumas et al., 2005). Dumas et al. (2005) noted an increase in visual roundness of a rippled bedform when flow conditions evolved from a dominantly oscillatory flow to unidirectional-dominant combined flow. The shape of the crest and stoss and lee sides of combined-flow ripples varies depending on oscillatory and unidirectional flow velocities. Combined-flow ripples formed

under oscillatory-dominant conditions were observed to have straight to biconvex flanks, locally deep and narrow troughs, and rounded crests. With further increase in unidirectional flow velocity, the stoss and lee sides become distinctly biconvex, crests become well rounded and locally distinct from the brickpoint and local deep scours appear on lower end of the stoss side (Dumas et al., 2005). Dumas et al. (2005) summarized their findings in a figure, highlighting the three types of combined-flow ripples including the "normal profile, "boxy" profile, and bulging profile (Fig. 14). These properties described in Dumas et al. (2005) proved helpful in identifying combined-flow rippled laminations/beds in this study.

The downlapping foresets indicate unidirectional flow interpreted to be from geostrophic currents, storm-setup relaxation flows or tidal currents. However, oscillatory motion from simultaneous storms overprints the unidirectional current ripples, forming a symmetrical, rounded, and/or wavy crest (Arnott and Southard, 1990; Dumas et al., 2005; Baas et al., 2016; Li and Schieber, 2018). The proportion of wave or current influence is dependent on which process (unidirectional or oscillatory flow) had greater influence (Arnott and Southard, 1990; Dumas et al., 2005; Baas et al., 2015). In the inner-shelf environments, more combined effect or wave dominated processes are expected due to shallower water depths. However in the outer-shelf, oscillatory motion is much weaker and wave overprinting is expected to occur less (Li and Schieber, 2018). Combined-flow ripples therefore represent both unidirectional and oscillatory flow.

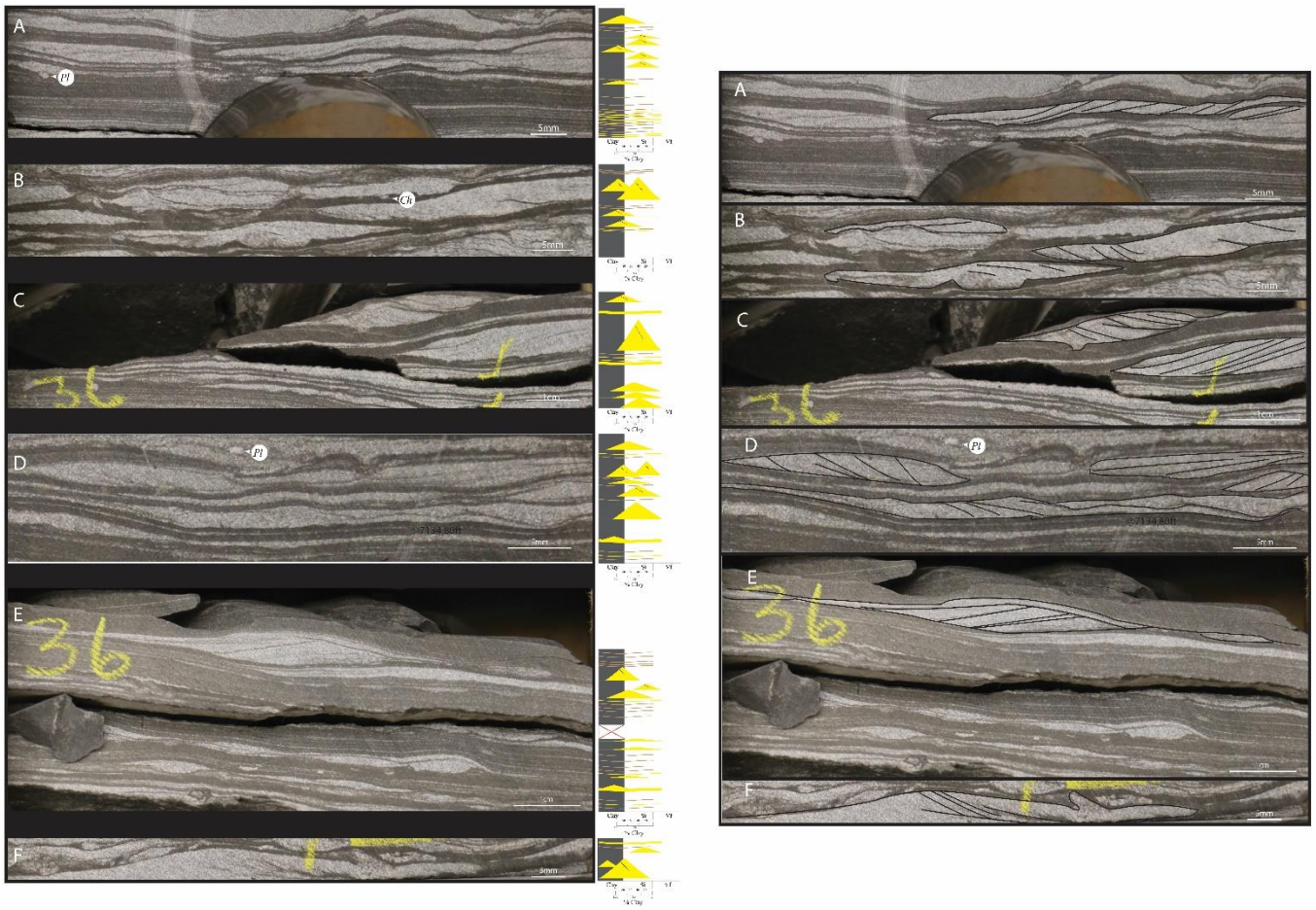

Fig. 13. Photographs highlighting combined-flow ripple facies A). Combined-flow ripple laminations with foresets dipping to the left at 7134.99ft. B). Starved combined-flow ripple laminations with foresets dipping to the left and right at 7094.05ft. C). Starved combined-flow ripple laminations with foresets dipping to the left and one dipping to the right at 7136.10ft. D). Starved combined-flow ripple laminations with foresets dipping to the left and one dipping to the right at 7134.80ft. E). Starved combined-flow rippled lamina with forests dipping to the left at 7136.80ft. F). Starved combined-flow ripple lamination with foresets dipping to the right at 7092.99ft

Fig. 14. Different combined-flow ripple profiles (taken from Dumas et al., 2005).

Facies 6: Current Ripple Laminations

Current ripples (Fig. 15) were identified by foresets downlapping onto a scour base and an asymmetrical ripple crest composed of a gently sloping stoss and steep lee side. The base and top of these ripples are in sharp contact with adjacent deposits. Thicknesses of this facies varies from very thin laminations (Fig. 15C) to thin laminations (Fig. 15A). Current ripple laminations that were very thin were similar to parallel laminations, but careful examination reveal subtle downlapping patterns that suggest it was once a ripple (Fig. 15B, C) (Yawar and Schieber, 2017). The more conventional thin current ripple laminations with a clear straight asymmetrical crests were also seen (Fig 15A) (Jopling and Walker, 1968; Reineck and Singh, 1980). Bioturbation was often found within adjacent mudstone layers (BI: 0-2).

Interpretation

Current ripples are produced by unidirectional flows, possibly from geostrophic, relaxation flows, and tidal currents; forming a basal scour surface, downlapping foresets and an asymmetrical ripple crest (Suter, 2006; Li and Schieber, 2018). Current ripples migrate downflow by erosion of sediment from the stoss side and avalanching of bedload onto the steep lee side of the current bedform (Dumas, et al., 2005; Baas et al., 2016). This migration leads to the formation of high angle cross laminations (Fig. 15A, A'). However, current ripple cross laminations are difficult to identify in mud-dominated rock successions because of the ability for ripples to compress. After compaction of sediment, they can easily be mistaken for parallel laminations (Yawar and Schieber, 2017). In this study, thin low-angle current ripples were dominantly observed (Fig. 15B, C). In order to distinguish between current ripples and parallel laminations, it is mandatory to examine for low-angle downlapping surfaces that indicate they were once current ripple foresets.

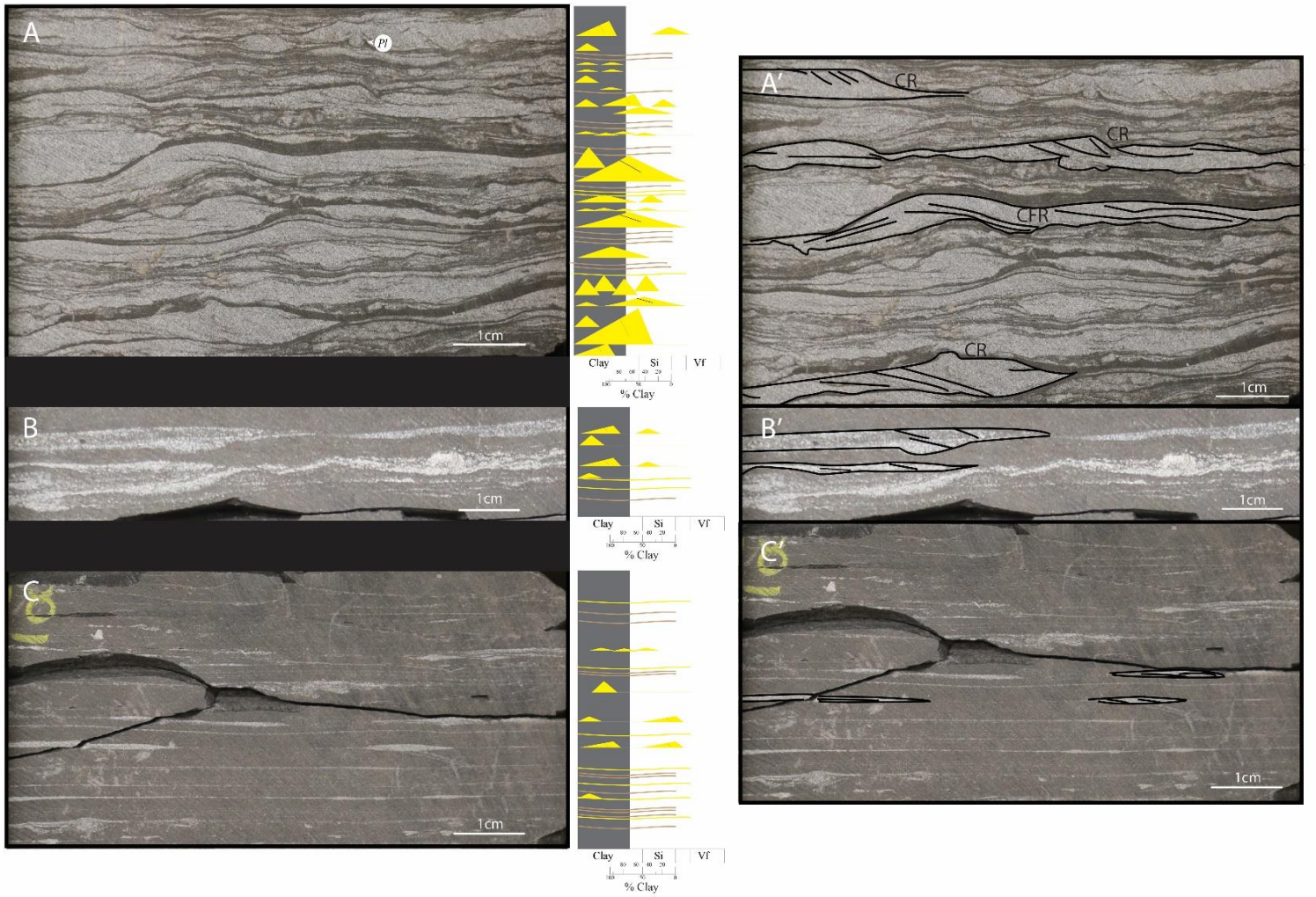

Fig. 15. Photographs highlighting the different types of current rippled (CR) laminations seen in this study. A). Deposit with combined-flow rippled (CFR) laminations, CR laminations, generic rippled laminations and wavy laminae at 7092.50ft. CR shown have the conventional straight asymmetric ripple crests, and gently sloping stoss and steep lee sides. The respective line drawing highlights both current rippled (CR) laminations and combined-flow rippled (CFR) laminations B). Current rippled laminations with observable downlapping foresets and straight asymmetrical crest. Found at 7263.50ft. C). Compacted current rippled laminations, portraying scouring, low-angle downlapping foresets and straight asymmetrical crests. Found at 7318.60ft. The respective line drawing highlights the foresets and crests seen.

Facies 7: Parallel Laminations

Parallel laminations are composed of sand or silt, and found in lamina sets (Fig 16). Common parallel laminations observed in this study include planar and wavy. Laminae in a parallel planar lamina set are relatively straight, showed no striatal terminations and did not intersect other laminae (Lazar et al., 2015) (Fig. 16A, B). Wavy parallel laminae also did not intersect other laminae, but are undulatory instead of straight (Fig. 16E). Parallel laminations are regularly found underlying normally graded beds (Fig 16B, C). Individual laminae are commonly 0.1mm. Lamina sets, however have variable thicknesses, ranging from 1mm to 1cm. Bioturbation is generally present within adjacent mudstone layers (BI:0-1).

Interpretation

Parallel laminations are commonly produced by small-scale fluctuations within flow, such as oscillation-currents and turbidity currents, where oscillation currents produce parallel wavy laminations and unidirectional currents produce parallel planar laminations (Bouma, 1962; Shanmugam, 1997; Lazar, 2015). Thin parallel laminations come in lamina sets, often alternating silt- and clay- rich mud laminae (Fig. 16B, E). The laminations were dominantly continuous, suggesting that sedimentation was continuous (Bohacs et al., 2005). Parallel laminations are often found underlying normally graded beds as they are commonly associated with waning flows such as turbidity currents or tempestites. When flow energy decreases, a normally graded lamination/bed will deposit as sediment fallout from suspension (Bouma, 1962; Walker et al., 1983; Myrow et al., 2002; Suter, 2006) (Fig. 16B, C, D, E). Lamina sets could also be tidal rhythmites if spring and neap bundles are observed (Mazumder and Arima, 2005).

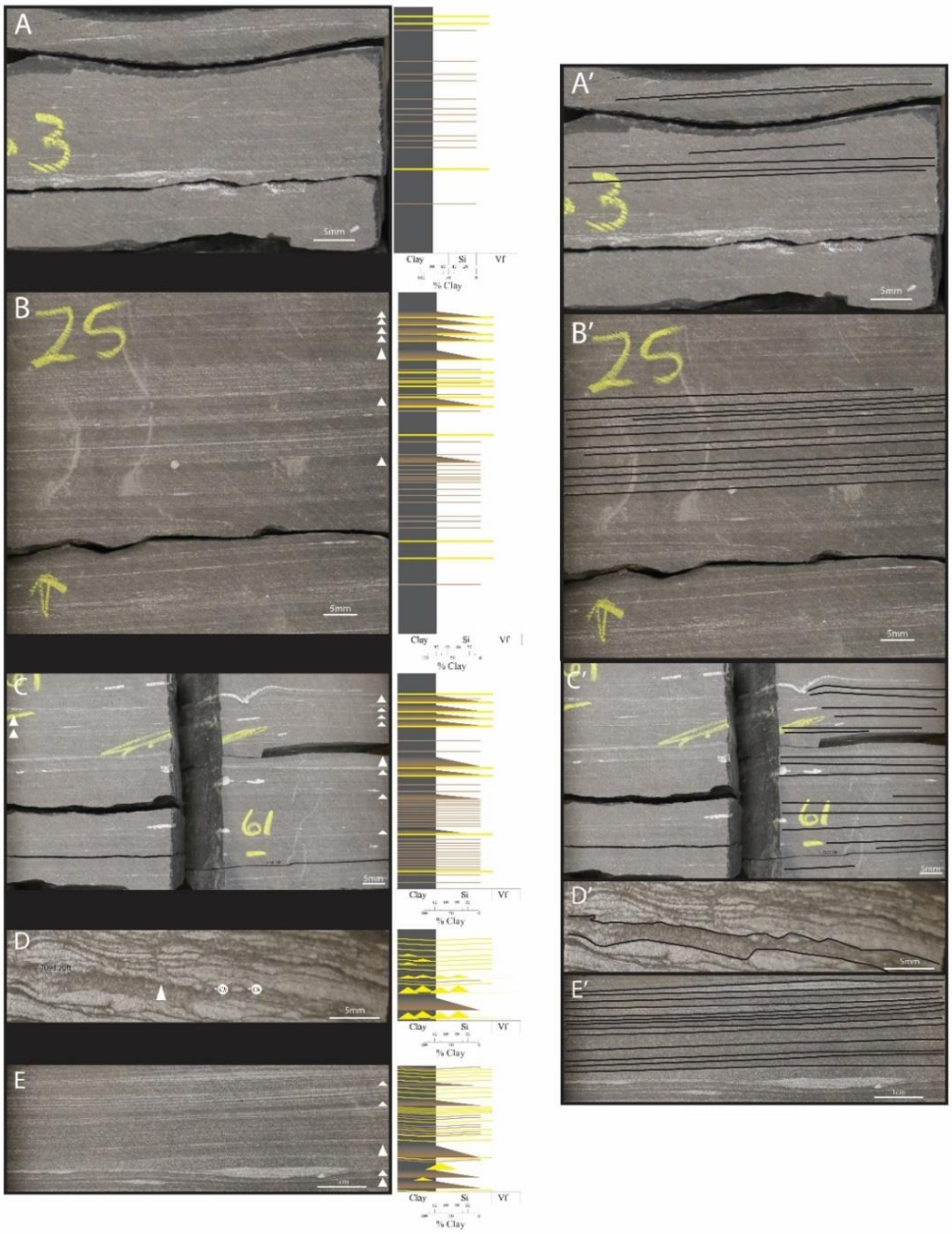

Fig. 16. Photographs highlighting parallel laminations and normal grading with line drawings. A). Silt and very fine lower sand parallel planar laminations at 7263.70ft. B). Very fine lower sand and silt planar laminations with normal grading at 7225.20ft. Normally graded laminations are marked by the white triangles. C) Very fine lower sand and silt parallel planar laminations with normally graded laminations at 7225.20ft. Normal grading is marked by white triangles. D) Very fine lower generic ripples with one normally graded laminae marked by the white triangle at 7094.20ft. E) Very fine lower sand and silt parallel wavy laminations with normally graded laminations marked by the white triangles at 7181.10ft.

Facies 8: Normal Grading

Normal grading was recognized by a gradual fining upward, typically from sand to silt to clay (Fig. 16B, C, D, E). Thicknesses are dominantly a few millimeters but have a range from very thin lamination of 0.5mm to very thin beds of 1cm. Bioturbation is uncommon, however if present, bioturbation is commonly found within the top clay layer.

Interpretation

Normal grading is formed from suspension settling, often associated with waning processes and usually caps facies successions (i.e., Tempestites, WESFGs, Bouma sequences) (Bouma, 1962; Walker et al., 1983; Myrow et al., 2002; Suter, 2006; Macquaker et al., 2010). If bioturbation is absent, this facies was likely deposited rapidly. If bioturbation is present, it suggests that the deposition happened gradually, providing organisms time to establish themselves in the sediment (Reineck and Singh, 1968; MacEachern et al., 1999; Ichaso and Dalrymple, 2009).

Facies 9: Muddy Carbonate

Muddy carbonates were found throughout the entirety of the core, composed of fossil fragments and/or carbonate cement (Fig. 17). At the macro-scale, fossil fragments include *Inoceramidae* (Fig. 17A), which was the dominant fossil found throughout. Fragments were observed to be associated with structureless, parallel laminated and rippled facies. Microfossils were also present including foraminiferal tests that have been infilled/replaced by calcite. Carbonate cement was observed typically surrounding framework grains. Thicknesses of this facies range from very thin lamina of 0.1mm to thin beds of 3cm.

Interpretation

Low faunal diversity and ubiquity of benthic organisms such as the *Inocerimidae* suggest dysoxic conditions versus anoxic conditions. Oxic conditions would yield greater faunal diversity (Brett and Allison, 1998; Schieber et al., 2016). Fragmentation of inoceramid shells indicate transport before deposition and was not *in situ* (e.g., Kiel et al., 2008). Association with ripples suggest transport by bottom current processes from a different location. Fragments that were within parallel laminated facies suggest slow deposition from suspension settling (Fig. 17C). The presence of pelagic foraminiferal tests further refutes sea-floor anoxia, and the diagenetic infill/replacement of the foraminiferal test suggest lower sedimentation rates, allowing more time for calcite to diagentically change the foram chambers (Li and Schieber, 2018). High carbonate content is an indication of hemiplegic deposition, where sedimentation rates are low. Further evidence of this is seen by the presence of diagenetic calcite and dolomite within foraminiferal tests, as they require time to precipitate out of the water. However, diagenetic material may be formed post-deposition and have no direct implications of sedimentation rate and deposition.

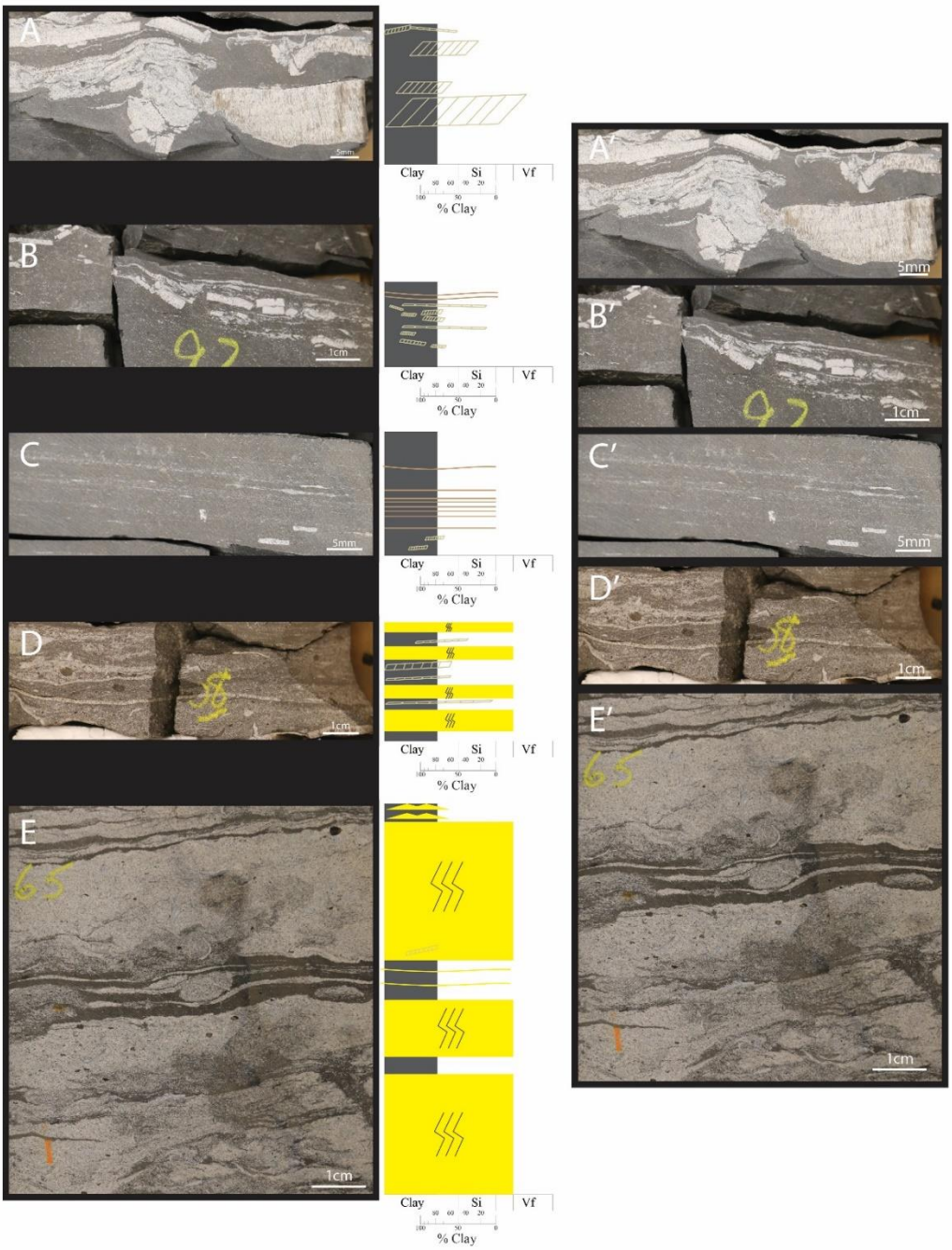

Fig. 17. Photographs highlighting A). Relatively thick inoceramid fragments in structureless mudstone at 7230.40ft. B). A concentrated mass of inoceramid fragments found with silt and sand laminations at 7192.95ft C). Few thin inoceramid fragments found within silt laminations at 7229.90ft. D). A mixture of fossil fragments at 7208.50ft E) Massive bioturbated sandstones, cemented with calcium carbonate, and interbedded with thin wavy sand laminations. Generic sandy ripples occur within muddy intervals.

Facies 10: Flaser and Wavy Bedding

Flaser and Wavy bedding are characterized by a heterolithic deposit (Fig. 18). In figure 18, two examples are provided, figure 18A represents a wavy bedded heterolithic deposit, and figure 18B represents a flaser bedded heterolithic deposit. Individual laminations in figure 18A are less thick compared to laminations in figure 18B. Wavy bedded heterolithics (Fig. 18A) were identified by mud layers overlying ripple crests and troughs. It can only be called wavy bedding when there is a sequence of mud and sand rippled layers, wherein both the mud and sand layers are continuous as seen in figure 18A. Flaser bedding can be wavy as seen in figure 18B. Characterizing wavy flaser bedding are the discontinuity of mud layers that overly the rippled sands. Similarly to wavy bedding, it can only be called wavy flaser bedding when there is a sequence of intercalated mud and sand, wherein the sand layers are continuous, and mud layers are discontinuous. Both of these deposits show bipolar current ripples orientations and double mud-drapes

Interpretation

Flaser and wavy bedding are indicative of intermittent flows of higher velocity and lower velocity (Reineck and Wunderlich, 1968). The changes in current velocity is the result of slack water in between ebb and flow tides, which gives rise to the intercalated heterolithic deposit seen in this facies (Dalrymple, 2010). This facies is often indicative of tidal deposition, especially when bipolar current directions and double mud-drapes were observed (Fig. 18).

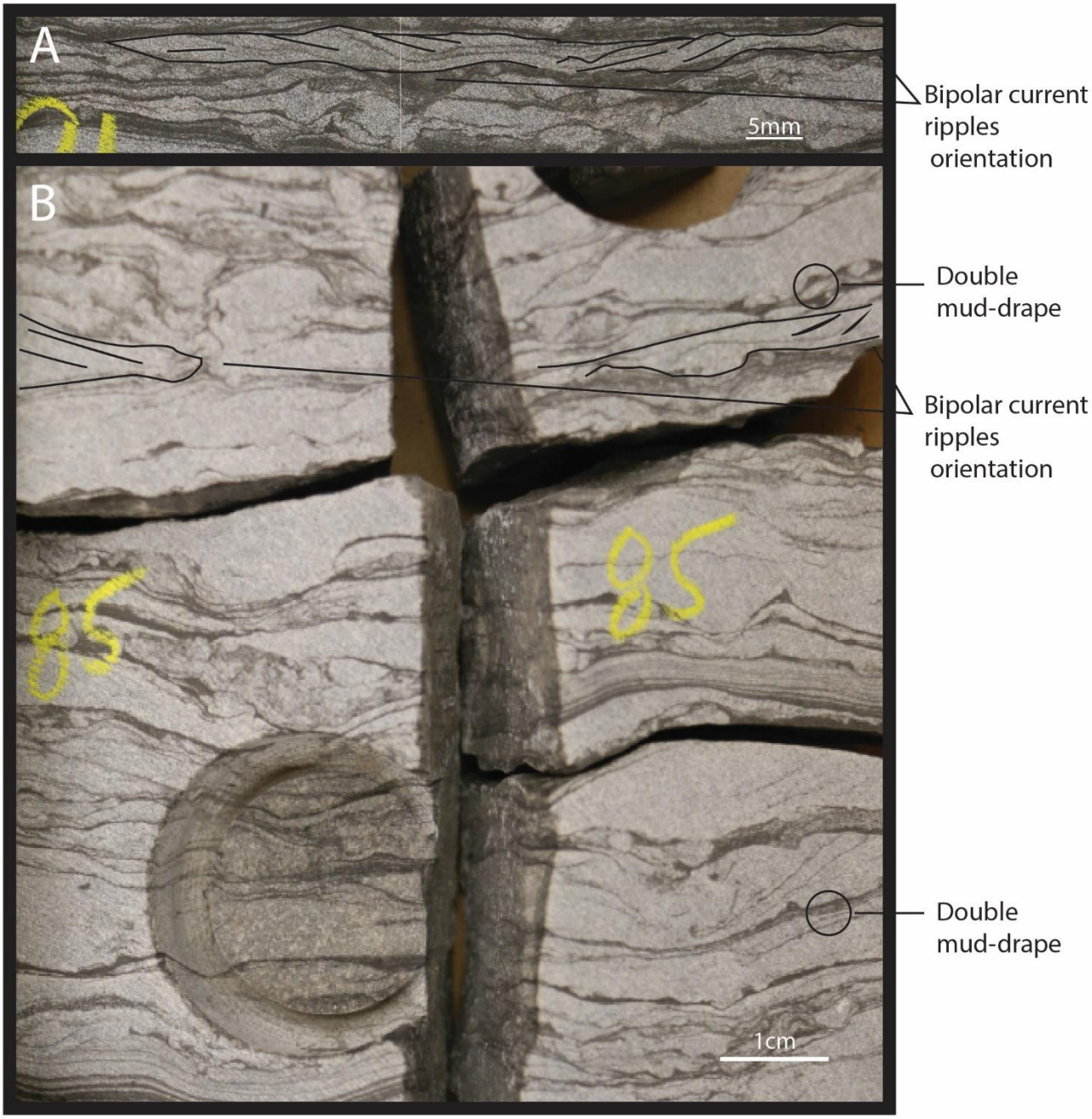

Fig. 18. Photographs highlighting flaser and wavy bedding. A). Wavy bedding, showing bipolar current ripple orientations at 7091.90ft. B). Wavy flaser bedding. Showing double mud-drapes and bipolar current ripples at 7085.80ft.

Facies 11: Bentonite Ash Layer

This facies was rare throughout the core and was found in two places, 7322.50ft and 7231.00ft (Fig. 19). These ash layers were considered as bentonites and were thinly bedded at approximately 3cm thick. Bentonite layers are light gray and yellow in colour, and are often fragmented.

Interpretation

Bentonites layers are composed of clay and are deposited by suspension settling of altered ash through the water column. These deposits are dominantly structureless and are interpreted to have been distributed by wind and deposited by ash-fall (Elder, 1988). Their presence in the core suggest a regional volcanic event and low sedimentation rates.

Fig. 19. Photographs highlighting bentonite ash layers A). A bentonite ash layer, sharply overlying silty and sandy parallel planar laminated mudstone at 7231.00ft. B). Fractured pieces of bentonite found at 7322.55ft.

4.2 Facies Association Identification and Interpretation

After the 11 facies were identified, a facies association was interpreted for a specific vertical succession of facies. These associations are based on the proposed processes that govern the transport of fine-grained sediment across or along the shelf including hypopycnal plumes, hyperpycnal flows, storm-setup relaxation flows, tempestites, and gravity driven fluid muds; all of which, except for hypopycnal plumes require sufficient bottom slopes to sustain movement (Bhattacharya and MacEachern, 2009; Schieber, 2016; Li and Schieber, 2018). Schieber (2016) summarized the potential offshore reach of processes such as tempestites, wave/tide/current aided hyperpycnal flows, wave/tide/current enhanced sediment gravity flows (WESGFs), and turbidites at a certain slope angle for water depths up to 200m. As mentioned earlier, the core was deposited ~220km offshore at the most distal, and ~110km offshore at the most proximal (Fig. 1, 3). Additionally, with water depths of ~100m, the slope angle of the seaway was approximately 0.026°- 0.04°. Therefore processes that were expected to be dominant include storms (tempestites), and wave and current enhanced sediment gravity flows (Fig. 20). However, the shoreline was spatially changing throughout time and sandier proximal deposits observed in this study may have been deposited by other processes such as ignitive turbidity currents. Therefore, the facies associations that were observed in this study include ignitive turbidite, storms (tempestite), WESGF, tidal, biogenic reworking, fluid mud, suspension settling, and generic bed load transport.

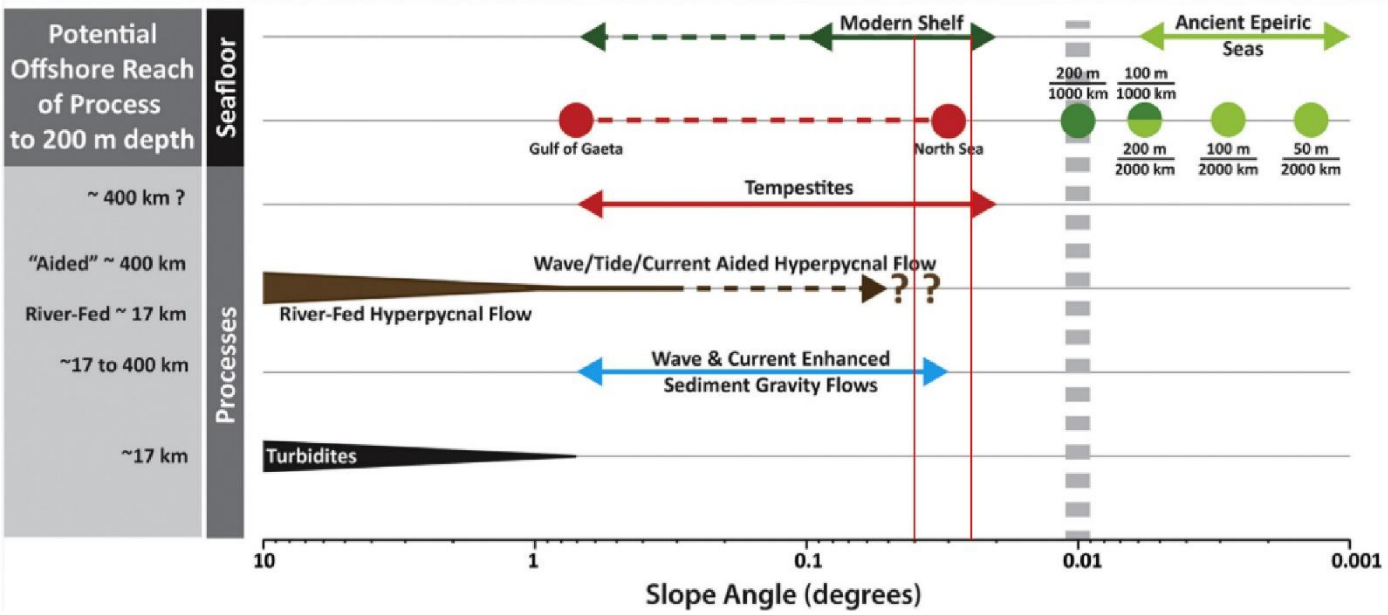

Fig. 20. Slope angles and potential offshore reach of processes for tempestites, wave/tide/current aided hyperpycnal flow, wave and current enhanced sediment gravity flows, and turbidites. Vertical red lines represent slope angles of seaway in this study from most proximal to distal (modified from Schieber, 2016).

Tempestites

The tempestite deposits observed in this study were similar to the wave-modified turbidites of Myrow et al. (2002). Their conceptualized model includes an upward succession consist of a scoured basal surface, graded bed, small-scale HCS, wave ripples, combined-flow ripple cross-lamination and a normally graded bed with a bioturbated cap (Fig. 21). It is interpreted that wave-modified turbidites are the product of the combination of waves and excess weight forces. It is however still considered a tempestite because storms play the dominant role in producing the waves, and enhancing excess weight forces by providing turbulence to suspended sediment concentration (Myrow et al., 2002). An example of a tempestite deposit found in this study is shown below (Fig. 22).

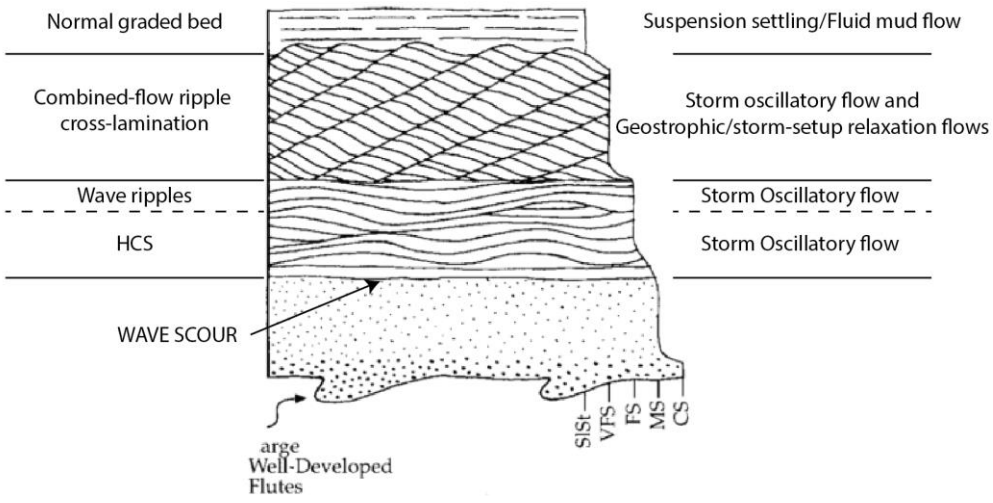

Fig. 21. Conceptualized model for the vertical succession of sedimentary structures in a wave-modified turbidite deposit, also known as a tempestite deposit. The model was observed in this study. Modified on the right are the depositional processes for associated sedimentary structures seen on the left (modified from Myrow et al., 2002).

Fig. 22. Example and line drawing of a tempestite deposit showing from an upward succession a basal wave scour, wave rippled laminations, combined-flow ripple laminations, wavy lamina set, and normally graded lamination. Taken from 7137ft.

Wave and current enhanced sediment gravity flows

River processes that produce hypopycnal plumes and hyperpycnal flows transport sediment offshore until they are deposited in prodelta or shelf areas with gentler slopes less than 0.7° and can no longer support their sediment load in autosuspension (Mulder et al., 2001; Bhattacharya and MacEachern, 2009; Schieber, 2016). However, there is a potential for resuspension by orbital wave motion or near bed currents to produce a liquid mud layer that can move on slopes as low as 0.03°. These wave and current enhanced sediment gravity flows can be dominantly bidirectional, unidirectional, or combined-flow depending on the magnitude of wave and current processes. A recent term "WESGFs" (Wave Enhanced Sediment Gravity Flows) has been coined for these type of flows (Macquaker et al., 2010), which encompasses wave and current processes that may have had enhanced sediment gravity flows (Schieber, 2016). Macquaker et al. (2010) proposed a diagnostic "triplet" facies succession that is indicative of wave and current enhanced sediment gravity flows, which is composed of an erosional surface overlain by curved ripple or combined-flow lamina set. Gradually overlying this is a wavy parallel lamina set, which is capped by a normally graded mud drape layer (Fig. 23). The depositional process interpreted from curved ripple or combined-flow ripple lamina set is the culmination of storm oscillatory flow with geostrophic, storm-setup relaxation, or tidal unidirectional flows. The wavy lamina set above is caused from storm oscillatory flow, and the normally graded bed capping the facies succession is

from suspension settling or fluid muds, depending on the presence of bioturbation. The complete triplet succession was observed in this study, however, individual units of the succession were more commonly found to be present (Fig. 16, 24). In figure 16B, wavy lamina sets underlying normally graded beds can be found and were interpreted to be analogous to the unit B and unit C of Macquaker et al. (2010) WESGF. Although seldom found, figure 24 exemplifies a complete WESGF. The scale of the WESGFs found in this study (Fig. 24) are comparable in scale to the ones found in Macquaker et al. (2010) (Fig. 23).

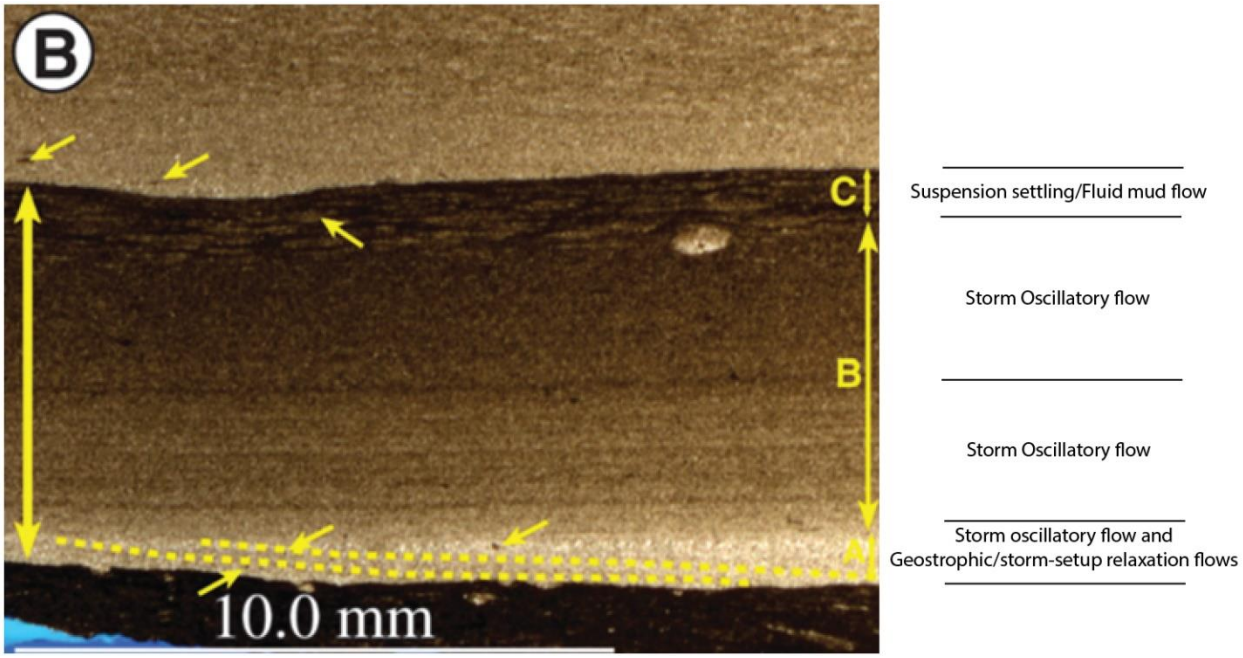

Fig. 23. Example of a WESGF deposit. Unit A exhibits combined-flow ripple cross lamination. Unit B has a wavy lamina set of intercalated silt and clay laminae. Unit C is a normally graded bed that is bioturbated (taken from Macquaker et al., 2010).

Fig. 24. Example of a WESGF deposit found in this study. A complete Macquaker et al. (2010) WESGF triplet facies succession is seen. Unit A, B and C are present.

Tidal Currents

It is suspected that tides play an important role in moving mud across the shelf, especially in epicontinental seas that have gentle slopes. Schieber (2016) suggested that tidal currents could have enough energy to move flocculated muds in bedload. Tidal deposits are characterized by tidal rhythmites, flaser/wavy/lenticular bedding, mud drapes (if bioturbation is present), and fluid mud (if bioturbation is not present) (Reineck and Wunderlich, 1968; Ichaso and Dalrymple, 2009). Tidal rhythmites are alternating silt/sand and clay deposits resulting from change in diurnal and neap-spring cycle current speeds (Mazumder and Arima, 2005; Williams, 1991). Flaser, wavy and lenticular bedding are deposits with alternating rippled sands/silt and clay (Fig. 25). The difference between flaser, wavy and lenticular bedding is represented by the amount of preserved clay. Environments with a higher amount of suspended clay will deposit wavy and lenticular bedding, compared to environments with a lower amount of suspended clay, which will deposit flaser bedding. Furthermore, higher energetic environments will preferentially deposit flaser bedding because stronger currents can erode previously deposited clay layers. During post ebb or flood tide, a mud drape will deposit overtop from suspension settling and will be commonly bioturbated. If bioturbation is absent, the mud layer is interpreted to have been deposited by fluid muds, which

accumulate relatively quicker (i.e., hours) (Ichaso and Dalrymple, 2009). Even though tidal deposits are associated with unidirectional flows, a combined-flow characteristic is often observed. This is due to two opposing current directions, and the overprinting of a ripple over another rounds the lee side and brink point, creating a reactivation surface of the underlying ripple. Careful examination is mandatory before classifying combined-flow ripples as tidal deposits. A good indicator that it is tidal in origin is the presence of bipolar current ripple orientations and double mud-drapes (Fig. 18, 26).

In figure 18, wavy bedding and flaser bedding were observed. They represent tidal deposition as the mud layers come in couplets, interpreted as double mud-drapes. Furthermore, the current, and combined-flow rippled sands show bipolar current orientations. This facies represents tidal ebb and flood, and slack water periods in between (Dalrymple, 2010). Figure 26 reveals clear bipolar ripple foresets and continuous mud layers suggesting it is wavy bedding. Unbioturbated muds suggest mud layers were deposited through fluid muds, which are commonly associated with tidal deposits (Ichaso and Dalrymple, 2009).

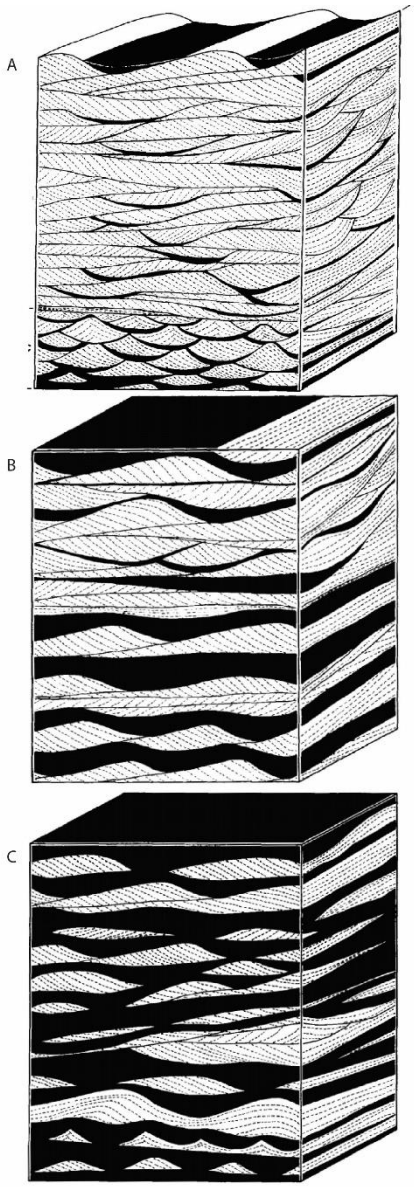

Fig. 25. A). Flaser bedding. B). Wavy bedding. C). Lenticular Bedding (modified after Reineck and Wunderlich, 1968).

Fig. 26. Example and line drawing of a tidal wavy bedding. Clear bipolar current ripple cross laminations can be seen. Taken from 7134.80'.

Ignitive Turbidity Currents

Ignitive turbidity currents occur from sediment instabilities, caused by river floods or storms that can carry sediment a few kilometers offshore, and are expected to be associated with proximal deposits. These turbidites require a slope of at least 0.7° to maintain autosuspension to keep its flow. Ignitive turbidites are represented by normally graded beds because they are associated with waning flows and show the T_A, T_B, T_C, T_D, T_E facies succession of a Bouma sequence (Bouma, 1962). However in mud-dominated deposits, T_C, T_D, and T_E divisions of the Bouma sequence are more commonly preserved (Fig. 27). Furthermore, the T_E division of the Bouma sequence can be further subdivided into three divisions as proposed by Piper (1978) known as "fine-grained turbidites". T_{E-1} is characterized by laminated mudstone, T_{E-2} as normally graded mudstone, and T_{E-3} as structureless mudstone (Li et al., 2015). Ignitive turbidites from sediment failure could also create differential compaction from rapid sedimentation rates (Alves, 2010). An example of an ignitive turbidite deposit is shown below (Fig. 28). It is interpreted that ignitive turbidites were triggered by

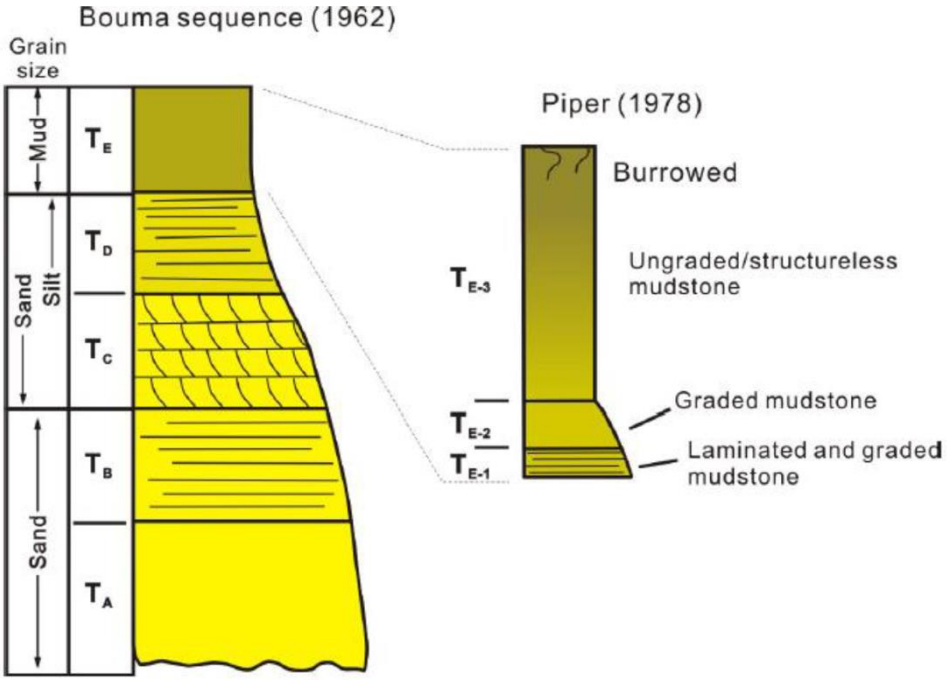

Fig. 27. The Bouma Sequence exhibiting normal grading. Divisions T_A, T_B, T_C, T_D, T_E can be seen. The additional TE subdivision as proposed by Piper (1978) is illustrated as subdivisions $T_{E-1,}$ T_{E-2}, and T_{E-3} (taken from Li et al., 2015).

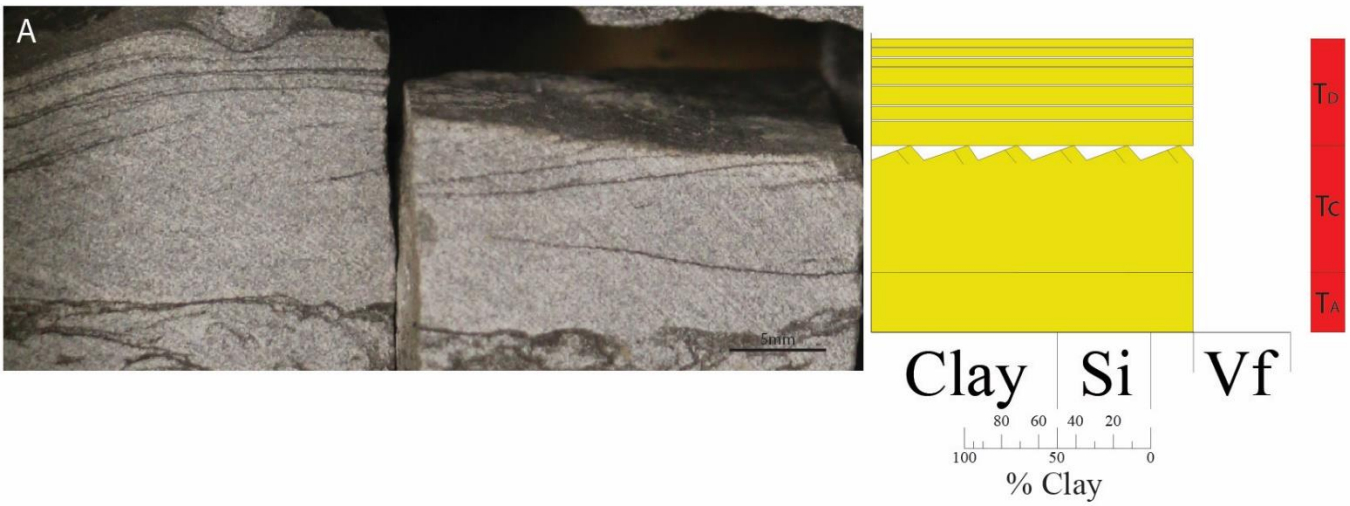

Fig. 28. A). Example of an ignitive turbidite deposit exhibiting the $T_{A,}$ $T_{C,}$ T_D Bouma divisions from 7085.00'.

4.3 Distinction between Depositional Processes and Sedimentary Structures

It is important to note that different depositional processes may create the same sedimentary structures, and currently a method does not exist to precisely differentiate identical sedimentary structures into separate depositional processes (Schieber, 2016; Yawar and Schieber, 2017). However, a summary of the 11 facies and their associated depositional processes is given below.

The structureless facies was interpreted three different ways depending on bioturbation intensity and lithology. A structureless sandstone was interpreted to have been deposited by an ignitive turbidite. A structureless mudstone with signs of bioturbation was associated with suspension settling, whereas a structureless mudstone with no signs of bioturbation is associated with fluid mud deposition. A completely bioturbated mudstone or sandstone was associated with biogenic reworking. Generic ripples were associated with a generic bed load transport process. Wave ripples were associated with tempestites. Combined-flow ripples were associated with three different processes including storms (tempestite), WESGFs, and tidal. However, the "triplet" facies succession of the WESGFs deposit proposed by Macquaker et al. (2010) was seldom seen, therefore a majority of combined-flow ripples were attributed to tempestites described as wave-modified turbidites by Myrow et al. (2002). Tidal deposits were interpreted only if bipolar current ripple orientations and double mud-drapes were seen. Current ripples can also be associated with three different processes including, ignitive turbidite, WESGFs, and tidal. However, in this study current ripples were mainly attributed to current or tide enhanced sediment gravity flows (CESGFs, TESGFs) as Schieber (2016) suggested that currents from trade wind circulation and tidal processes can interact with the sea bed and resuspend sediment to form enhanced sediment gravity flows. However for simplicity, all the enhanced sediment gravity flows will be referred to

WESGF, as the acronym is already established. Perhaps a more serviceable acronym should be developed to encompass current, tide and wave enhanced sediment gravity flows. Parallel laminations were mainly associated with tempestites and ignitive turbidites. Due to both processes being waning flows, it is expected to see parallel laminations for both. In order to make the distinction, other nearby structures must be considered. A tempestite deposit was interpreted when wavy parallel laminations were observed; whereas an ignitive turbidite deposit was interpreted when the T_a and T_c divisions of the Bouma sequence were seen. Normal grading was associated with suspension settling. Muddy carbonates were associated with tempestites, ignitive turbidites, or suspension settling; depending if adjacent structures were wave ripples, Bouma T_a and T_c divisions or normal grading/structureless respectively. Flaser and wavy bedding was associated with tidal. Bentonite ash layers were associated with suspension settling. A summary chart is provided in figure 29.

Facies	Facies Association
1) Structureless	Suspension Settling/Fluid mud/ Ignitive Turbidite
1a) Structureless Mudstone with Bioturbation	Suspension Settling
1b) Structureless Mudstone without Bioturbation	Fluid Mud
1c) Structureless Sandstone	Ignitive Turbidite
2) Bioturbated	Biogenic Reworking
3) Generic Ripples	Generic Bedload Transport
4) Wave Ripples	Tempestite
5) Combined-Flow Ripples	Tempestite
6) Current Ripples	WESGF
7) Parallel Laminations	Tempestite/Ignitive Turbidite
7a) Nearby Wave Ripples	WESGF
7b) Nearby Bouma Ta and Tc divisions	Ignitive turbidite
8) Normal Grading	Suspension Settling
11) Muddy Carbonate	Tempestite/Ignitive Turbidite/Suspension Settling
9a) Nearby Wave Ripples	Tempestite
9b) Nearby Bouma Ta and Tc divisions	Ignitive Turbidite
9c) Within normal grading/structureless	Suspension Settling
10) Flaser and Wavy Bedding	Tidal
11) Bentonite Ash Layer	Suspension Settling

Fig. 29. Chart summarizing facies associations interpreted for each facies seen in this study. Colours correspond to colours in facies key.

5. Results: Macro-, Meso-, Micro-scale Analysis

5.1 Macro-scale Analysis

Macro-scale analysis was used to identify candidate surfaces, parasequences, system tracts, sequences, upward variability in lithology, bioturbation intensity and net-to-gross. Furthermore, parasequences observed from this analysis were examined for broad lithological variability related to their interpreted sequence stratigraphic position within the core. Surfaces were identified when there was a change in grain size, sedimentary structures, and bioturbation intensity. However, it is important to note that without a regional correlation, sequence stratigraphic interpretations of surfaces in this study are ultimately candidate. Surfaces bounding upward-coarsening parasequences were identified by the increase in clay content and bioturbation intensity interpreted as a flooding surface. Individual parasequences were identified where grain size and thicknesses of laminations/beds gradually increased upwards. Sequence boundaries were identified by a sharp erosional contact, separating underlying finer deposits from overlying coarser deposits, and where there was a distinct increase in lamination frequency and thickness. Lowstand systems tracts (LST) were placed above sequence boundaries, and highstand system tracts were placed below (Posamentier and Vail, 1988; Van Wagoner et al., 1988; Van Wagoner et al., 1990). Overlying the LST is the transgressive surface, which marks the onset of finer sediment above and are characterized by a *Glossifungites* surface and a lag deposit pair, where the *Glossifungites* surface is found under the lag deposit. The transgressive surface marks the onset of sea level deepening and deposition of the transgressive systems tract (TST) above. The TST contains parasequences that gradually step farther landward in a retrogradational stacking pattern, in response to the sea level rise (Posamentier and Vail, 1988; Van Wagoner et al., 1988; Van Wagoner et al., 1990). Capping the transgressive systems tract is the maximum flooding surface, which is marked by the most

fine-grained deposit compared to adjacent deposits. Highstand systems tracts (HST) were placed above this surface (Fig. 6) (Posamentier and Vail, 1988; Van Wagoner et al., 1988; Van Wagoner et al., 1990). Furthermore, to give better confidence in interpretation, the well log was used to determine if observations made from the core correlated with the well log (Fig. 5). Furthermore, net-to-gross was calculated by adding the thicknesses of all sandstone intervals and dividing it by the total thickness of the core.

A total of 92 parasequences, 9 full systems tracts and 3 full sequences were observed. Out of the 92 parasequences, 91 coarsens upward and 1 fines upward (Fig. 6). The 92 parasequences are shown in figure 6, wherein the P1 represents parasequence at the bottom of the core, and P92 represents the top parasequence in the core. The core begins at the end of a sequence within a HST and ends at 23m. Above the HST is a LST that begins at 23m and ends at 27m before a TST begins at 27m and ends at 34m. Above the TST is a HST that starts at 34m until 45.5m. Above the HST is a significant decrease in grain size and bioturbation, and is interpreted to be overlain by a TST that begins at 45.5m until 50m. Above the TST is a HST starting at 50m and ending at 62.5m before a LST begins at 62.5m until 63m. Above the LST is a TST at 63m until 66m before the start of a HST at 66m until 91.5m. Above the HST is a LST at 91.5m until 100.5m and overlying the LST is a TST from 100.5 until the top of the core at 103m. To summarize, there are four HSTs, three LSTs, and four TSTs. The HST at the beginning and TST at the end are incomplete, making nine full system tracts. Furthermore, approximately 23m of the core is composed of sand, resulting in a net-to-gross of 23m:103m, 0.22 or 22%.

The entirety of the core was observed to be shoaling upwards, progressively becoming sandier up section (Fig. 6). Repeated system tracts were noticeably sandier near the top of the core compared to the bottom. For example, the HST, near the top of the core, contains significantly

more sand compared to the HST near the bottom. This trend can be explained by the paleoshoreline projections in figure 3, where the paleoshoreline is shown to move basinward as sea level regressed from early late Turonian to early Coniacian. Furthermore, individual parasequences were observed to vary in lithology depending on their sequence stratigraphic position (Fig. 6). Generally, the parasequences within LSTs become thicker and sandier as parasequences prograde. This can be seen from the four parasequences, parasequence 21 (P21), P24, P88, and P89 in their respective LSTs (Fig. 6). Parasequences within a TST become muddier up-section as parasequences retrograde. This was seen from the three parasequences, P30, P43, and P54. Parasequences within a HST typically aggrade then prograde, first becoming thicker then sandier up-section. This can be observed from the three parasequences P9, P33, and P80, which are sandier than the other underlying parasequences in their respective HSTs. Therefore, under macro-scale analysis, lithological vertical variability between parasequences were observed to be dependent on the sequence stratigraphic position.

5.1.1: Lithofacies and Environment of Deposition

Under macro-facies analysis, lithofacies were identified and were assigned to the core based on lithological properties. In Li and Schieber (2018), the lithofacies classification was used to interpret environment of deposition (EOD) across a shelf based on the relative proportions of carbonate, sand, and mud (Fig. 30). By using general relationships correlated with proximity to shoreline (i.e., calcareous content increases basinward, clastic dilution decreases basinward), they proposed a depositional model for the Cretaceous Tununk Shale in Utah. The lithofacies used in this study from most proximal to distal include muddy silty sandstone (MSS), carbonate-bearing muddy silty sandstone (CMSS), silty sandy mudstone (SSM), carbonate-bearing silty sandy mudstone (CSSM), carbonate-bearing silty mudstone to muddy siltstone (CMS), and silt-bearing

calcareous mudstone (SCM). This study modified the lithofacies classification used in Li and Schieber (2018) by adding two additional lithofacies members, the MSS and CMSS; and changing CMS to represent a more distal facies compared to CSSM (Fig. 30). In this study, these lithofacies categorizations provided broad lithofacies trends throughout the core; allowing a general understanding of spatial changes of the paleoshoreline and EOD through time. Lithofacies were observed to correspond with changes within a system tract and are shown in figure 6 and figure 30. The lithofacies associated with the first highstand observed in the core begins with a CMS and ends with a CSSM, interpreted as a shallowing from an outer shelf to middle shelf (Fig. 6, 30). The lithofacies for the LST above is a MSS and is interpreted to be deposited within a proximal lower shoreface. The TST above the LST grades into a SSM and becomes CSSM, interpreted as a deepening from an inner shelf to middle shelf. The HST above begins with CSSM and grades into a SSM then CMSS, interpreted as a gradual shallowing from a middle shelf to inner shelf to distal lower shoreface. Above is a TST that begins with a CMS then grades into a SCM and is interpreted as a deepening from a distal middle shelf to outer shelf. Above the TST is a HST with CSSM interpreted to be a middle shelf environment. The LST above is a CMSS interpreted to be a distal lower shoreface environment. The TST above begins with a CSSM and grades into a CMS suggesting a gradual deepening from a middle shelf to a distal middle shelf. The HST above begins at a CMS then grades into a CSSM then a CMSS, suggesting an overall shallowing from a distal middle shelf to middle shelf then distal lower shoreface. The LST above is a MSS interpreted to be deposited in a proximal lower shoreface environment. The TST above is a CSSM, interpreted to be deposited in a middle shelf environment. The transition of lithofacies through the core is presented in figure 30. From the depositional model proposed by Hart (2016), the core

portrays lithofacies in between zone 1 and zone 2 which includes siliciclastic mudstone and calcareous mudstone (Fig. 31).

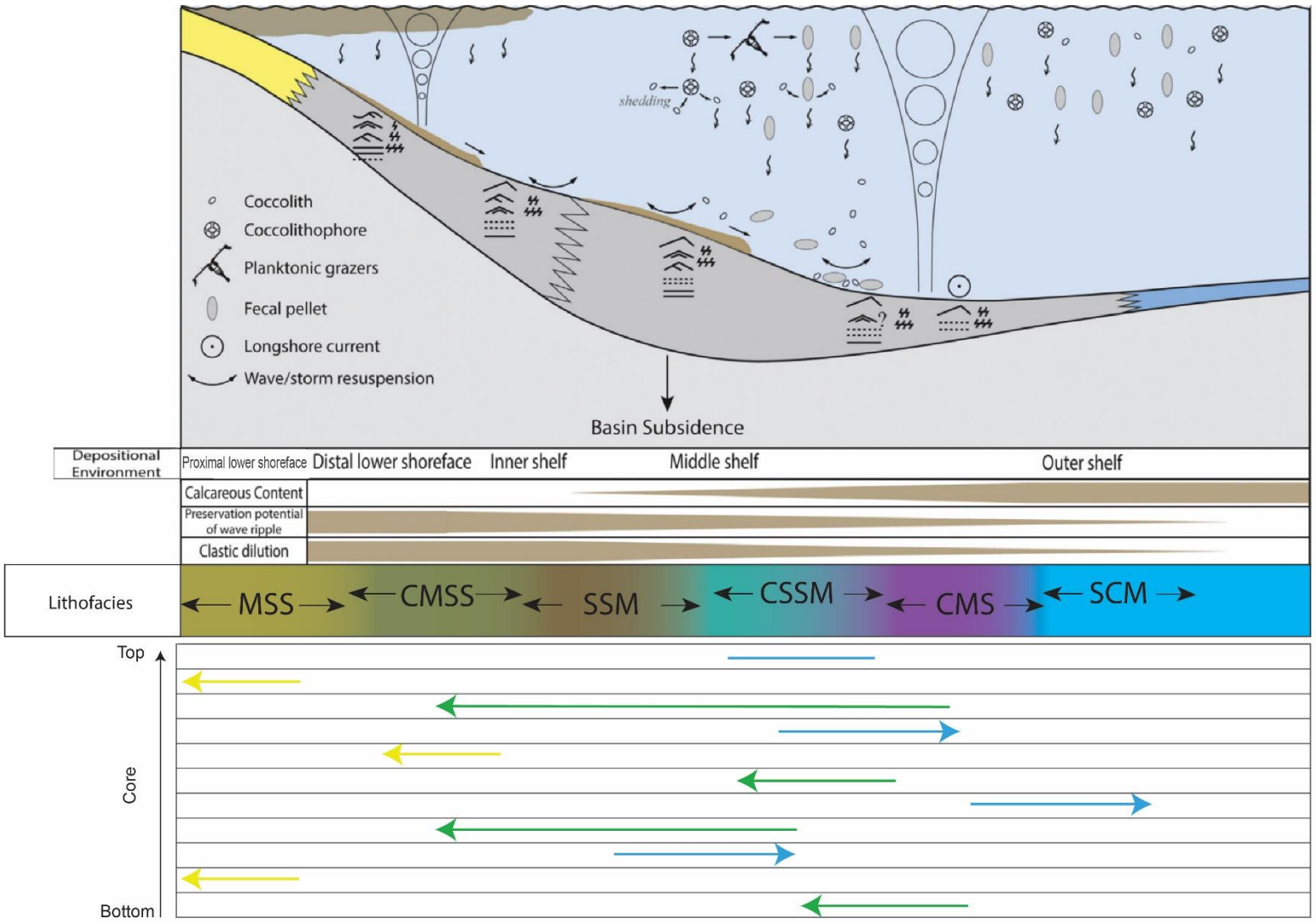

Fig. 30. Depositional model for Tununk Shale in the CWIS. The four lithofacies observed in their study are assigned to a depositional environment across shelf. Calcareous content is shown to increases further basinward; whereas preservation potential of wave ripple and clastic dilution decreases. The green, yellow and blue arrows indicate LST, HST, and TST respectively in the core. The bottom represents the bottom of the core and top represents the top of the core. Chart portrays the change lithofacies and environment of deposition transition throughout the core within each system tract (modified after Li and Schieber, 2018).

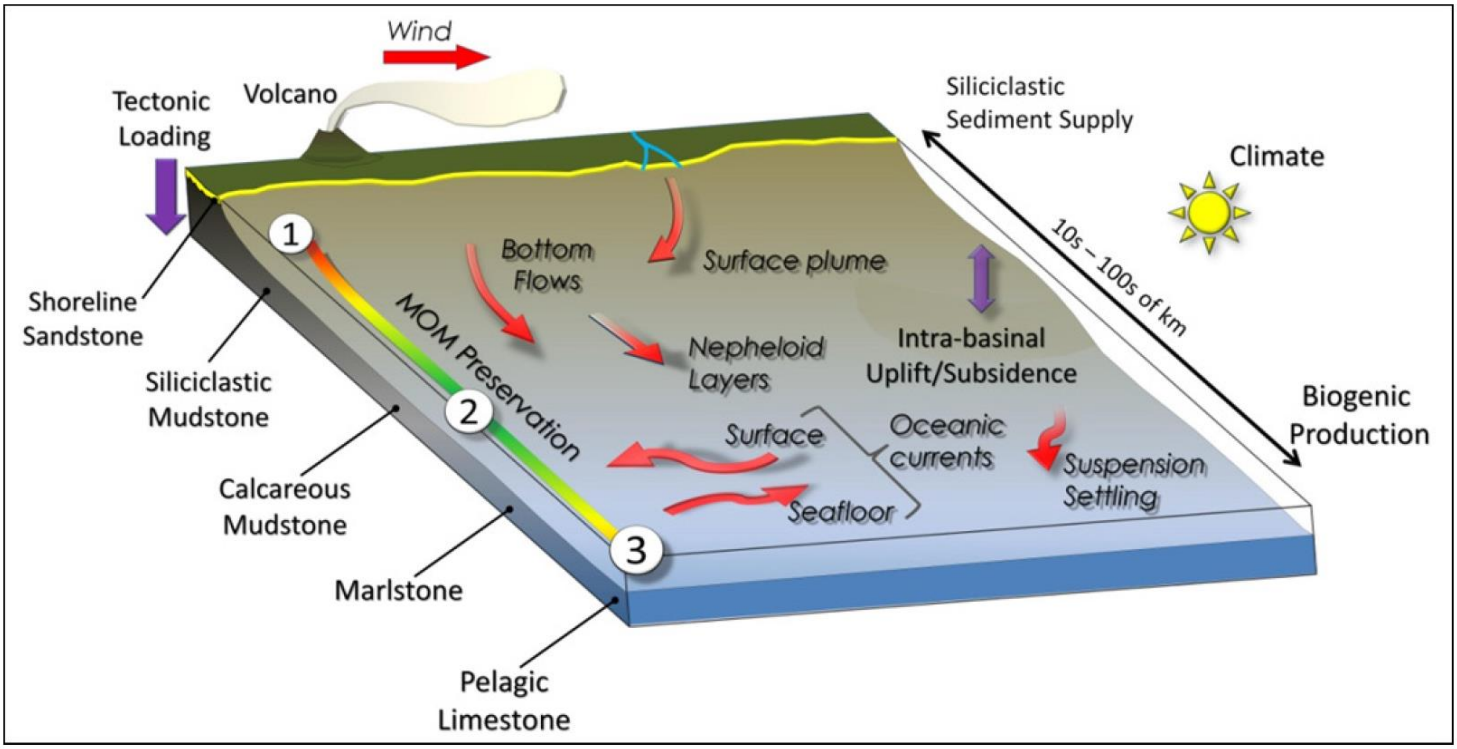

Fig. 31. Depositional model of the CWIS. The red arrows show the processes that transport sediment across the seaway. The most proximal deposit (shoreline sandstone) is dominated by coarse grained siliciclastic sediments. The most proximal mudstone deposit (siliciclastic mudstone) is dominated by clay, silt, and quartz. Further offshore siliciclastic input decreases and biogenic sediment increases forming calcareous mudstones. Marlstone and pelagic limestone are formed near the basincenter where biogenic production are highest. Marine organic matter (MOM) zones are labeled as 1-3, where 1 has low preservation potential for MOM, 2 have good MOM preservation potential, and 3 have low MOM content (taken from Hart, 2016).

5.2 Meso-scale Analysis

Macro-scale analysis was able to identify compositional variability within parasequences due to their different sequence stratigraphic positions within the core. However, to further examine parasequences, meso-scale analysis was done to identify variability in facies composition, facies successions, and depositional processes within ten individual upward-coarsening parasequences. Variability in sedimentary structures, clay content, lithology, facies, and bioturbation were examined at a millimeter-centimeter resolution. Sedimentary structure and clay content variations were portrayed using a stratigraphic log, where clay content and grain size is on the x-axis, and height is on the y-axis. Facies variability was organized in a chart, where on the x-axis are the eleven different facies, and on the y-axis is thickness. Lithology was portrayed by a graphic log, where percentage is on the x-axis divided by 10% intervals, and thickness is on the y-axis. The BI log was also included as a line graph, where BI index is on the x-axis, and thickness is on the y-axis. A total of ten parasequences were examined in detail. Selecting the parasequences for analysis was based on the availability of micro-scale data (i.e., thin-sections, SEM) from the Weatherford Laboratories' report. By selecting the parasequences with available micro-scale data, further analysis on minerology can be done. In addition to data availability, the samples selected by Weatherford Laboratories for analysis were well dispersed throughout the core, which provided the opportunity to analyse how the ten parasequences differed depending on their stratigraphic position within the core. The parasequences chosen for further meso-scale analysis are P9, P21, P24, P30, P33, P43, P54, P80, P88, and P89. The location of parasequences with respect to the core are shown in figure 6. Ultimately, the objective of this analysis was to observe the vertical variability of facies, facies association and lithology, and interpret vertical changes in depositional

process, as well as examine how the distribution of depositional processes differed depending on the stratigraphic position of the parasequences.

The distribution of facies throughout each parasequence are shown in percentages, and were further categorized into primary, secondary, and tertiary facies (Fig. 32). Depending on the distribution of facies, the depositional process associated with each facies succession was determined to have had either dominated, influenced or affected the deposition of the parasequence (e.g., Ainsworth et al., 2011) (Fig. 33). To further classify depositional process, a ternary diagram similar to Ainsworth et al. (2011) was modified to show which process, biogenic reworking (*B*), suspension settling (*S*), or bedload transport (*T*) dominated, influenced or affected the deposition of the parasequences; which are determined by the distribution of facies successions (Fig. 33). Bedload transport was further categorized to be wave (*W),* tidal (*T)* or generic (*G*) dominated, influenced, or affected. A fluvial categorization was not included because its percentage is negligible in this study. For example, if a parasequence was biogenic reworking-dominated, bedload transport-influenced, and suspension settling-affected, it would be denoted by *Bts;* in which the dominant process is first, followed by the influenced and affected processes. For further bedload transport categorization, if bedload transport was wave-dominated, tidal-influenced and generic-affected, then it would be denoted by *Wtg* (Fig. 34). Bedload transport include ignitive turbidites, which were attributed to be wave-dominated, as it was interpreted to have had been most likely from storm resuspension (Piper and Normark, 2009); tempestites, which are attributed to be wave-dominated as they are formed by storms; WESGFs, which are attributed to a wave-dominated process as they are interpreted to be caused by storms; tides, which are attributed to a tidal process; and fluid mud, which was attributed to a wave or tidal process, as both processes can form fluid muds (Ichaso and Dalrymple, 2009; Piper and Normark, 2009). The

distinction was made if fluid muds were adjacent to tempestites, or flaser and wavy bedding, in which case, the fluid mud was attributed to a wave-dominated process near tempestites and a tidal process near flaser and wavy bedding.

Two charts were made to summarize the distribution of facies and facies associations observed; where the green, yellow, and red indicate primary, secondary, and tertiary facies in figure 32, and dominant, influenced, and affected facies associations for figure 33, respectively. Two ternary diagrams were made to classify dominant depositional process for each of the ten parasequences shown in figure 34.

5.2.1 Parasequence Observations and Interpretation

All ten parasequences coarsen and increase in sand content upwards (Fig. 35-44). Bioturbation intensity was found to decrease and become increasingly variable up-section in all parasequences except for P33 (Fig. 39) and P43 (Fig. 40). Bioturbation intensity typically decreases when rippled facies were present. Thicknesses of parasequences were variable, ranging from 63cm-220cm.

Summarized in figure 32, the distribution of primary, secondary and tertiary facies found for each parasequence are as follows. For P9 (Fig. 35) and P21 (Fig. 36), bioturbated is primary, generic ripples are secondary, and wave ripples are tertiary. P24 (Fig. 37), only had two facies, the primary is bioturbated, and wave ripples are secondary. For P30 (Fig. 38), bioturbated is primary, current ripples are secondary, and wave ripples are tertiary. For P33 (Fig. 39), bioturbated is primary, wave ripples are secondary, and generic ripples are tertiary. For P43 (Fig. 40), parallel laminations are primary, wave ripples are secondary, and carbonate is tertiary. P54 (Fig.41) had the same order as P33. For P80 (Fig. 42), combined-flow ripples are primary, wave ripples are

secondary, and bioturbated is tertiary. For P88 (fig. 43), bioturbated is primary, combined-flow ripples are secondary, and wave ripples are tertiary. For P89 (Fig. 44) Combined-flow ripples were primary, generic ripples were secondary, and flaser and wavy bedding were tertiary. To summarize, a chart is provided below in figure 32.

As for the distribution of facies successions for each parasequence, a chart is given and summarized in figure 33. For P9 (Fig. 35) and P21 (Fig. 36), the dominant process was biogenic reworking, influenced by tempestites, and affected by bedload transport. P24 (Fig. 37) was dominated by biogenic reworking and influenced by tempestites. P30 (Fig. 38) was dominated by biogenic reworking, influenced by tempestites, and affected by WESGFs. P33 (Fig. 39) was dominated by biogenic reworking, influenced by tempestites and affected by generic bedload transport. P43 (Fig. 40), was dominated by WESGFs, influenced by tempestites, and affected by suspension settling. P54 (Fig. 41) was dominated by biogenic reworking, influenced by tempestites, and affected by generic bedload transport. P80 (Fig. 42) and P88 (Fig. 43) were dominated by tempestites, influenced by biogenic reworking, and affected by tidal processes. P89 (Fig. 44) was dominated by tempestites, influenced by generic bedload transport, and affected by tidal processes.

Regarding depositional processes (Fig. 33), P9 is biogenic reworking-dominated, bedload transport-influenced, and suspension settling affected (*Bts)*, P21 is *Bts*, P24 biogenic reworking-dominated and bedload transport-influenced (*Bt*), P30 is *Bts*, P33 is *Bts*, P43 is bedload transport-dominated and suspension settling-influenced (*Ts)*, P54 is bedload transport-dominated, biogenic reworking-influenced and suspension settling-affected (*Tbs*). P80 is *Tbs.* P88 is *Tbs.* P89 is bedload transport-dominated, and biogenic reworking-influenced (*Tb*) (Fig. 33, 34). Furthermore, by examining the distribution of facies associations, it can be concluded that there was a change

from biogenic reworking-dominated processes within the first five parasequences, to mostly bedload transport-dominated processes within the last five parasequences.

Interpretation

Upward-coarsening parasequences are the product of gradual decrease of water depth and a progradational shoreline trajectory (Van Wagoner et al., 1988; Van Wagoner et al., 1990). The decrease in BI and increase in BI fluctuations upward are correlated with the upward coarsening of parasequences. This occurs because bioturbation intensity is dependent on water depth, energy levels, and sedimentation rates (MacEachern et al., 2005). As parasequences shoal upwards, energy levels and sedimentation rates generally increase, creating an environment more stressful for organisms to colonize, and BI ultimately decreases (Schieber et al., 2016; MacEachern et al., 2005). Furthermore, BI fluctuations were seen to increase upwards because as water depths become shallower, more events are capable of interacting with the sea bed, decreasing BI. Subsequent to an event, if given enough time (around six months) organisms could recolonize and BI would ultimately increase again; thus creating an alternating pattern of high-low BI (MacEachern et al., 2005). An example of this BI trend is seen in P30 (Fig. 37). Furthermore, certain facies successions become increasingly prevalent as a parasequence and the core shoals (Fig. 6, 33). It is typically seen that tempestites and tidal processes dominate the upper portions of a parasequence and of the core, while biogenic reworking and suspension settling dominate the lower portions of a parasequence and of the core (Fig. 6, 34-43). This pattern is apparent in parasequence 88 (Fig. 42). From these observations, it can be interpreted that high energy events such as tempestites and tides became increasingly prevalent as water depth decreases, and biogenic reworking occurs frequently within deeper waters. Given the distribution of facies succession, bedload transport processes dominate the top of the parasequences and core, and have less

contribution within bottom of parasequences and core where the dominant process is dominantly biogenic reworking. Therefore just as lithological variability was observed to be related to sequence stratigraphic position, vertical variability in facies distribution, facies successions and dominant depositional process within parasequences are also dependent on the sequence stratigraphic position, as well as their natural upward shoaling succession.

Facies	Facies Association	P9	P21	P24	P30	P33	P43	P54	P80	P88	P89
1) Structureless	Suspension Settling/Fluid mud/ Ignitive Turbidite				5%		19%	2%	3.5%	2%	6%
1a) Structureless Mudstone with Bioturbation	Suspension Settling										
1b) Structureless Mudstone without Bioturbation	Fluid Mud										
1c) Structureless Sandstone	Ignitive Turbidite										
2) Bioturbated	Biogenic	83%	92%	99%	41%	59%		33%	8%	37%	15%
3) Generic Ripples	Generic Bedload Transport	13%	6%		5%	9.5%	6.5%	22%	4.5%	8%	28%
4) Wave Ripples	Tempestite	3%	1%	1%		25%	25%	26%	39%	21%	13%
5) Combined-flow Ripples	Tempestite/Tidal				8%	3.5%	5%	3%	45%	28%	38%
6) Current Ripples	WESGF				20%		12%	4%		1%	
7) Parallel Planar Laminations	Tempestite/Ignitive Turbidite/WESGF						32%	6%	0.5%	1%	
7a) Nearby Wave Ripples	Tempestite										
7b) Nearby Bouma Ta and Tc divisions	Ignitive turbidite										
8) Normal grading	Suspension Settling	1%	1%		2%	3%	0.5%	4%	0.5%	1%	
9) Muddy Carbonate	Tempestite/Ignitive Turbidite/Suspension Settling				4%	2%	12.5%	17%	3%	1%	
9a) Nearby Wave Ripples	Tempestite										
9b) Nearby Bouma Ta and Tc divisions	Ignitive Turbidite										
9c) Within normal grading/structureless	Suspension Settling										
10) Flaser and Wavy Bedding	Tidal									17%	16%
11) Bentonite Ash Layer	Suspension Settling										
Parasequence Thickness (cm)		106	106	90.5	152	84	68	63	166	220	112
System Tract		HST	LST	LST	TST	HST	TST	TST	HST	LST	LST

Fig. 32. Chart summarizing the relative distribution in percentages of facies through each of the ten parasequences. The facies association for each facies is also included. The green, yellow and red indicate the primary, secondary, and tertiary facies observed, respectively.

Facies Association	**P9**	**P21**	**P24**	**P30**	**P33**	**P43**	**P54**	**P80**	**P88**	**P89**
Ignitive Turbidite								2.5%		6%
Tempestite	3%	1%	1%	27%	28.5%	30%	29%	80.5%	33%	35%
WESGF				20%		44%	10%		1%	
Tidal								3%	17%	16%
Biogenic Reworking	83%	92%	99%	41%	59%		33%	8%	37%	15%
Fluid Mud						9%	1%	1%	1%	
Suspension Settling	1%	1%		7%	3%	10.5%	5%	0.5%	3%	
Generic Bedload Transport	13%	6%		5%	9.5%	6.5%	22%	4.5%	8%	28%
System Tract	HST	LST	LST	TST	HST	TST	TST	HST	LST	LST
Process Classification										
Biogenic (B)	83%	92%	99%	41%	59%		33%	8%	37%	15%
Suspension Settling (S)	1%	1%		7%	3%	10.5%	5%	0.5%	3%	
Bedload Transport (T):	16%	7%	1%	52%	38.0%	89.5%	62%	91.5%	60%	85%
Generic (G)	81%	86%		1%	25%	1%	35%	5%	13%	33%
Wave (W)	19%	14%	100%	99%	75%	99%	65%	92%	57%	48%
Tidal (T)								3%	30%	19%
Classification	*Bts*	*Bts*	*Bt*	*Bts*	*Bts*	*Ts*	*Tbs*	*Tbs*	*Tbs*	*Tb*
Bedload Transport Classification	*Gw*	*Gw*	*W*	*Wg*	*Wg*	*Wg*	*Wg*	*Wgt*	*Wgt*	*Wgt*

Fig. 33. Chart summarizing the relative distribution in percentages of facies association throughout each of the ten parasequences. The green, yellow and red indicate the dominant, influenced, and affected depositional process, respectively. Process classification is given, to show which processes dominated, influenced, or affected the deposition of the parasequence.

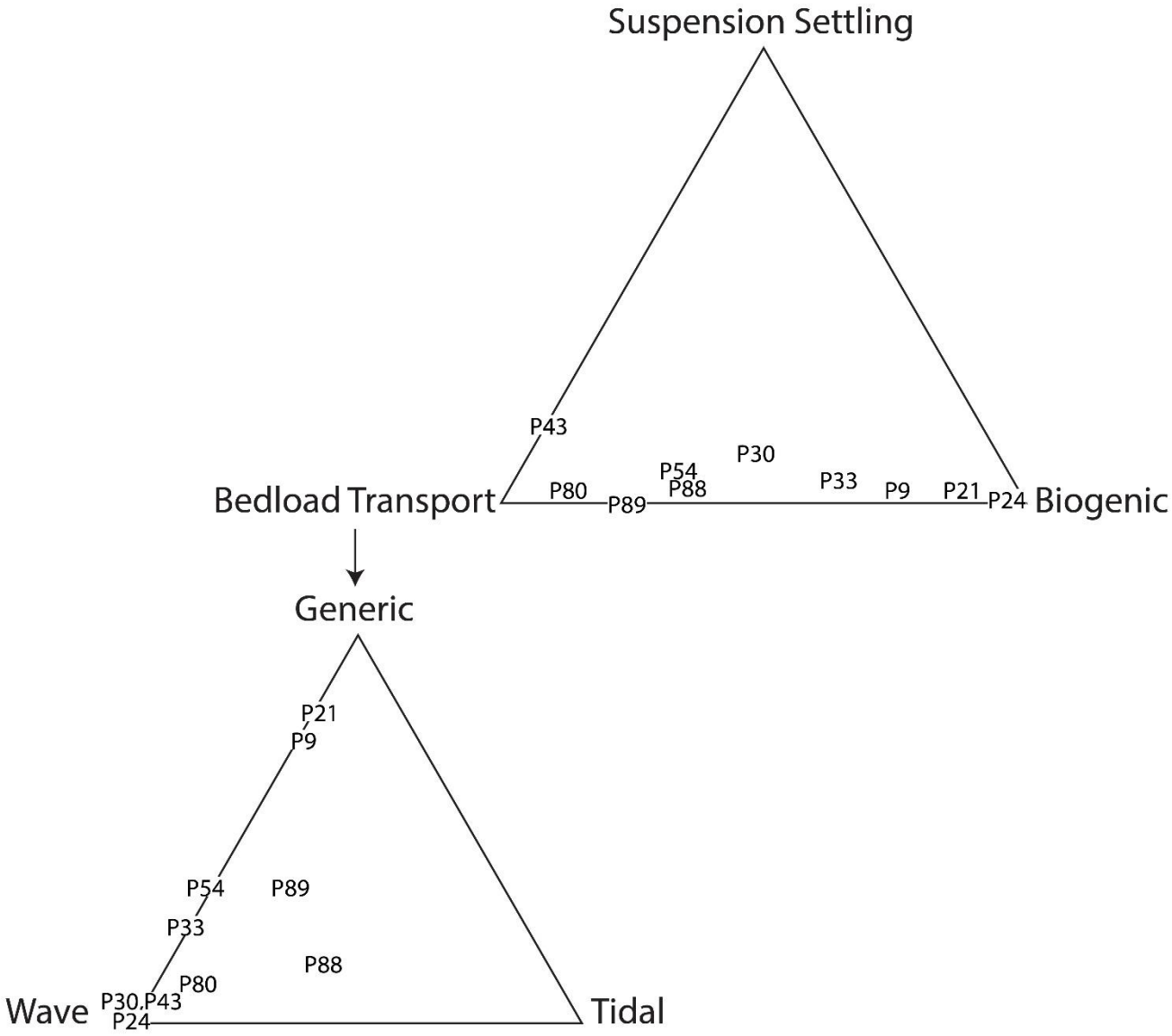

Fig. 34. Two ternary diagrams illustrating the classification of dominant depositional processes. Suspension settling, Biogenic reworking, and bedload transport are classified in the first ternary diagram. Bedload transport is further divided into generic, wave, and tidal processes.

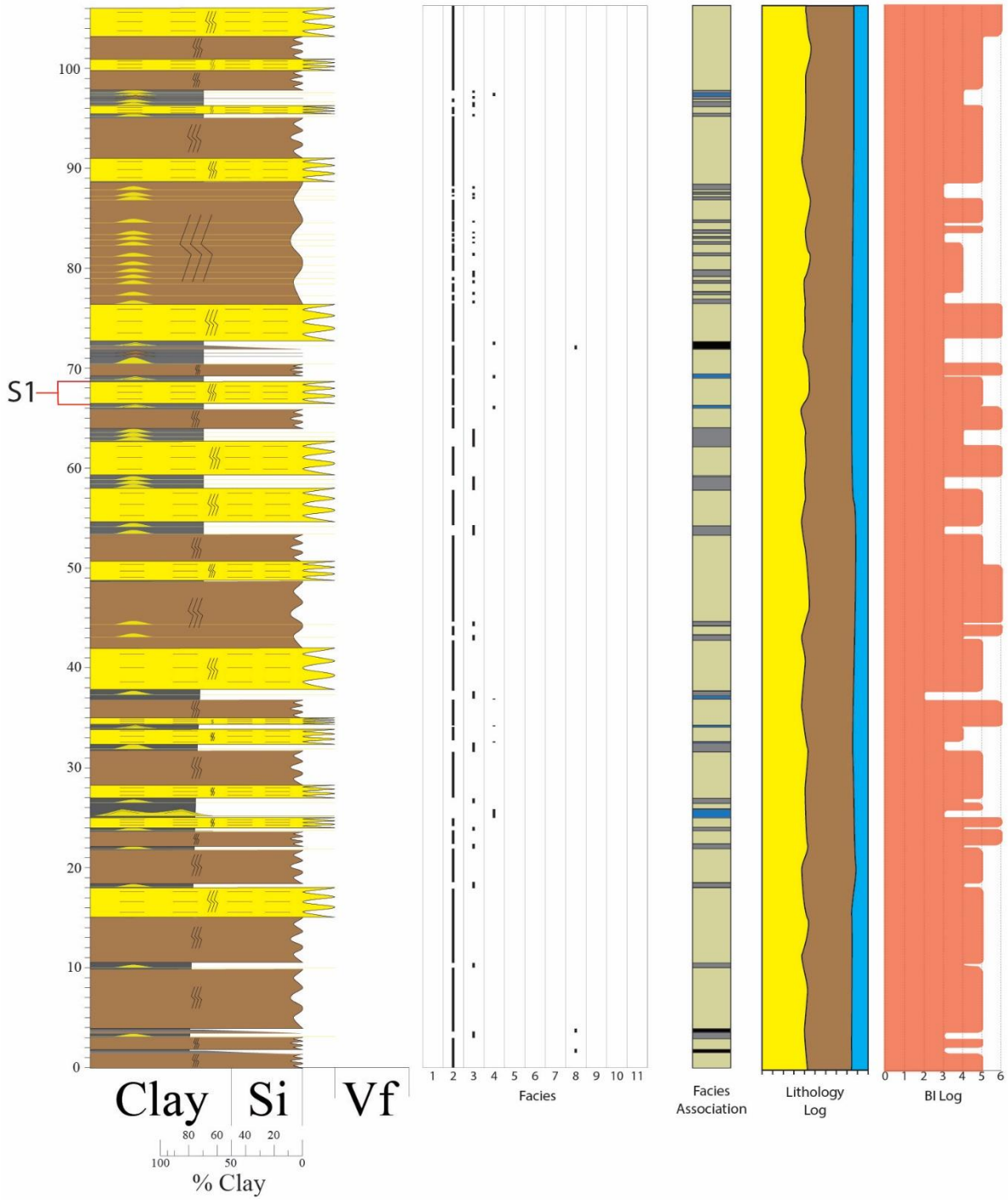

Fig. 35. Stratigraphic column, facies chart, facies association column, lithology graphic log, and BI log for parasequence 9. Sample 1 used for micro-scale analysis is highlighted by red bracket on the left. Parasequence 9 is from 7386'-7383'.

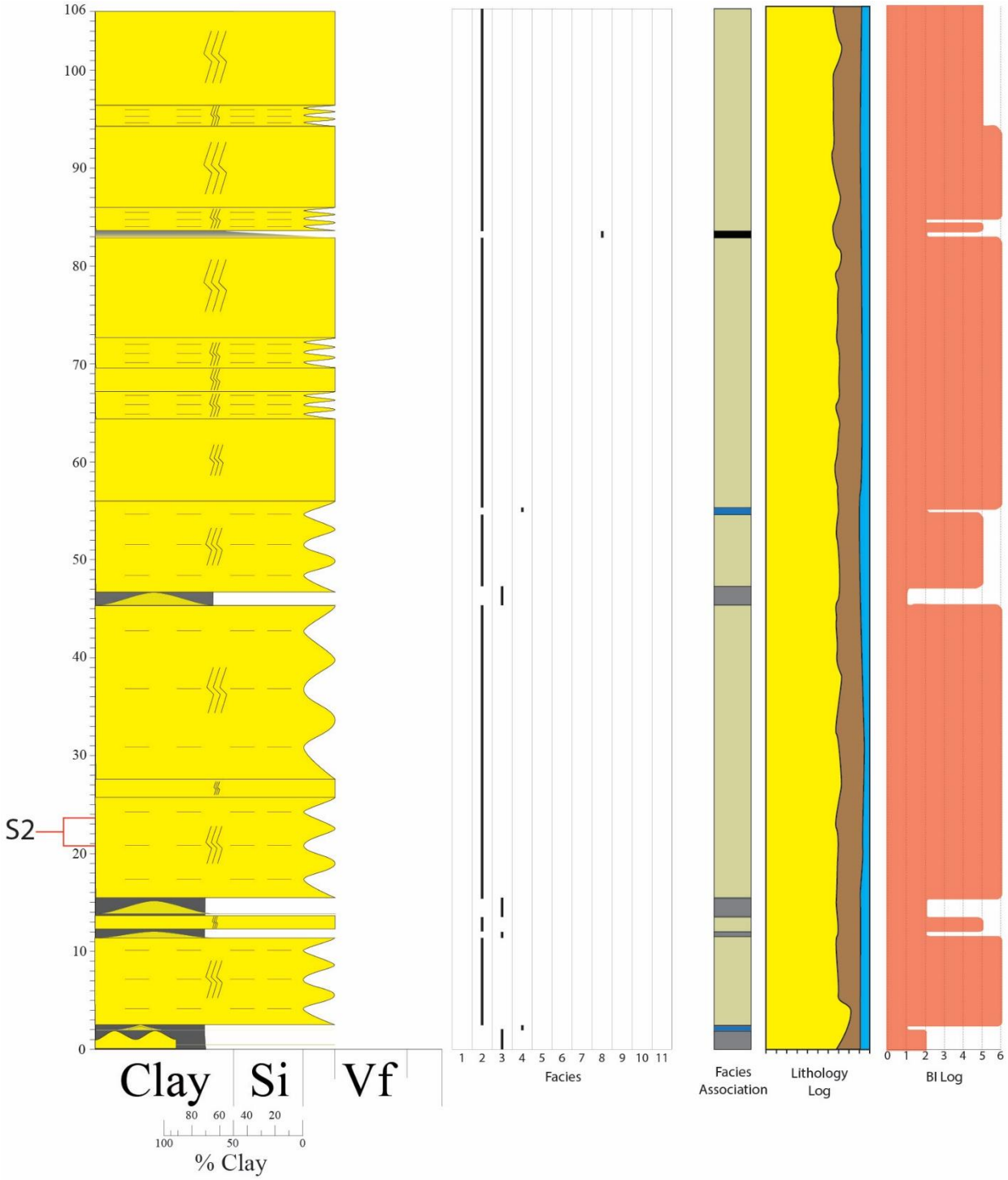

Fig. 36. Stratigraphic column, facies chart, facies association column, lithology graphic log, and BI log for parasequence 21. Sample 2 used for micro-scale analysis is highlighted by red bracket on the left. Parasequence 21 is from 7344'-7340.05'.

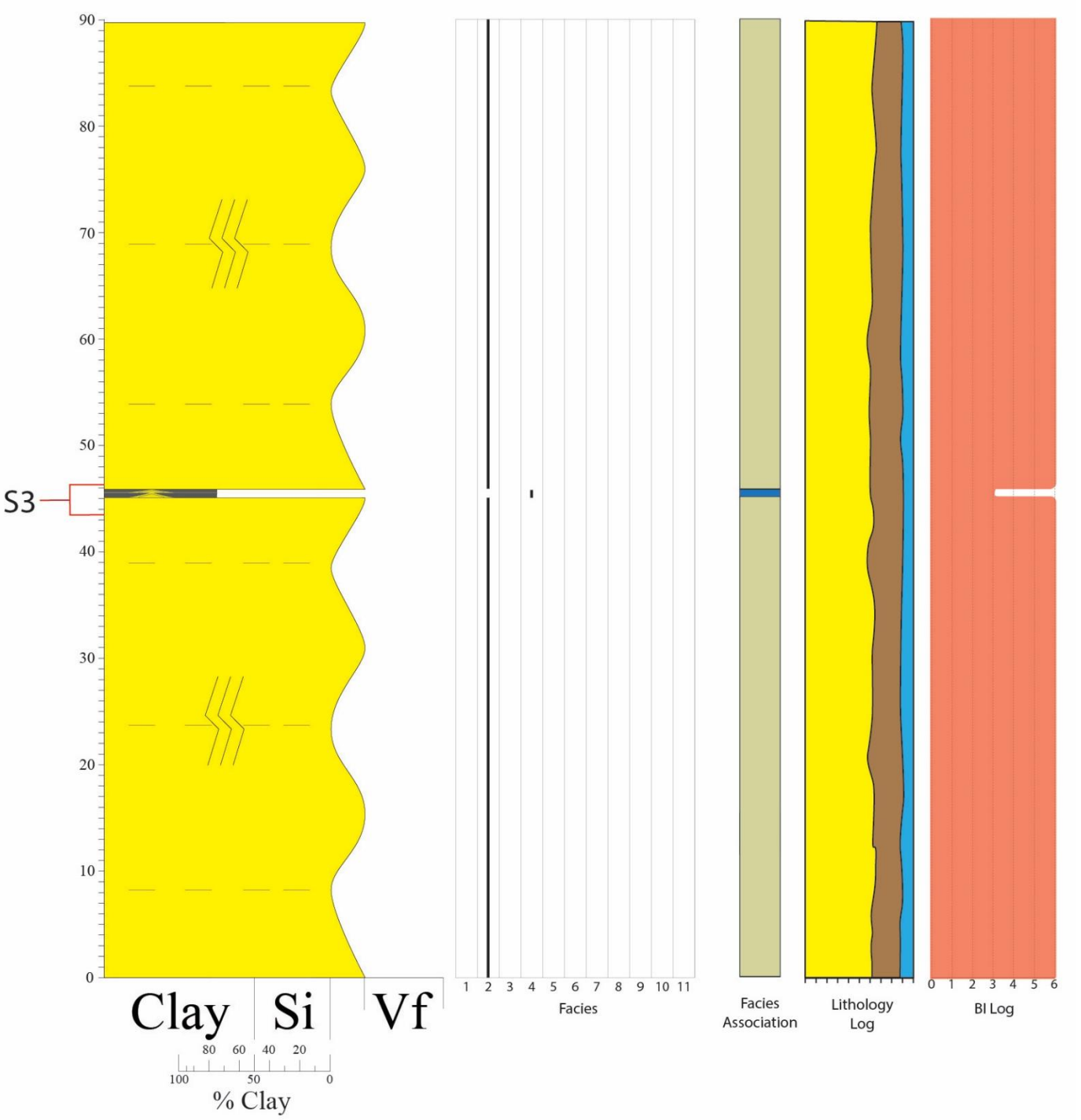

Fig. 37. Stratigraphic column, facies chart, facies association column, lithology graphic log, and BI log for parasequence P24. Sample 2 used for micro-scale analysis is highlighted by red bracket on the left. Parasequence 24 is from 7334'-7331'.

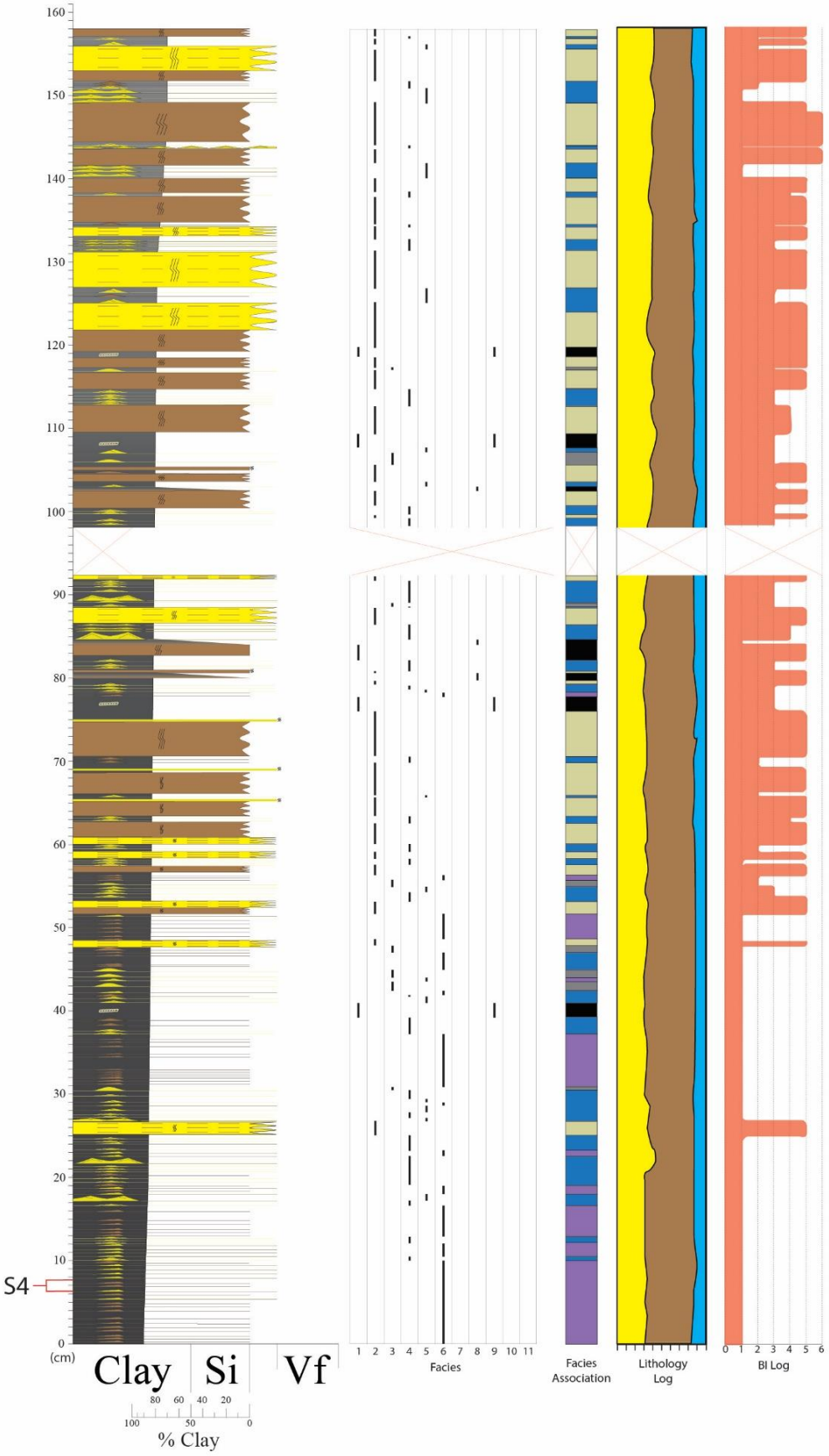

Fig. 38. Stratigraphic column, facies chart, facies association column, lithology graphic log, and BI log for parasequence 30. Sample 4 used for micro-scale analysis is highlighted by red bracket on the left. Parasequence 30 is from 7315.20'-7311.10'.

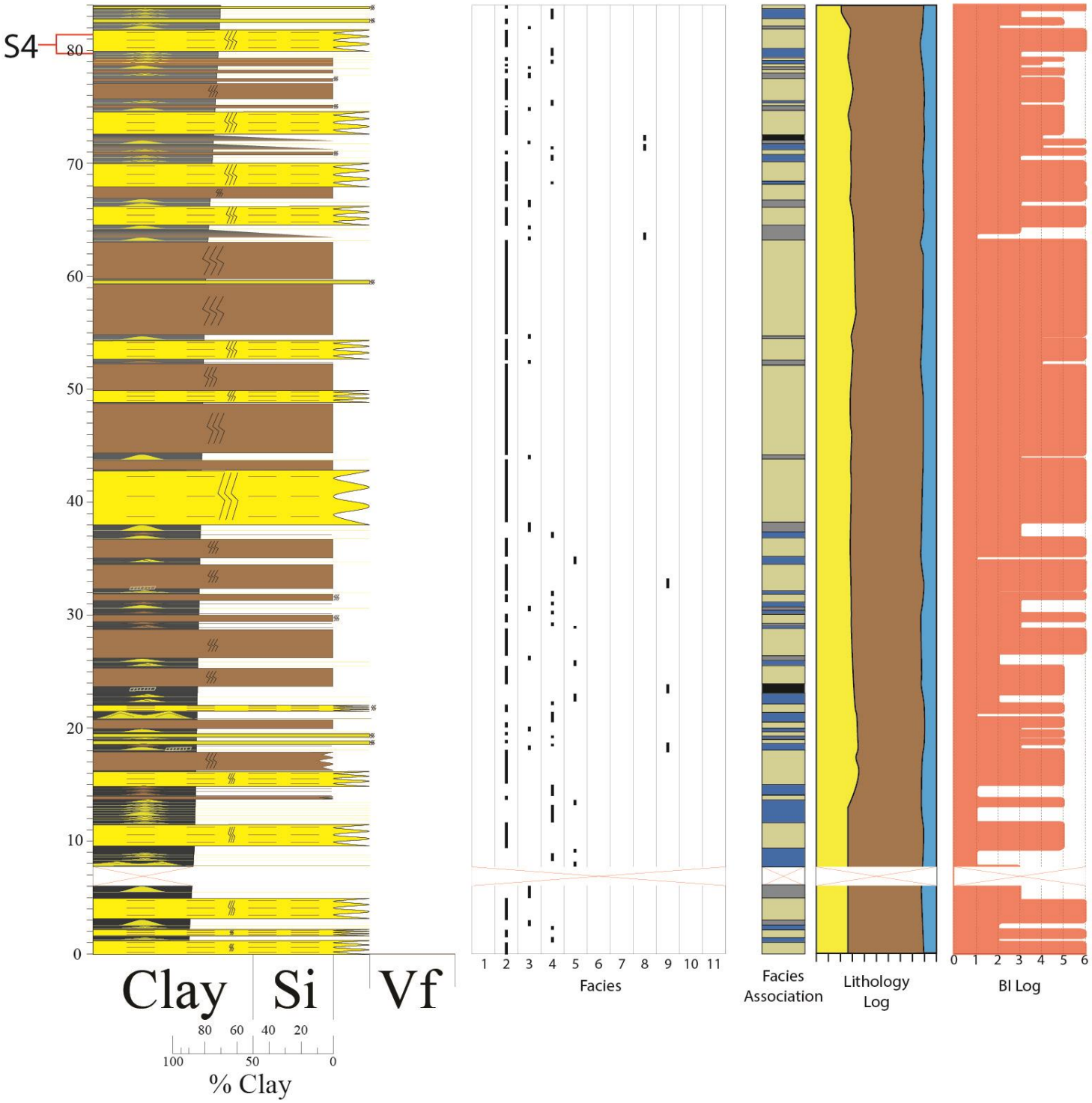

Fig. 39. Stratigraphic column, facies chart, facies association column, lithology graphic log, and BI log for parasequence 33. Sample 5 (S5) used for micro-scale analysis is highlighted by red bracket on the left. Parasequence 33 is from 7303.15'-7300.05'.

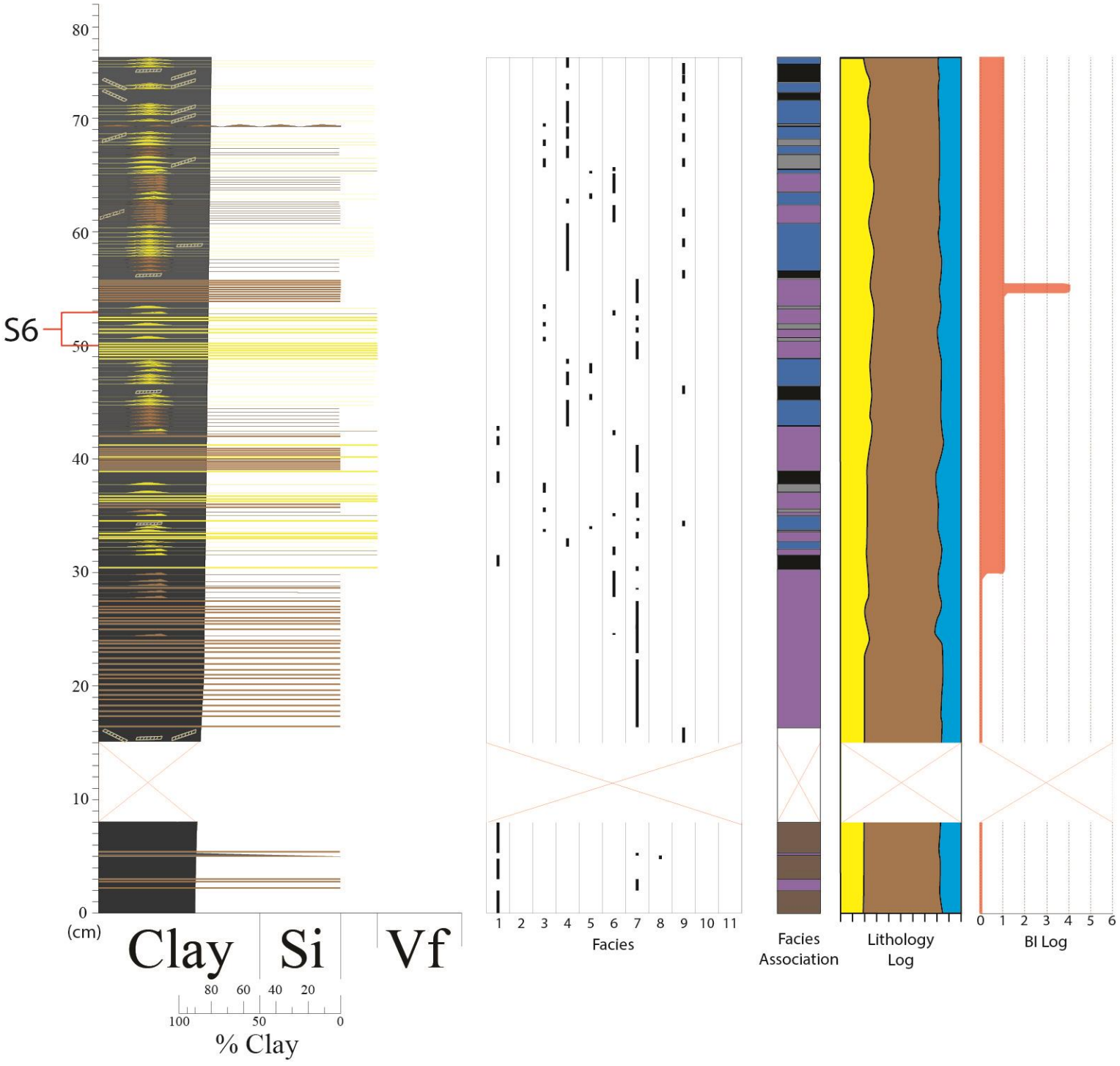

Fig. 40. Stratigraphic column, facies chart, facies association column, lithology graphic log, and BI log for parasequence 43. Sample 6 used for micro-scale analysis is highlighted by red bracket on the left. Parasequence 43 is from 7264.30'-7261.95'.

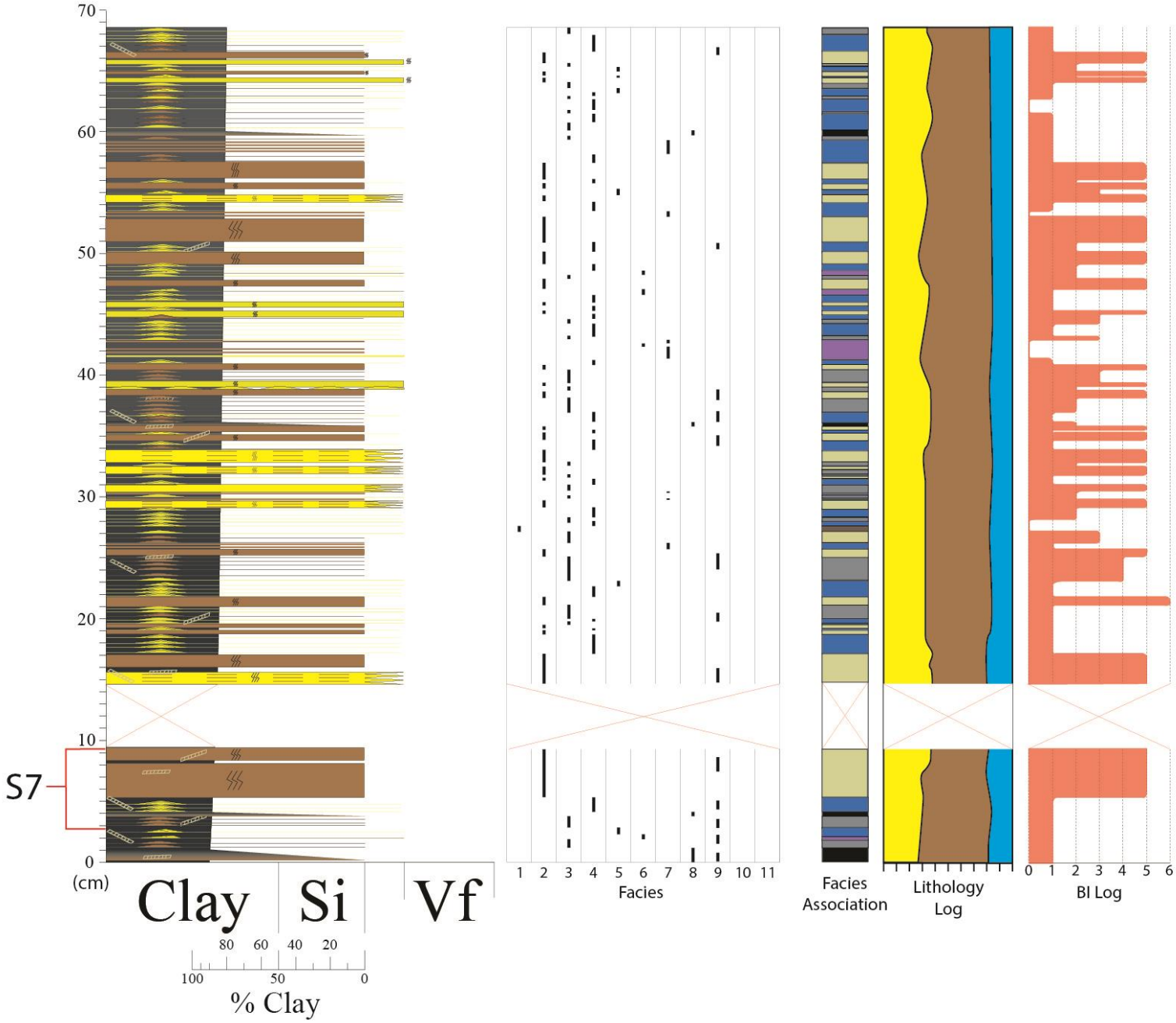

Fig. 41. Stratigraphic column, facies chart, facies association column, lithology graphic log, and BI log for parasequence 54. Sample 7 used for micro-scale analysis is highlighted by red bracket on the left. Parasequence 54 is from 7208.95'-7206.10'.

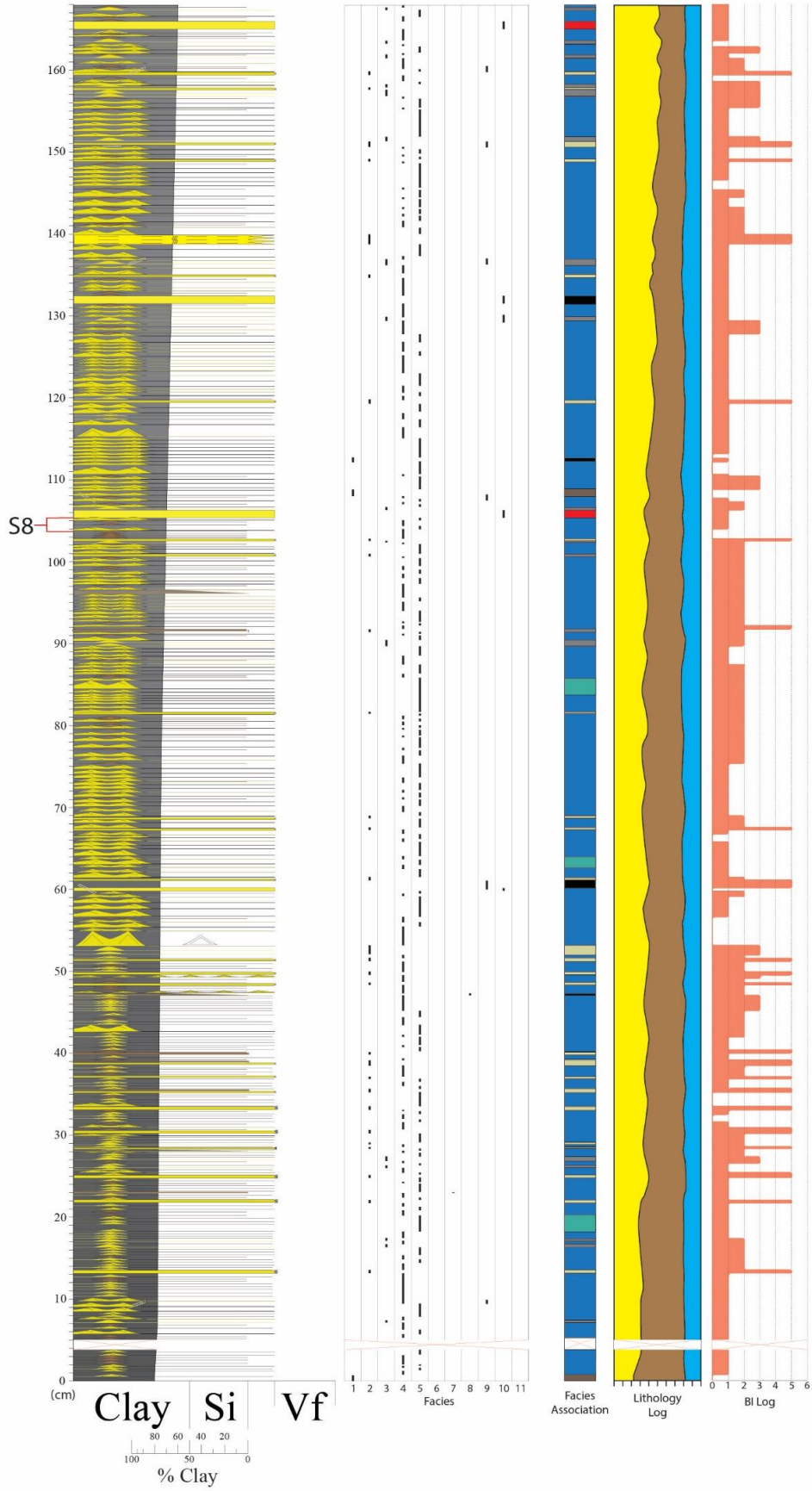

Fig. 42. Stratigraphic column, facies chart, facies association column, lithology graphic log, and BI log for parasequence 80. Sample 8 used for micro-scale analysis is highlighted by red bracket on the left. Parasequence 80 is from 7136.90'-7130.10'.

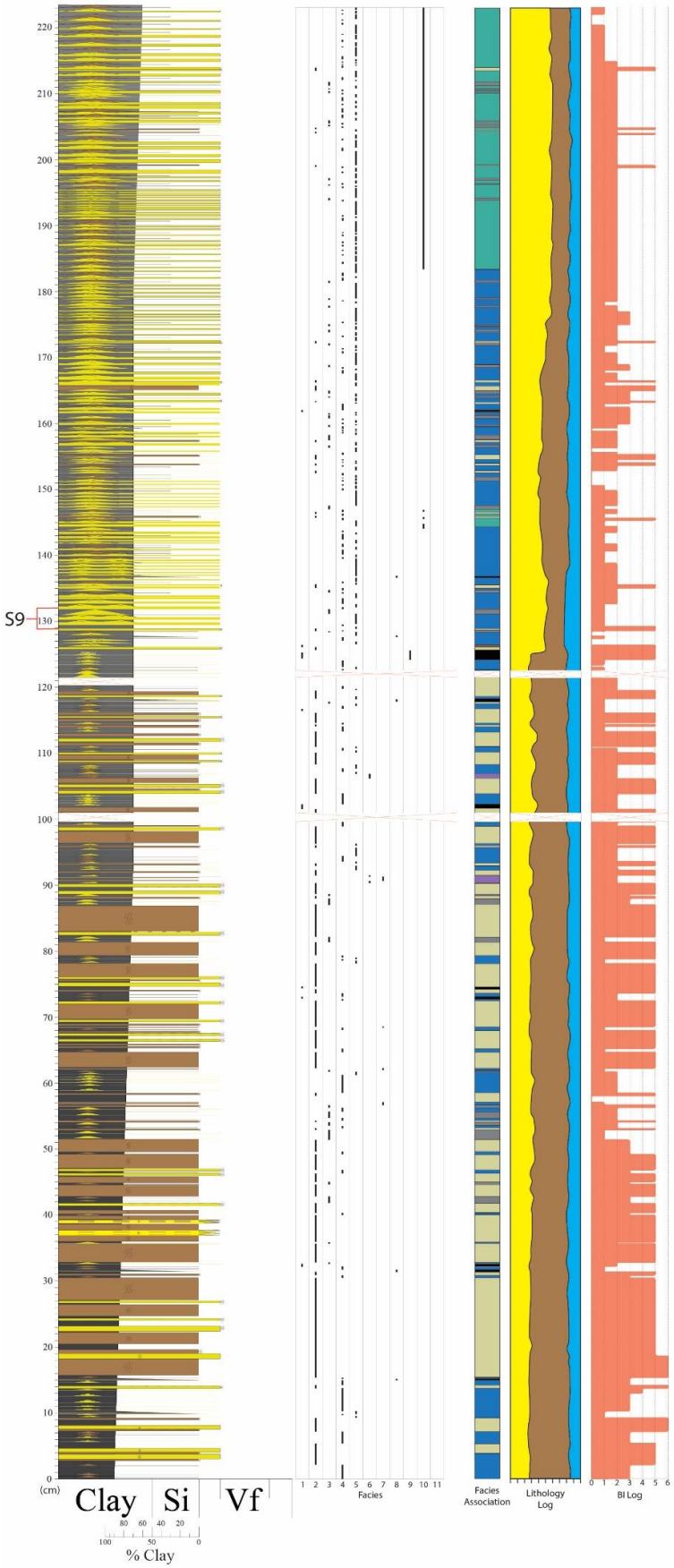

Fig. 43. Stratigraphic column, facies chart, facies association column, lithology graphic log, and BI log for parasequence 88. Sample 9 used for micro-scale analysis is highlighted by red bracket on the left. Parasequence 88 is from 7100.50'-7090.90'.

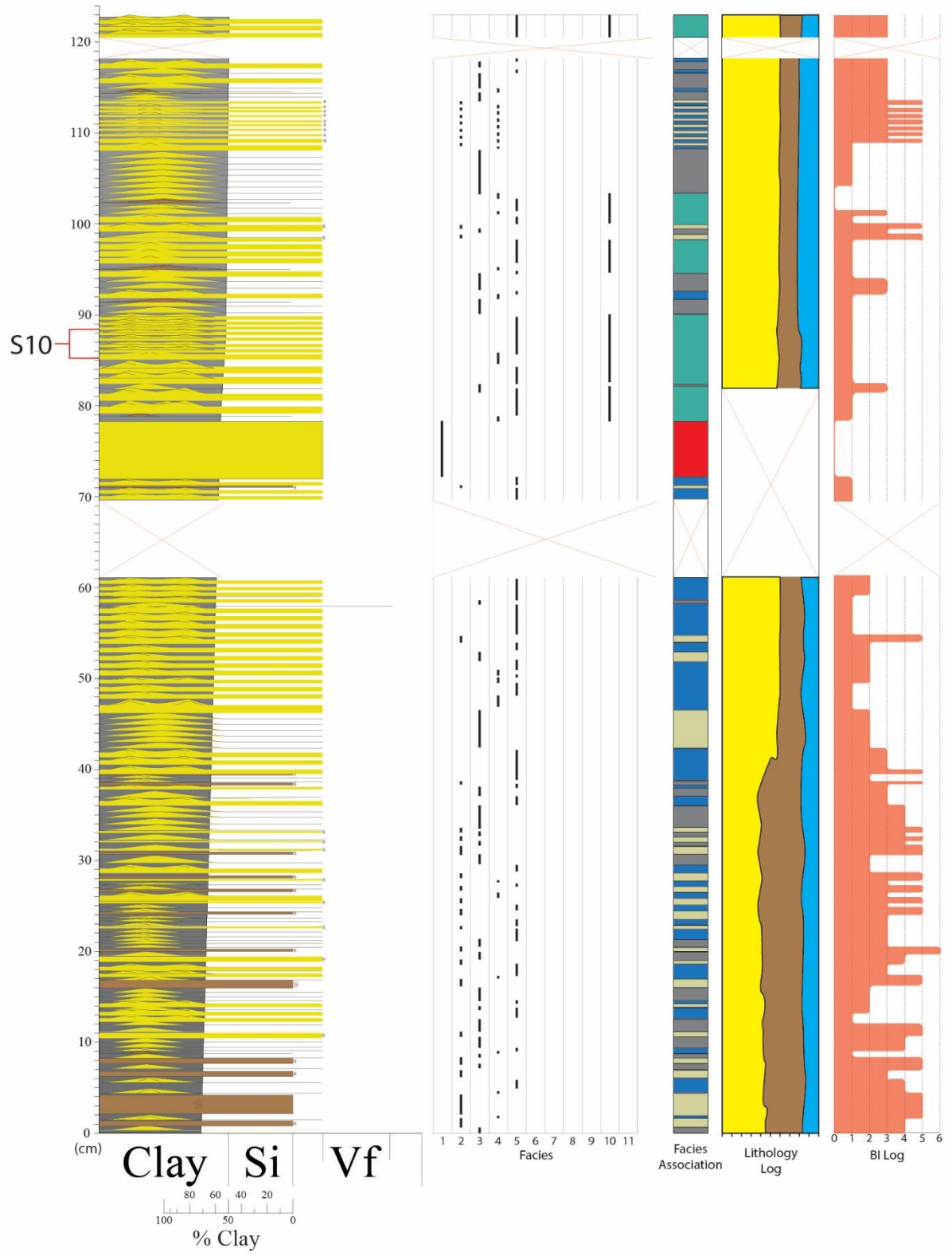

Fig. 44. Stratigraphic column, facies chart, facies association column, lithology graphic log, and BI log for parasequence 89. Sample 10 used for micro-scale analysis is highlighted by red bracket on the left. Parasequence 89 is from 7090.90'-7084.40'.

5.3 Micro-scale Analysis

Micro-scale analysis was performed in order to determine the mineralogy and microfossils present within each sample from the ten parasequences. By observing the photomicrographs of thin-sections, composition and abundance was determined between siliciclastic or calcareous, and further organized into detrital or diagenetic. This was accomplished by extrapolating the identified minerals provided by Weatherford Laboratories to the entire photomicrograph. From this, level of clastic dilution (sedimentation rate) and distance from shoreline was interpreted. In this analysis, the siliciclastic components were typically detrital, including quartz, silt, and clays. They are interpreted to be of terrigenous origin and their abundance is correlated with clastic dilution and proximity to the shoreline. Furthermore, detrital siliciclastics were further divided into framework (i.e., quartz) and matrix grains (i.e., clays). High abundance of framework grains indicate high clastic dilution, whereas low abundance indicate low clastic dilution (Bohacs et al., 2011; Hart; 2016; Li and Schieber, 2018). Although seldom seen, diagenetic siliciclastics were also present in these deposits and include illitic, kaolinitic, and chloritic clays that commonly fill pore spaces or infill foraminiferal tests. However because the aluminum needed to form these phyllosilicates must be of terrigenous source, these authigenic clays are good indicators of detrital sources (Hart, 2016). Calcareous components were also divided into detrital or diagenetic categories, including detrital biogenic calcareous particles and diagenetic calcareous cement. Detrital calcareous biogenic particles include microfossil such as foraminiferal tests, coccolithis, and calcispheres; which are deposited by suspension onto the sea bed, and could be reworked by subsequent bedload processes. Diagenetic calcareous cements are composed of authigenic calcite that develops by precipitating out of the water, and are typically infilling pore spaces, foraminiferal tests, or replacing grains. Abundance of calcareous material is correlated with distance from shoreline and inversely correlated with clastic dilution (Bohacs et al., 2011; Hart; 2016; Li and Schieber, 2018). Other

diagenetic products, including glauconite and pyrite, were developed after deposition during shallow burial of sediment. Although diagenetic materials are formed post-deposition, they are typically indicators of low clastic dilution, as these processes require dysoxic reducing conditions, which are produced by the consumption of oxidants from organisms digesting organic matter (Potter et al., 2005). Dolomite and quartz overgrowths are also diagenetic products, but are produced by deep burial and were not considered for interpreting environment of deposition. The two main components (i.e., siliciclastic, calcareous) were categorized by assigning a relative abundance from high, medium, low to none; and abundance of framework/matrix was given a percentage. The third component, (i.e., diagenetic) was also categorized by assigning the relative abundance from high, medium, low to none. Observations highlighted in the photomicrographs and SEM images were entirely taken from the Weatherford Laboratories' report, however, interpretations suggested in this study were all independent of their report (See Appendix). The locations of the samples from bottom to top are the following: 7384.25', 7343.20', 7332.65', 7316.40', 7300.20', 7262.80', 7208.85', 7133.35', 7094.55', and 7085.80'. A chart below summarizes the three categories and interpretations (Fig. 45). It is important to note that one sample is not diagnostic of the entire parasequence, however, it is still of value because it provides a sense of the mineralogy present.

5.3.1 Photomicrograph observations and interpretations

The interpretations of all samples were summarized into a chart in figure 46. All samples contain siliciclastic, calcareous and diagenetic components. Two photomicrograph samples are provided below in figure 47, representing sample one, and in figure 48, representing sample two. As seen in figure 47, different grains and minerals are labelled based on what was provided by Weatherford Laboratories. Given their identification of different grains and minerals, relative

abundance of the three components were interpreted. Furthermore, by visual inspection, the framework grain to matrix ratio was interpreted.

Sample one is found within a HST and in the middle of P9. This sample contains medium, low, and low amounts of siliciclastics, calcareous and diagenetic material respectively. The framework to matrix ratio is 1:1 (Fig. 47). Sample two is found within a LST and within the bottom of P13. The sample contains high, medium, and medium amounts of siliciclastics, calcareous and diagenetic material respectively. Ratio between framework grains to matrix is 4:1 (Fig. 48). Sample three is found within a TST and in the middle of P24. This sample contains high amounts of siliciclastics, no calcareous content and low amounts of diagenetic material. The framework to matrix ratio is 1:1. Sample four is found within a TST and bottom of P30. The sample contains low, high, and high amounts of siliciclastics, calcareous and diagenetic material respectively. Ratio between framework grains to matrix is 2:3. Sample five is found within a HST and top of P33. The sample contains high, low, and low amounts of siliciclastics, calcareous and diagenetic material respectively. Ratio between framework grains to matrix is 3:2. Sample six is found within a HST and middle of P43. The sample contains low, high, and high amounts of siliciclastics, calcareous and diagenetic material respectively. Ratio between framework grains to matrix is 3:7. Sample seven is found within a TST and bottom of P54. The sample contains high, medium, and medium amounts of siliciclastics, calcareous and diagenetic material respectively. Ratio between framework grains to matrix is 7:3. Sample eight is found within a HST and middle of P80. The sample contains high, medium, and high amounts of siliciclastics, calcareous and diagenetic material respectively. Ratio between framework grains to matrix is 4:1. Sample nine is found within a LST and middle of P88. The sample contains high, low, and low amounts of siliciclastics, calcareous and diagenetic material respectively. Ratio between framework grains to matrix is 4:1. Sample ten is found within a

LST and top of P89. The sample contains high, high, and high amounts of siliciclastics, calcareous and diagenetic material respectively. Ratio between framework grains to matrix is 4:1.

Interpretation

Micro-scale interpretations were mainly based on the relationships discussed in Hart (2016). Three of the relationships discussed in his study include: 1) sand will only be deposited a certain distance into the basin and as distance increases, siliciclastic deposits will predominantly be muds. 2) Detrital clay mineral content and calcareous content are inversely correlated. More proximal areas will be dominated by detrital components and will decrease as calcite production increases basinward. 3) Proximal environments tend to have a higher sedimentation rates, thus diluting any biogenic particle input. Due to this, such deposits will have less calcareous content and higher siliciclastic content. Therefore, from these three relationships, calcareous content is interpreted to increase further basinward and decrease landward. Utilizing these relationships, interpretations regarding the proximity to the shoreline of the sample were made. Furthermore, mineralogy variability can be related to the variability found within macro-scale analysis and meso-scale analysis; based on the sequence and parasequence stratigraphic position of the sample.

From sample one (S1) to S2 (Fig. 47, 48), the proportions of all three components and the ratio between framework grains to matrix increased. This suggests an increase in clastic dilution and therefore a basinward shift of the shoreline. The increase in clastic dilution and siliciclastic proportions can be related to the change in stratigraphic position from a HST to a LST. Comparing S2 and S3, calcareous material is absent and diagenetic components are low in S4, therefore the shoreline is interpreted to have had shifted basinward; which is also reflected by the change from a lower LST position to a higher position. From S3 to S4, the decrease in the proportion of siliciclastic and increase in calcareous and diagenetic components suggest a landward shift of the

shoreline. This decrease in clastic dilution is seen to be related to the stratigraphic position, as sample four is found stratigraphically higher within the same TST as sample three. From S4 to S5, there is an increase in siliciclastics and decrease in calcareous and diagenetic components. This increase in siliciclastic is interpreted to be the result from the change from a TST to the beginning of a HST. In addition to the change in system tracts, S5 is found within the top of a parasequence compared to sample four which is found near the bottom. Therefore, compared to S4being within the end of a TST and bottom of a parasequence, S5 represents a basinward shift of the shoreline as the sample is from a HST and top of a parasequence. From S5 to S6, there is an increase calcareous and diagenetic components suggesting a landward shift of the shoreline. This correlates with the change in stratigraphic positions as S5 is found within a HST and S6 is found within a TST. Sample six to sample seven increases in siliciclastics and decreases in calcareous and diagenetic components, suggesting a basinward shift of the shoreline. This correlates with the change from a HST to a TST. Sample seven to sample eight increases in the ratio of framework grains, suggesting a basinward shift of the shoreline. This corresponds with the change from TST to a HST. Sample eight to sample nine decreases in calcareous and diagenetic components, suggesting a basinward shift of the shoreline. This corresponds with the change from a HST to a LST. Sample nine to sample ten increases in the ratio of framework grains, suggesting a basinward shift of the shoreline. This corresponds with the change from a lower LST position to a higher LST position.

Components	Interpretation
HS/LC High Framework Low Matrix	High Clastic Dilution Proximal to Shoreline High Sedimentation Rates
HS/LC Low Framework High Matrix	Moderate Clastic Dilution Proximal to Shoreline High Sedimentation Rates
LS/HC Low Framework, High Matrix	Low Clastic Dilution Distal to Shoreline Low Sedimentation Rates
LS/HC High Framework Low Matrix	Modereate Clastic Dilution Distal to Shoreline High Sedimentation Rates
HD	Low Sedimentation Rates
LD	High Sedimentation Rates

Fig. 45. Chart summarizing the three components with each abundance end member categorized in micro-scale analysis. The "H" represents "high abundance" and the "L" represent "low abundance". The "S", "C", and "D" represent "siliciclastic", "calcareous", and "diagenetic" respectively. The interpretation of each component and associated abundance is given on the right.

	P9/S1	P21/S2	P24/S3	P30/S4	P33/S5	P43/S6	P54/S7	P80/S8	P88/S9	P89/S10
Position in Parasequence (Bottom/Middle/Top)	Middle	Bottom	Middle	Bottom	Top	Middle	Bottom	Middle	Middle	Top
Proportion of Siliciclastic (High/Medium/Low)	M	H	H	L	H	L	H	H	H	H
Proportion of Calcareous (High/Medium/Low)	L	M	N/A	H	L	H	M	M	L	H
Proportion of Diagentic (High/Medium/Low)	L	M	L	H	L	H	M	H	L	H
Framework to Matrix Ratio	1:1	4:1	1:1	2:3	3:2	3:7	7:3	4:1	4:1	19:1
Shoreline Migration (Basinward/Landward)	N/A	Basinward	Basinward	Landward	Basinward	Landward	Basinward	Basinward	Basinward	Basinward
System Tract	HST	LST	LST	TST	HST	TST	TST	HST	LST	LST

Fig. 46. Chart summarizing the relative proportions of siliciclastic, calcareous, and diagenetic components in the samples examined in each parasequence. The relative position of the sampling within each parasequence is also noted. An interpretation of the shoreline migration relative to the first sample is given in the bottom row.

Sample 1 from Parasequence 9: 7384.25ft

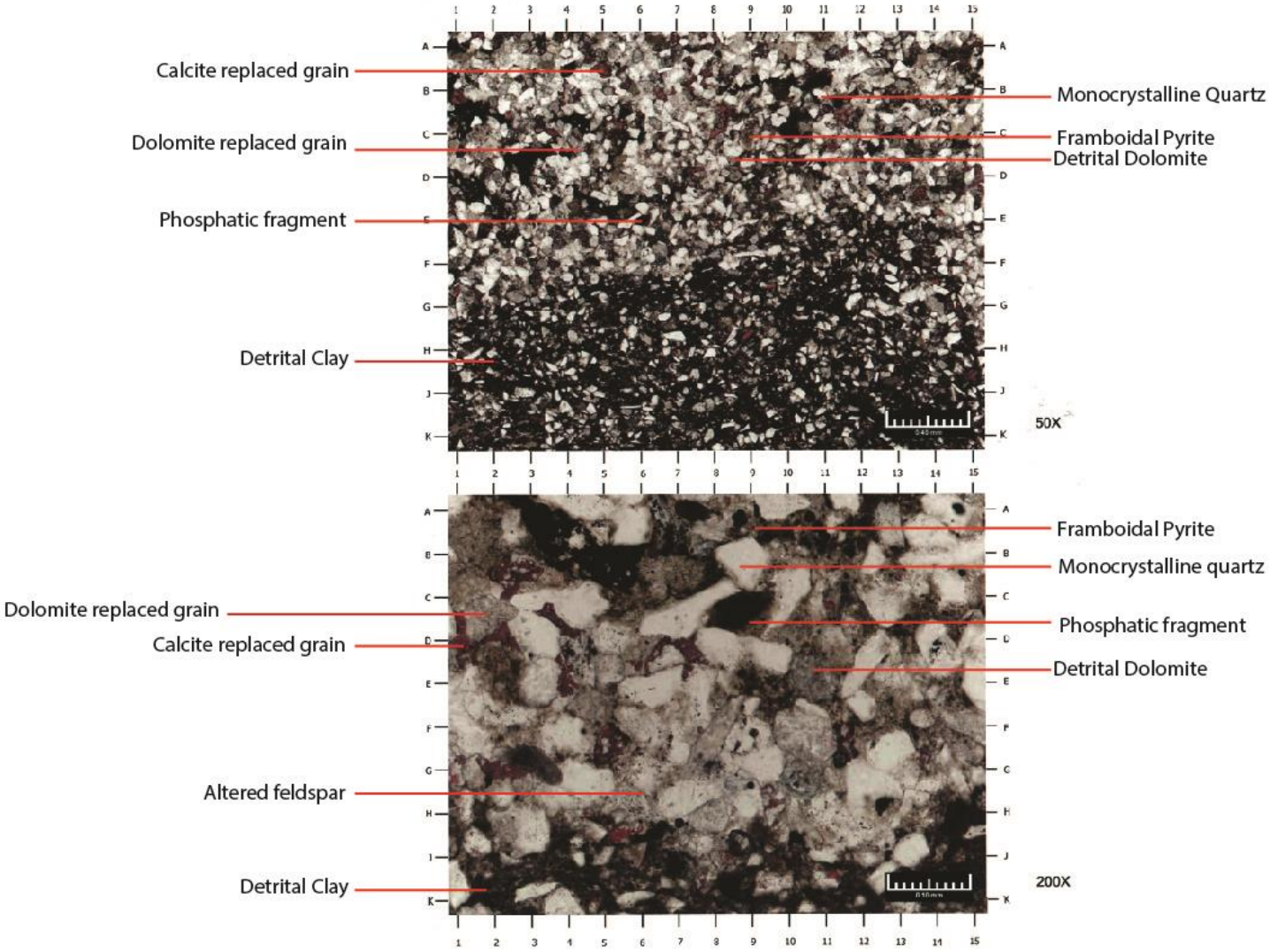

Fig. 47. Sample 1. Plain light photomicrographs of a thin section in parasequence 9. A general view is at the top and detailed view is at the bottom.

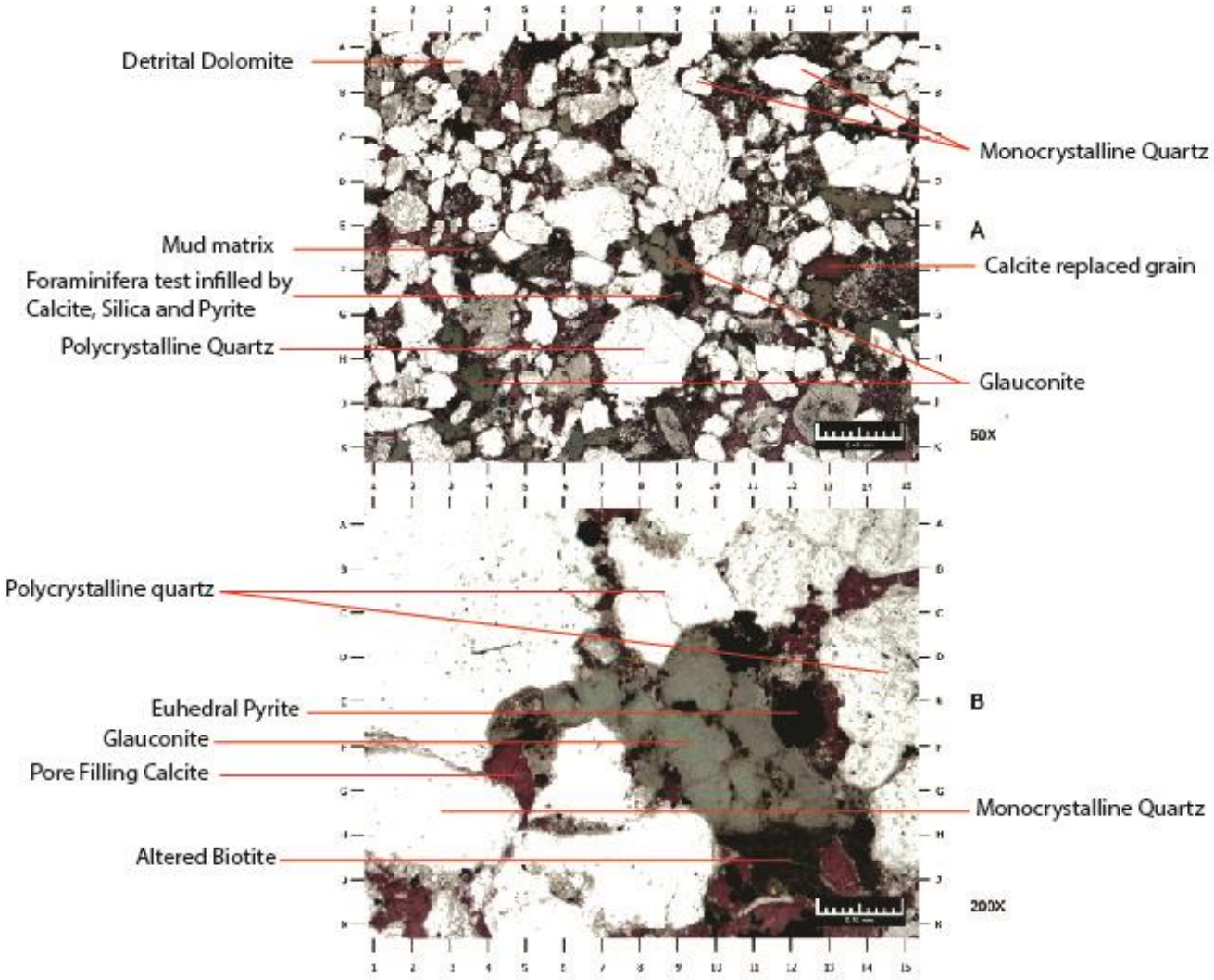

Fig. 48. Sample 2. Plain light photomicrographs of a thin section in parasequence 21. A general view is at the top and detailed view is at the bottom.

6. Discussion

6.1 Identifying Vertical Variability from Integration of all Three Scales of Analysis

Vertical variability can be predicted as all three scales are interdependent. From the broadest scale, macro-scale analysis reveals the lithological variability between parasequences depending on their sequence stratigraphic position. To further examine individual parasequences, meso-scale analysis identifies the vertical change in facies and depositional processes which are dependent on the natural shoaling upward succession of parasequences, as well as its relative sequence stratigraphic position as examined in macro-scale analysis. Micro-scale analysis further investigates the mineralogy of a specific position within a parasequence, and is dependent on the relative position within a parasequence and sequence stratigraphic position. With the relationships observed in this study, predictions can be formed in terms of distribution of facies, dominant depositional process, and mineralogy within analogous deposits in the San Juan Basin.

6.1.1 Vertical Variability Indication from Well Log

The gamma and resistivity logs are good indicators of lithology. High gamma typically indicate clay rich deposits, and low gamma indicate sand rich deposits. In this study, the core and well log were tied together to investigate the application of the well log in a comprehensive thin-bedded facies analysis study. The well log has an approximate resolution of one meter (Fig. 5). Parasequence thicknesses in this study range from 60cm-220cm (Fig. 6). This resolution inhibits the use of the well log to identify individual laminations and thin parasequences (<1m), but was used to resolve parasequence sets and sequences (Fig. 5). The well log provided a broad indication of vertical variability, and was useful in identifying sharp surfaces and changes throughout the core.

However, for thin-bedded units such as the core in this study, detailed thin-bedded facies analysis was important to ensure that no features were missed due to the low resolution of the well log.

6.2 Comparison to other thin-bedded facies study

Facies examined in this study were comparable to the ones presented in Li and Schieber (2018) of the Cretaceous Tununk Shale, Utah. In their study, they analysed polished slab rock samples collected from the field, photomicrographs and SEM images. The lithofacies, sedimentary structures, trace fossil types and thicknesses of laminations they observed were analogous to the ones examined in this study (Fig. 49). As mentioned above, the lithofacies used in this study were taken from Li and Schieber (2018) with an additional two lithofacies. Sedimentary structures seen in their study include wave ripple laminations, combined-flow ripple laminations, current ripple laminations, parallel to wavy laminations, bioturbated mudstone, and normal grading; all of which were observed in this study. Trace fossils seen in their study include *Chondrites*, *Planolites*, *Phycosiphon*, *Teichichnus*, and; *Zoophycos*; which were present in this study (Fig. 10). Furthermore, they concluded that the Tununk Shale was an offshore mud blanket deposited on a storm-dominated shelf in the CWIS; dynamically shifting in shelf environments that was largely controlled by sea-level changes. Comparing their conclusions with the results from this study, it can be seen that the Upper Mancos is similar to the Tununk Shale. However, the Upper Mancos Shale is interpreted to have had deposited on a storm- and tide- dominated shelf.

Furthermore, this study shows that thin-bedded facies analysis can be done on slabbed core and not restricted to polished slabs, photomicrographs and SEM of rock samples collected in the field as done in Li and Schieber (2018). By doing so, large sections of core can be analysed rather than individual samples, which limits the comprehensive facies analysis. However, an integration of

both methodologies may prove beneficial as samples collected from the field are wider and can give better indication of lateral variability.

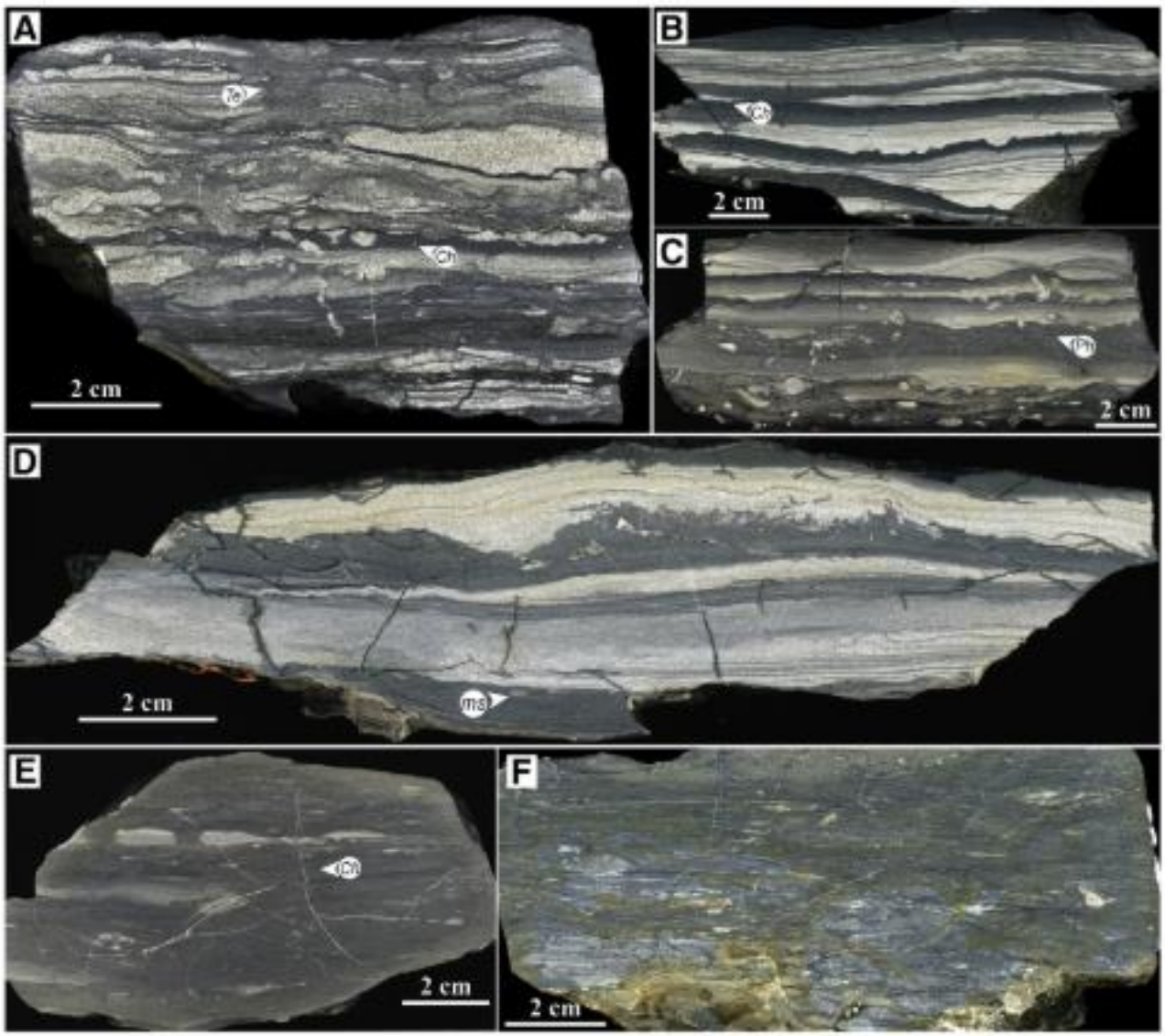

Fig. 49. Example of facies observed in Li and Schieber (2018). The facies observed in their study are analogous to the ones observed in this study (taken from Li and Schieber, 2018).

6.3 Comparison with Existing Depositional models

The depositional models from Hart (2016), and Li and Schieber (2018) can be applied to the results observed in this study. Both models link lithofacies, shelf environment of deposition and depositional processes together. They suggest that the decrease in clastic dilution, and increase in calcareous components is correlated with distance from shoreline. They further link a variety of shelf environments with depositional processes, suggesting that lower shoreface and inner shelf areas are dominated by processes such as waves, combined-flows, currents and HCS. With increasing distance from the shoreline HCS and combined-flows decrease, and currents and suspension settling becomes more prevalent. The results observed in this study correspond with their models.

The shoreline during the deposition of this core was gradually regressing (Fig. 3) and is supported by the sedimentological observations found in this study as the core has an overall coarsening upward succession. By applying the models provided by Hart (2016) and Li and Schieber (2018) the overall coarsening upward of the core should correspond with the decrease in calcareous and biogenic particles. Furthermore, depositional processes should increase in wave, combined-flows, and tides. These patterns were observed in this study and are congruent with the models provided by Hart (2016) and Li and Schieber (2018).

6.4 Contribution to Debatable Topics

This study addresses three main debatable topics. First, it was historically thought that mud-dominated successions were homogeneous and were exclusively deposited by suspension settling. This study disproves that idea and suggests that "monotonous" successions of mud have a wealth of sedimentary structures, deposited by multiple processes. The presence of a variety of sedimentary structures indicate that suspension settling, although present, was just one of the many processes that were responsible for the transport and deposition of muddy sediment. Secondly, the presence of bedload transport refutes the idea of long-term Oceanic Anoxic Events. There was a brief OAE from Coniacian to Santonian, during the Cretaceous (Jenkyns, 1980). As this core was deposited from late Turonian- middle Coniacian, it falls within the earlier age range of the Coniacian-Santonian OAE. Although the OAE is considered as a long-term global phenomenon (Jenkyns, 1980), the presence of bedload transport, as well as evidence of storms; as shown in this study, suggest mixing and introduction of oxygen into the water column. This could suggest that the OAE during the Coniacian-Santonian was not as long-term as previously thought, and perhaps intermittent storms may have introduced oxygen into the water column. Thirdly, the origin of mud clasts and floccules within the CWIS are also a topic of debate. Plint (2014) believe that the origin of clays of mud clasts were intraclasts from storm erosion from the contemporaneous sea bed and did not arrive in discrete flakes or flocculated states. However, Schieber (2015) believe that the mud clasts were not intraclasts, and originated from clay floccules and from a substantial depth instead of near the sea bed. This study agrees with Schieber (2015) due to the evidence observed in the SEM images. Flocculated clays as seen in Schieber et al. (2013) are seen in the SEM images observed in this study (See Appendix).

6.5 Cyclicity

Cyclicity can be identified if the depositional duration for the succession of interest and number of units are known (e.g., Zhu and Bhattacharya, 2012). Given that the core was deposited in a span of approximately 2 myr from early late Turonian to late Coniacian, and the number of sequences, system tracts, and parasequences are roughly 3, 11 and 92 respectively; cyclicity for all three can be calculated (Fig. 3 and 6) (Nummedal and Molenaar, 1995). For each sequence, it took ~670,000 yr to deposit, falling under the fourth-order eustatic cyclicity described in Vail et al. (1977) and Haq et al. (1988). For the system tracts, each one took ~200,000 yr to deposit, falling under fifth-order eustatic cyclicity, and each parasequence took ~20,000 yr to deposit, associated with the sisxth-order eustatic cyclicity (Vail, 1977; Haq et al., 1988; Mitchum and Van Wagoner, 1990). These cycles can be attributed to eustatic and climatic variations influenced by orbital forcing Milankovitch effects (Fischer, 1964; Hays, 1976; Mitchum and Van Wagoner, 1991). Milankovitch effects are generated by Earth's orbital irregularities such as eccentricity, obliquity and precession (Fischer, 1964; Hays, 1976; Mitchum and Van Wagoner, 1991). Eccentricity is the shape of the Earth's orbit and has two cycles, 100,000 yr and 413,000 yr. The obliquity of the Earth is related to its rotational axis, which changes up to 3° in an obliquity cycle of 41,000 yr. Lastly, the Earth precesses on its rotational axis, and the precession cycle is around 26,000yr (Fischer, 1964). As discussed in Mitchum and Van Wagoner (1991), the Milankovitch cycles of eccentricity, obliquity and precession may have effects on the fifth-, and sixth-order eustatic cyclicity. As the deposition duration of each sequence is ~670,000 yr, each system tract is ~200,000 yr, and each parasequence is ~20,000 yr, it can be inferred that the eustatic cyclicity is influenced by the Milankovitch cycle, wherein the eccentricity cycle influenced the deposition of each sequence, the obliquity cycle influenced the deposition of each system tract, and the precession cycle influenced

the deposition of each parasequence. Therefore, the deposition of this core may have been influenced by Milankovitch effects and represent Milankovitch cycles.

Currently, there is a debate regarding the origin of Cretaceous cyclothems such as the Upper Mancos Shale (Gale et al., 2002, 2008). There are two groups of thought; one group suggest that 4th-order sequence bounding unconformities are tectonic in origin (e.g., Yoshida et al., 1996, Vakarelov et al., 2006), and another group believe sequence bounding unconformities are driven by glacio-eustasy (e.g., Miller et al.. 2003, Laurin and Sagemen, 2007; Locklair and Sagemen, 2008; Zhu et al., 2012). In this study, it is believed that the cyclothems observed in the Upper Mancos Shale was of glacio-eustatic origin, influenced by Milankovitch Cycles. This is because high-frequency sea level changes must be accounted for, during the deposition of parasequences (~20, 000 yr); and other controlling mechanisms (e.g., tectonics) cannot explain the quick changes in sea level (<1 my). This reasoning was also proposed by Miller et al. (2003), that Milankovitch Cycles controlled moderate-sized ice sheets in Antarctica, which ultimately contributed to high-frequency sea level changes.

6.6 Industry Implications

It is of interest to the petroleum industry to understand the organic content and kerogen type present within sedimentary deposits as those two properties control the presence and type of petroleum within. The presence and type of organic matter (OM) in sediment are largely controlled by three factors: 1) organic supply from a terrigenous source or biogenic production; 2) destruction of OM by oxidation, bacterial degradation or ingestation by benthic organisms; 3) dilution of organic matter by other sediment (Arthur and Sageman, 2005, Bohacs et al., 2005; Tyson, 2005; Hart, 2016). Typically, the organic matter can be characterized by measurements of total organic carbon (TOC) and hydrogen index (HI) from Rock-Eval pyrolysis (Ronov, 1958). The total organic

carbon (TOC) is expressed in weight percent (wt. %), or number of grams of TOC in 100g of sediment. The hydrogen index is expressed in milligrams of hydrocarbon per gram of organic carbon (mg HC/g TOC) (Langford and Blanc-Valleron, 1990). TOC levels can be used to interpret source richness suggested by a semiquantitative scale; in which a poor, fair, good, and very good source richness corresponds with 0.0-0.5%, 0.5-1.0%, 1.0-2.0%, and >2.0% TOC respectively (Peters, 1986).

TOC values for specific intervals of the core was provided by Weatherford Laboratories. The intervals that they examined were the following: 7413.8ft, 7409ft, 7379.3ft, 7326.4ft, 7311.8ft, 7269ft, 7258.5ft, 7234.4ft, 7223.8ft, 7214.9ft, 7191.3ft, 7160.4ft, 7157.5ft, 7144.7ft, 7119.8ft, 7097ft, and 7076.7ft. The TOC values in the same order as sample depth are: 1.47, 1.23, 1.26, 1.09, 0.88, 2.17, 3.08, 2.19, 2.31, 2.07, 1.88, 1.53, 1.50, 1.92, 1.44, 1.26, and 1.50. A line graph is provided in figure 50 representing the change in TOC from the bottom to the top of the core. At the interval 7413.8ft, the TOC value is a 1.47 representing a good source richness, and begins to decline until 7269ft, where TOC values sharply increase. The greatest TOC value is 3.08, representing a very good source richness at 7258.5ft, before the TOC value gradually decreases, correlated with the decrease in depth. The end of the core records a 1.50 TOC value, representing a good source richness (Fig. 50). The average TOC value is 1.69, which represents a good source richness. Referring to figure 4 and figure 6, it can be seen that the TOC value is greatest within the second TST, and lowest within the first TST. As for lithofacies, TOC value is greatest within a SCM, and lowest within a CSSM. TOC values are observed to be greater within the more mud-dominated sections (e.g., 7258.5ft) and decline as sand increases up section.

Regarding a broader, regional scale, Broadhead (2015) provided TOC values for all three Upper Mancos units, and is of interest to this study to discuss the TOC values for the Mancos C and

B. TOC values for Mancos C ranges from 0.5%-3.2%. A large majority of the samples analysed (81%) have more than 1% TOC, and a little less than half (44%) have more than 2% TOC, making Mancos C a good to very good source rock. Rock-Eval reveal that the kerogen type for Mancos C are dominantly Type IIS oil-prone, suggesting that Mancos C was deposited in a marine setting; corresponding to the sedimentological evidence shown in this study. Furthermore, TOC generally increases to the northeast (basinward). TOC values for Mancos B are mostly more than 1% and a third of the samples examined have more than 2% TOC; which also makes Mancos B a good to very good source rock. Mancos B has a mixture of oil-prone, gas-prone and inertinitic kerogens, however, unlike Mancos C, Mancos B contain a low percentage of Type II and Type IIS kerogens. It appears that TOC levels are higher within the lower parts of Mancos B compared to the upper parts.

In addition to TOC, net-to-gross is important as it indicates the total volume in a given reservoir. In this study, the net-to-gross is 0.22, suggesting that 22% of the core is sand and can store hydrocarbons that can flow. As suggested in this study, most sandy units are associated with wave rippled, combined-flow rippled units that suggest energetic tempestite and tidal processes; that occur within relatively shallower depths.

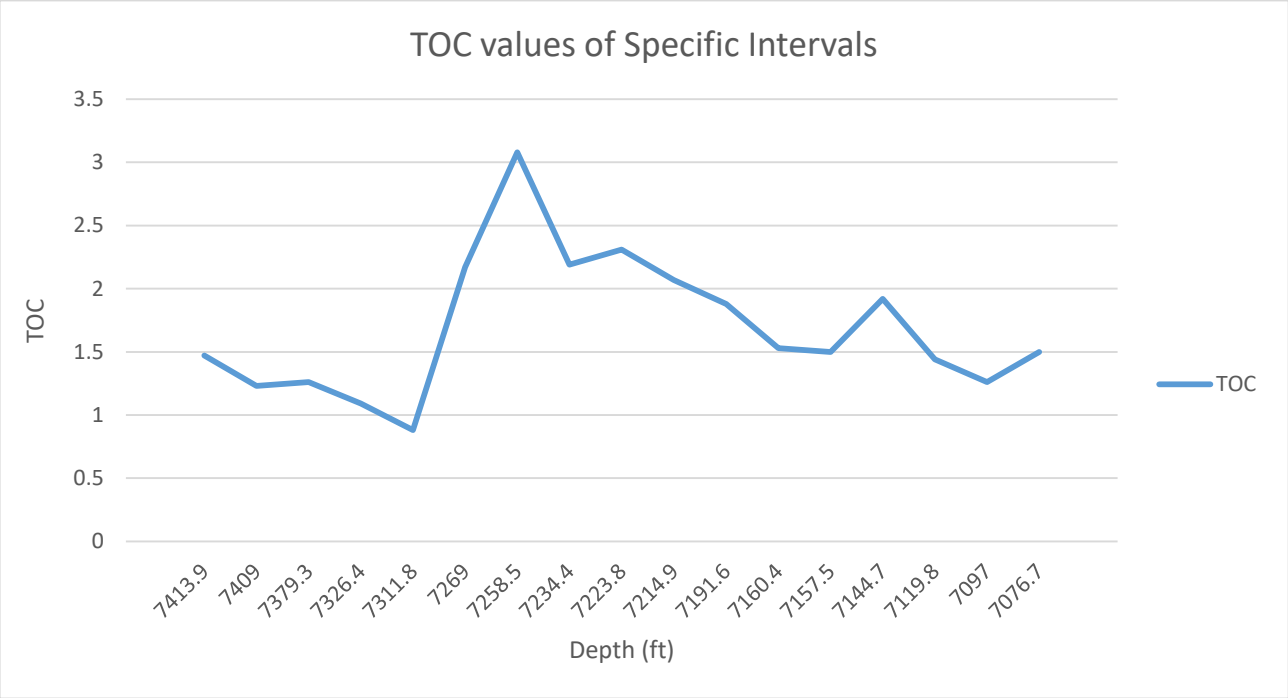

Fig. 50. Graphical representation of TOC values throughout the core. The y-axis is the TOC value and x-axis is depth. TOC values sharply increase at 7269ft and gradually decreases correlated to decrease in depth. All data is provided by Weatherford Laboratories.

7. Conclusion

Thin-bedded facies analysis of the Upper Mancos Shale has revealed vertical variability in lithology, sedimentary structures, depositional processes and bioturbation intensity. Furthermore, candidate surfaces with sequence stratigraphic importance were picked out by observing sharp lithological, bioturbation intensity, and lamination/bed thickness changes throughout the core. The well log associated with the core was analysed and used for further confidence in picking the candidate surfaces. The ten parasequences that were analysed were examined for changes in depositional process and were categorized in terms of their associated dominant, influenced and affected depositional process. It was observed that when stratigraphically higher in the core, wave-dominated depositional processes such as tempestites and ignitive turbidites increased; whereas biogenic reworking and suspension settling processes decreased. This vertical change in the distribution of depositional process is related to the overall marine regression (Fig. 3). Furthermore, changes in depositional processes were also seen within individual upward-coarsening parasequences where tempestites and tidal processes become increasing dominant within the upper portions of a parasequence. Analysis of photomicrographs from Weatherford Laboratories revealed variability in mineralogy depending on the stratigraphic position of the sample. Calcareous and diagenetic components are seen to be more prevalent within bottom half of parasequences, and within TSTs and bottom half of HSTs. Furthermore, framework to matrix ratio is observed to be higher within the top half of the parasequences, and within LSTs and top half of HSTs.

The depositional models developed by Hart (2016) and Li and Schieber (2018) were used in this study and suggest that the deposits examined fall between zone 1 and 2 of Hart's depositional model, and the change in EOD as suggested by the lithofacies from Li and Schieber's depositional model. As for industry implications, TOC values provided by Broadhead (2015) suggest that the

Mancos C and B are good to very good source rocks. The net-to-gross of the core is 0.22, indicating that the reservoir volume within is approximately 22%. Cyclicity was observed in the core and is interpreted to be the result from Milankovitch effects. Candidate sequences, system tracts and parasequences took ~670,000 yr, ~200,000 yr and ~20,000 yr to deposit respectively, associated with Milankovitch cyclicity.

In conclusion, thin-bedded facies analysis can be done on slabbed core, identifying vertical variability in lithology, sedimentary structures, bioturbation and depositional processes. Candidate surfaces can also be interpreted; however in order to complete a true sequence stratigraphic study, correlations must be made; which this study did not focus on. Ultimately, understanding the vertical variability of mud dominated deposits give us a better understanding of ancient mud-dominated depositional systems and the processes that were active during that time. It is shown in this study that previously regarded "monotonous successions" have a wealth of sedimentary structures and were deposited by various depositional processes. Bedload transport is shown to be present. This also have direct implications in understanding source-rock reservoirs, which can be used to predict hydrocarbon type, porosity, permeability and fracturing properties.

References

Aigner, T. (1982). Calcareous tempestites: storm-dominated stratification in Upper Muschelkalk limestones (Middle Trias, SW-Germany). In *Cyclic and event stratification* (pp. 180-198). Springer, Berlin, Heidelberg.

Ainsworth, R. B., Vakarelov, B. K., & Nanson, R. A. (2011). Dynamic spatial and temporal prediction of changes in depositional processes on clastic shorelines: Toward improved subsurface uncertainty reduction and management. *AAPG Bulletin*, *95*(2), 267–297.

Alves, T. M. (2010). 3D Seismic examples of differential compaction in mass-transport deposits and their effect on post-failure strata. *Marine Geology*, *271*(3-4), 212-224.

Arnott, R. W., & Southard, J. B. (1990). Exploratory flow-duct experiments on combined-flow bed configurations, and some implications for interpreting storm-event stratification. *Journal of Sedimentary Research*, *60*(2), 211-219.

Arthur, M. A., & Sageman, B. B. (2005). Sea-level control on source-rock development: perspectives from the Holocene Black Sea, the mid-Cretaceous Western Interior Basin of North Am

Baas, J. H., Best, J. L., & Peakall, J. (2016). Predicting bedforms and primary current stratification in cohesive mixtures of mud and sand. *Journal of the Geological Society*, *173*(1), 12-45.

Baldwin, B. (1971). Ways of deciphering compacted sediments. *Journal of Sedimentary Research*, *41*(1), 293-301.

Barron, E. J., Thompson, S. L., & Schneider, S. H. (1981). An ice-free Cretaceous? Results from climate model simulations. *Science*, *212*(4494), 501-508.

Bilodeau, W. L. (1986). The Mesozoic Mogollon Highlands, Arizona: An Early Cretaceous rift shoulder. *The Journal of Geology*, *94*(5), 724-735.

Bhattacharya, J. P., & MacEachern, J. A. (2009). Hyperpycnal Rivers and Prodeltaic Shelves in the Cretaceous Seaway of North America. *Journal of Sedimentary Research*, *79*(4), 184–209.

Bohacs, K. M., Grabowski Jr, G. J., Carroll, A. R., Mankiewicz, P. J., Miskell-Gerhardt, K. J., Schwalbach, J. R., ... & Simo, J. T. (2005). Production, destruction, and dilution—the many paths to source-rock development.

Bouma, A. H., Kuenen, P. H., & Shepard, F. P. (1962). Sedimentology of some flysch deposits: a graphic approach to facies interpretation. *Amsterdam Elsevier*, *168*.

Birgenheier, L. P., Horton, B., McCauley, A. D., Johnson, C. L., & Kennedy, A. (2017). A depositional model for offshore deposits of the lower Blue Gate Member, Mancos Shale, Uinta Basin, Utah, USA. *Sedimentology*, *64*(5), 1402-1438.

Brett, C. E., & Allison, P. A. (1998). Paleontological approaches to the environmental interpretation of marine mudrocks.

Broadhead, R. F. (2015). The Upper Mancos Shale in the San Juan Basin: Three plays, Conventional and Unconventional.

Brown, W. G. (1988). Deformational style of Laramide uplifts in the Wyoming foreland. *Interaction of the Rocky Mountain foreland and the Cordilleran thrust belt: Geological Society of America Memoir*, *171*, 1-25.

Campbell, C. V. (1966). Truncated wave-ripple laminae. *Journal of Sedimentary Research*, *36*(3), 825-828.

Campbell, C. V. (1967). Lamina, laminaset, bed and bedset. *Sedimentology*, *8*(1), 7-26.

Cheel, R. J., & Leckie, D. A. (1993). 7 Hummocky cross-stratification. *Sedimentology Review 1*, *31*, 103.

Dalrymple, R. W., 2010, Tidal Depositional Systems, in N. P. James, and R. W. Dalrymple, eds., Facies Models 4: St. John's, Geological Association of Canada, p. 201–231Dane, C. H. (1960). *The Boundary Between Rocks of Carlile and Niobrara Age in San Juan Basin New Mexico and Colorado*. US Government Printing Office.

DeCelles, P. G. (2004). Late Jurassic to Eocene evolution of the Cordilleran thrust belt and foreland basin system, western USA. *American Journal of Science*, *304*(2), 105-168.

Dembicki Jr, H. (2009). Three common source rock evaluation errors made by geologists during prospect or play appraisals. *AAPG bulletin*, *93*(3), 341-356.

Dickinson, W. R., Klute, M. A., Hayes, M. J., Janecke, S. U., Lundin, E. R., McKITTRICK, M. A., & Olivares, M. D. (1988). Paleogeographic and paleotectonic setting of Laramide sedimentary basins in the central Rocky Mountain region. *Geological Society of America Bulletin*, *100*(7), 1023-1039.

Dott, R. H., & Bourgeois, J. (1982). Hummocky stratification: significance of its variable bedding sequences. *Geological Society of America Bulletin*, *93*(8), 663-680.

Dumas, S., & Arnott, R. W. C. (2006). Origin of hummocky and swaley cross-stratification—The controlling influence of unidirectional current strength and aggradation rate. *Geology*, *34*(12), 1073-1076.

Dumas, S., Arnott, R. W. C., & Southard, J. B. (2005). Experiments on oscillatory-flow and combined-flow bed forms: implications for interpreting parts of the shallow-marine sedimentary record. *Journal of Sedimentary research*, *75*(3), 501-513.

Einsele, G., & Seilacher, A. (1982). Paleogeographic significance of tempestites and periodites. In *Cyclic and Event Stratification* (pp. 531-536). Springer, Berlin, Heidelberg.

Elder, W. P. (1988). Geometry of Upper Cretaceous bentonite beds: implications about volcanic source areas and paleowind patterns, Western Interior, United States. *Geology*, *16*(9), 835-838.

Ericksen, M. C., & Slingerland, R. (1990). Numerical simulations of tidal and wind-driven circulation in the Cretaceous Interior Seaway of North America. *Geological Society of America Bulletin*, *102*(11), 1499-1516.

Fassett, J. E., Hamilton Jr, W., Martin, G. W., & Middleman, A. A. (1983). Oil and Gas Fields of the Four Corners Area, Contents and Front Matter

Fischer, A. G. (1986). Climatic rhythms recorded in strata. *Annual Review of Earth and Planetary Sciences*, *14*(1), 351-376.

Gale, A.S., Hardenbol, J., Hathaway, B., Kennedy, W.J., Young, J.R., and Phansalkar, V., 2002, Global correlation of Cenomanian (Upper Cretaceous) sequences: Evidence for Milankovitch control on sea level: Geology, v. 30, p. 291–294.

Gale, A. S., Voigt, S., Sageman, B. B., & Kennedy, W. J. (2008). Eustatic sea-level record for the Cenomanian (Late Cretaceous)—extension to the Western Interior Basin, USA. *Geology*, *36*(11), 859-862.

Haq, B. U., Hardenbol, J. A. N., & Vail, P. R. (1987). Chronology of fluctuating sea levels since the Triassic. *Science*, *235*(4793), 1156-1167.

Haq, B. U., Hardenbol, J., & Vail, P. R. (1988). Mesozoic and Cenozoic chronostratigraphy and cycles of sea-level change.

Hart, B. S. (2016). Marine mudstone source rocks in epicontinental basins: Development of a conceptual facies model and application to Cenomanian/Turonian mudstones of the Cretaceous Western Interior Seaway. M. P. Dolan, D. K. Higley, and P. G. Lillis, eds., *Hydrocarbon Source Rocks in Unconventional Plays, Rocky Mountain Region*: p. 364–421.

Hart, B. S., Macquaker, J. H., & Taylor, K. G. (2013). Mudstone ("shale") depositional and diagenetic processes: Implications for seismic analyses of source-rock reservoirs. *Interpretation*, *1*(1), B7-B26.

Harms, J. C. (1969). Hydraulic significance of some sand ripples. *Geological Society of America Bulletin*, *80*(3), 363-396.

Harms, J. C. (1979). Primary sedimentary structures. *Annual Review of Earth and Planetary Sciences*, *7*(1), 227-248.

Hays, J. D., Imbrie, J., & Shackleton, N. J. (1976, December). Variations in the Earth's orbit: pacemaker of the ice ages. Washington, DC: American Association for the Advancement of Science.

Howard, J.D. (1975). The sedimentological significance of trace fossils, in Frey, R.W., ed., The Study of Trace Fossils: A Synthesis of Principles, Problems and Procedures in Ichnology: *New York, Springer-Verlag*, 131–146.

Ichaso, A. A., & Dalrymple, R. W. (2009). Tide-and wave-generated fluid mud deposits in the Tilje Formation (Jurassic), offshore Norway. *Geology*, *37*(6), 539-542.

Jenkyns, H. C. (1980). Cretaceous anoxic events: from continents to oceans. *Journal of the Geological Society*, *137*(2), 171-188.

Jopling, A. V., & Walker, R. G. (1968). Morphology and origin of ripple-drift cross-lamination, with examples from the Pleistocene of Massachusetts. *Journal of Sedimentary Research*, *38*(4), 971-984.

Kauffman, E. G., & Caldwell, W. G. E. (1993). The Western Interior Basin in space and time. *Evolution of the Western Interior Basin: Geological Association of Canada, Special Paper*, *39*, 1-30.

Kiel, S., Amano, K., Hikida, Y., & Jenkins, R. G. (2009). Wood-fall associations from Late Cretaceous deep-water sediments of Hokkaido, Japan. *Lethaia*, *42*(1), 74-82.

Kimura, G., Koga, K., & Fujioka, K. (1989). Deformed soft sediments at the junction between the Mariana and Yap Trenches. *Journal of structural geology*, *11*(4), 463-472.

Kirby, R., & Parker, W. R. (1983). Distribution and behavior of fine sediment in the Severn Estuary and Inner Bristol Channel, UK. *Canadian Journal of Fisheries and Aquatic Sciences*, *40*(S1), s83-s95.

Kirkland, J. I. (1991). Lithostratigraphic and biostratigraphic framework for the Mancos Shale (Late Cenomanian to Middle Turonian) at. *Stratigraphy, Depositional Environments, and Sedimentary Tectonics of the Western Margin, Cretaceous Western Interior Seaway*, *260*, 85.

Kneller, B. C., & Branney, M. J. (1995). Sustained High-Density Turbidity Currents and the Deposition of Thick Massive Sands. *Sedimentology, 42*, 607-616.

Langford, F. F., & Blanc-Valleron, M. M. (1990). Interpreting Rock-Eval pyrolysis data using graphs of pyrolizable hydrocarbons vs. total organic carbon (1). *AAPG Bulletin*, *74*(6), 799-804.

Laurin, J., And Sageman, B.B., 2007, Cenomanian–Turonian Coastal Record in SW Utah, U.S.A.: Orbital-Scale Transgressive–Regressive Events During Oceanic Anoxic Event II, Journal of Sedimentary Research, v. 77, p. 731–756

Lazar, R. O., Bohacs, K. M., Macquaker, J. H. S., Schieber, J., & Demko, T. M. (2015) Capturing Key Attributes of Fine-Grained Sedimentary Rocks in Outcrops, Cores, and Thin Sections: Nomenclature and Description Guidelines. *Journal of Sedimentary Research, 85*, 230-246.

Leckie, D. (1988). Wave-formed, coarse-grained ripples and their relationship to hummocky cross-stratification. *Journal of Sedimentary Research*, *58*(4).

Li, Z., Bhattacharya, J., & Schieber, J. (2015). Evaluating along-strike variation using thin-bedded facies analysis, Upper Cretaceous Ferron Notom Delta, Utah. *Sedimentology*, *62*(7), 2060-2089.

Li, Z., & Schieber, J. (2018). Detailed facies analysis of the Upper Cretaceous Tununk Shale Member, Henry Mountains Region, Utah: Implications for mudstone depositional models in epicontinental seas. *Sedimentary Geology, 364*, 141-159.

Livaccari, R. F. (1991). Role of crustal thickening and extensional collapse in the tectonic evolution of the Sevier-Laramide orogeny, western United States. *Geology, 19*(11), 1104-1107.

Lock, B. E., Butler, R. W., & Franklund, R. T. (2009). Tempestite Sedimentation: An example from the Del Rio Formation of West Texas. *Gulf Coast Association of Geological Societies Transactions, 59,* 463-476.

Locklair, R.E., Sageman, B.B., 2008, Cyclostratigraphy of the Upper Cretaceous Niobrara Formation, Western Interior, U.S.A.: A Coniacian–Santonian orbital timescale, Earth and Planetary Science Letters, v. 269, p. 540-553.

Lowe, D. R. (1982). Sediment gravity flows: II Depositional models with special reference to the deposits of high-density turbidity currents. *Journal of Sedimentary Research, 52*(1).

Lundegard, P. D., & Samuels, N. D. (1980). Field classification of fine-grained sedimentary rocks. *Journal of Sedimentary Research, 50*(3).

MacEachern, J. A. Bann, K. L., Bhattacharya, J. P., & Howell, D. C. $J_{R.}$ (2005). Ichnology of deltas: organism responses to the dynamic interplay of rivers, waves, storms, and tides. *SEPM Special Publication. 83,* 49-85.

Maceachern, J. A., Stelck, C. R., & Pemberton, S. G. (1999). Marine and Marginal Marine Mudstone Deposition: Paleoenvironmental Interpretations Based on the Integration of Ichnology, Palynology and Forarniniferal Paleoecology.

Macquaker, J. H. S., & Gawthorpe, R. L. (1993). Mudstone lithofacies in the Kimmeridge Clay Formation, Wessex Basin, southern England; implications for the origin and controls of the distribution of mudstones. *Journal of Sedimentary Research*, *63*(6), 1129-1143.

Macquaker, J. H., Bentley, S. J., & Bohacs, K. M. (2010). Wave-enhanced sediment-gravity flows and mud dispersal across continental shelves: Reappraising sediment transport processes operating in ancient mudstone successions. *Geology*, *38*(10), 947-950.

Mazumder, R., & Arima, M. (2005). Tidal rhythmites and their implications. *Earth-Science Reviews*, *69*(1-2), 79-95.

McPeek, L. A. (1965). Dakota-Niobrara (Cretaceous) Stratigraphy and Regional Relationships, El Vado Area, Rio Arriba County, New Mxico. *The Mountain Geologist*.

Miller, K. G., Sugarman, P. J., Browning, J. V., Kominz, M. A., Hernández, J. C., Olsson, R. K., ... & Van Sickel, W. (2003). Late Cretaceous chronology of large, rapid sea-level changes: Glacioeustasy during the greenhouse world. *Geology*, *31*(7), 585-588.

Mitchum, R. M., & Van Wagoner, J. C. (1991). High-Frequency Sequences and their Stacking Patterns: Sequence-stratigraphic evidence of high frequency eustatic cycles. *Sedimentary geology*, *70*, 131-160.

Molenaar, C. M. (1983). Major depositional cycles and regional correlations of Upper Cretaceous rocks, southern Colorado Plateau and adjacent areas. Rocky Mountain Section (SEPM).

Molenaar, C. M., & Baird, J. K. (1992). *Regional stratigraphic cross sections of Upper Cretaceous rocks across the San Juan Basin, northwestern New Mexico and southwestern Colorado* (No. 92-257).

Molenaar, C. M., & Cobban, W. A. (1991). *Middle Cretaceous stratigraphy on the south and east sides of the Uinta Basin, northeastern Utah and northwestern Colorado* (No. 1787-P).

Mulder, T., Migeon, S., Savoye, B., & Faugères, J. C. (2001). Inversely graded turbidite sequences in the deep Mediterranean: A record of deposits from flood-generated turbidity currents? *Geo-Marine Letters*, *21*(2), 86–93.

Mutti, E. (1977). Distinctive thin-bedded turbidite facies and related depositional environments in the Eocene Hecho Group (South-central Pyrenees, Spain). *Sedimentology*, *24*(1), 107-131.

Myrow, P. M., Fischer, W., & Goodge, J. W. (2002). Wave-modified turbidites: combined-flow shoreline and shelf deposits, Cambrian, Antarctica.*Journal of Sedimentary research*, *72*(5), 641-656.

Nummedal, D., & Molenaar, C. M. (1995). Sequence stratigraphy of ramp-setting strand plain successions: the Gallup Sandstone, New Mexico.

Pasley, M. A., Riley, G. W., & Nummedal, D. (1993). Sequence Stratigraphic Significance of Organic Matter Variations: Example from the Upper Cretaceous Mancos Shale of the San Juan Basin, New Mexico: Chapter 14.

Passey, Q.R., Dahlberg, K.E., Sullivan, K., Yin, H., Brackett, B., Xiao, Y., & Guzman-Garcia, A.G. (2006). Petrophysical Evaluation of Hydrocarbon Pore-Thickness in Thinly Bedded Clastic Reservoirs: The Clastic Thin-bed Problem. *AAPG Archive Series, No. 1*, 1-15.

Penttila, W. C. (1964). Evidence for the pre-Niobrara unconformity in the northwestern part of the San Juan Basin. *The Mountain Geologist*.

Peters, K. E. (1986). Guidelines for evaluating petroleum source rock using programmed pyrolysis. *AAPG bulletin*, *70*(3), 318-329.

Piper, D. W. (1978). Turbidite muds and silts on deepsea fans and abyssal plains. *Sedimentation in submarine canyons, fans, and trenches*.

Piper, D. J., & Normark, W. R. (2009). Processes that initiate turbidity currents and their influence on turbidites: a marine geology perspective. *Journal of Sedimentary Research*, *79*(6), 347-362.

Plint, G. A. (2014). Mud dispersal across a Cretaceous prodelta: storm-generated, wave-enhanced sediment gravity flows inferred from mudstone microtexture and microfacies. *Sedimentology*, *61*(3), 609-647

Plint, G, A., Macquaker, J. H. S., & Varban, B. L. (2012). Bedload Transport of Mud Across a Wide, Storm-Influenced Ramp: Cenomanian-Turonian Kaskapau Formation, Western Canada Foreland Basin. *Journal of Sedimentary Research*, *82*, 801-822.

Posamentier, H. W., & Vail, P. R. (1988). Eustatic controls on clastic deposition II—sequence and systems tract models.

Potter, P. E., Maynard, J. B., & Depetris, P. J. (2005). *Mud and mudstones: Introduction and overview*. Springer Science & Business Media.

Prave, A. R., & Duke, W. L. (1990). Small-scale hummocky cross-stratification in turbidites: a form of antidune stratification?. *Sedimentology*, *37*(3), 531-539.

Reineck, H. E., & Singh, I. B. (1980). Current and wave ripples. In *Depositional Sedimentary Environments* (pp. 22-55). Springer, Berlin, Heidelberg.

Reineck H. E., & Wunderlich, F. (1968). Classification and origin of flaser and lenticular bedding. *Sedimentology*, *11*(1-2), 99-104.

Ridgley, J. L., Condon, S. M., & Hatch, J. R. (2013). *Geology and oil and gas assessment of the mancos-menefee composite total petroleum system: Chapter 4 in total petroleum systems and geologic assessment of undiscovered oil and gas resources in the san juan basin province, exclusive of paleozoic rocks, new mexico and Colorado* (No. 69-F-4). US Geological Survey.

Ronov, A. B. (1958). Organic carbon in sedimentary rocks (in relation to the presence of petroleum). *Geochemistry*, *5*, 497-509.

Sageman, B. B., & Arthur, M. A. (1994). Early Turonian Paleogeographic/Paleobathymetric Map, Western Interior, U.S. *Mesozoic Systems of the Rocky Mountain Region*, 457-469.

Schieber, J. (1999). Distribution and deposition of mudstone facies in the Upper Devonian Sonyea Group of New York. *Journal of Sedimentary Research*, *69*(4), 909-925.

Schieber, J. (2015). Discussion: "Mud dispersal across a Cretaceous prodelta: Storm-generated, wave-enhanced sediment gravity flows inferred from mudstone microtexture and microfacies" by Plint (), Sedimentology 61, 609–647. *Sedimentology*, *62*(1), 389-393.

Schieber, J. (2016). Mud re-distribution in epicontinental basins–Exploring likely processes. *Marine and Petroleum Geology*, *71*, 119-133.

Schieber, J., Southard, J. B., & Thaisen, K. (2007). Accretion of Mudstone Beds from Migrating Floccule Ripples. *American Association for the Advancement of Science, 318*, 1760-1763.

Schieber, J., & Southward, J. B. (2009). Bedload Transport of Mud by Floccule Ripples - Direct Observation of Ripple Migration Processes and Their Implications. *Geology, 37,* 483-486.

Schieber, J., Lazar, R., Bohacs, K., Klimentidis, R., Dumitrescu, M., & Ottmann, J. (2016). An SEM study of porosity in the Eagle Ford Shale of Texas—Pore types and porosity distribution in a depositional and sequence-stratigraphic Context.

Shangmugam, G. (1997). The Bouma Sequence and the Turbidite Mind Set. *Earth-Science Reviews*, *42*, 201-229.

Slingerland, R., & Keen, T. R. (1999). Sediment transport in the Western Interior Seaway of North America: Predictions from a climate-ocean-sediment model.

Suter, J. R. (2006). Facies models revisited. *Special Publication – Society for Sedimentary Geology*, *84*, 1-527.

Talling, P. J., Masson, D. G., Sumner, E. J., & Malgesini, G. (2012). Subaqueous sediment density flows: depositional processes and deposit types. *Sedimentology*, *59*(7), 1937-2003.

Taylor, A. M., & Goldring, R. (1993). Description and analysis of bioturbation and ichnofabric. *Journal of the Geological Society*, *150*(1), 141-148.

Tyson, R. V. (2005). The" productivity versus preservation" controversy: cause, flaws, and resolution. *Special Publication-SEPM*, *82*, 17.

Vail, P. R., Mitchum Jr, R. M., & Thompson III, S. (1977). Seismic stratigraphy and global changes of sea level: Part 3. Relative changes of sea level from Coastal Onlap: section 2. Application of seismic reflection Configuration to Stratigraphic Interpretation.

Van Loon, A. J. (2009). Soft-sediment deformation structures in siliciclastic sediments: an overview.

Van Wagoner, J. C., Posamentier, H. W., Mitchum, R. M. J., Vail, P. R., Sarg, J. F., Loutit, T. S., & Hardenbol, J. (1988). An overview of the fundamentals of sequence stratigraphy and key definitions.

Van Wagoner, J. C., Mitchum, R. M., Campion, K. M., & Rahmanian, V. D. (1990). Siliciclastic sequence stratigraphy in well logs, cores, and outcrops: concepts for high-resolution correlation of time and facies.

Walker, R. G., Duke, W. L., & Leckie, D. A. (1983). Hummocky stratification: Significance of its variable bedding sequences: Discussion and reply: Discussion. *Geological Society of America Bulletin*, *94*(10), 1245-1249.

Williams, G. E. (1991). Upper Proterozoic tidal rhythmites, South Australia: sedimentary features, deposition, and implications for the earth's paleorotation.

Yawar, Z., & Schieber, J. (2017). On the origin of silt laminae in laminated shales. *Sedimentary Geology*, *360*, 22-34.

Yoshida, S., Willis, A., & Miall, A. D. (1996). Tectonic control of nested sequence architecture in the Castlegate Sandstone (Upper Cretaceous), Book Cliffs, Utah. *Journal of Sedimentary Research*, *66*(4), 737-748.

Zhu, Y., Bhattacharya, J. P., Li, W., Lapen, T. J., Jicha, B. R., & Singer, B. S. (2012). Milankovitch-scale sequence stratigraphy and stepped forced regressions of the Turonian Ferron Notom Deltaic Complex, South-central Utah, USA. *Journal of Sedimentary Research*, *82*, 723-746.

Appendix: Photomicrographs for Samples 3-10 and SEM images of Sample 1-10

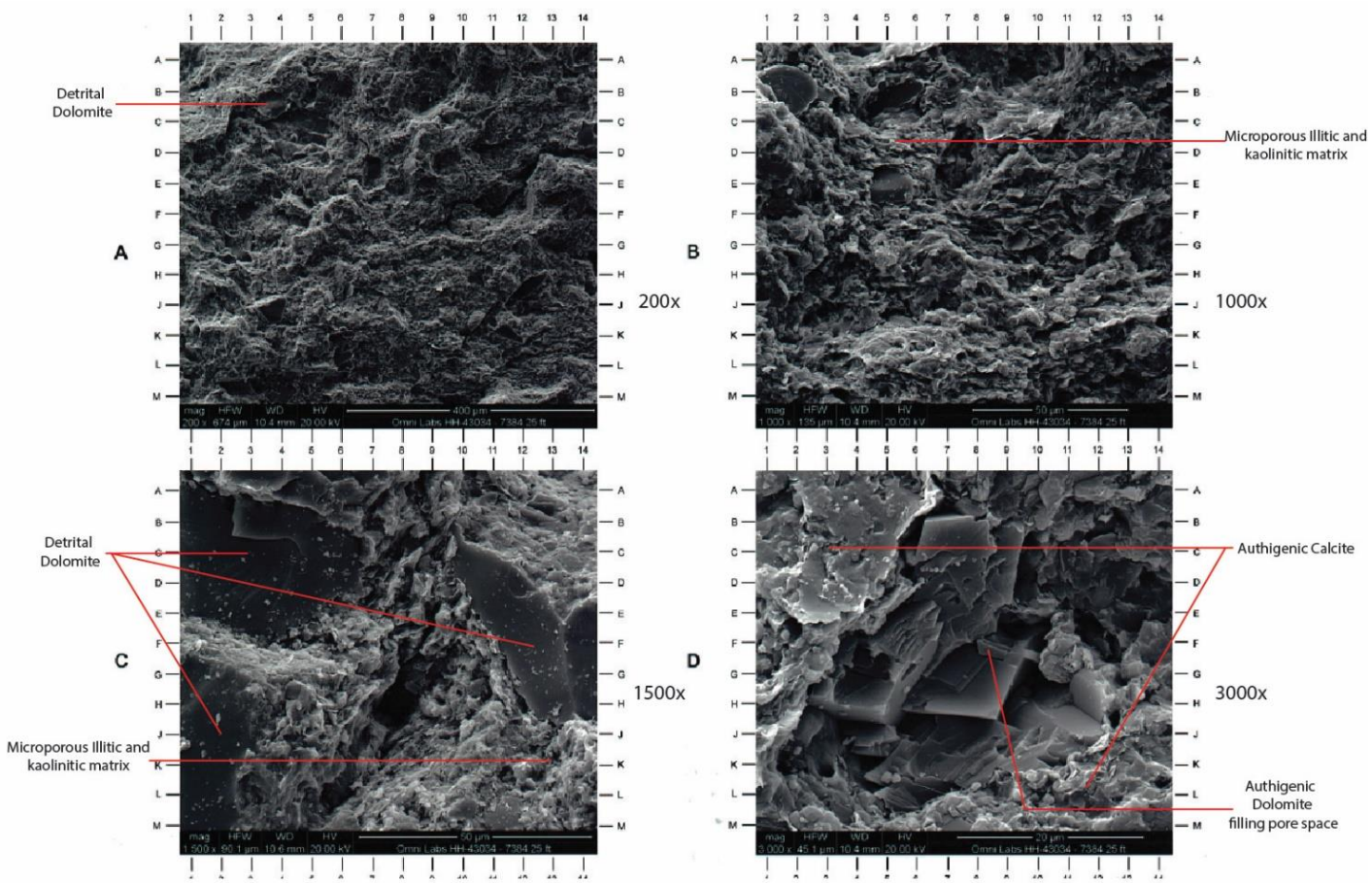

Fig. 1. Sample 1. SEM images of the thin section used in the photomicrograph at different magnifications.

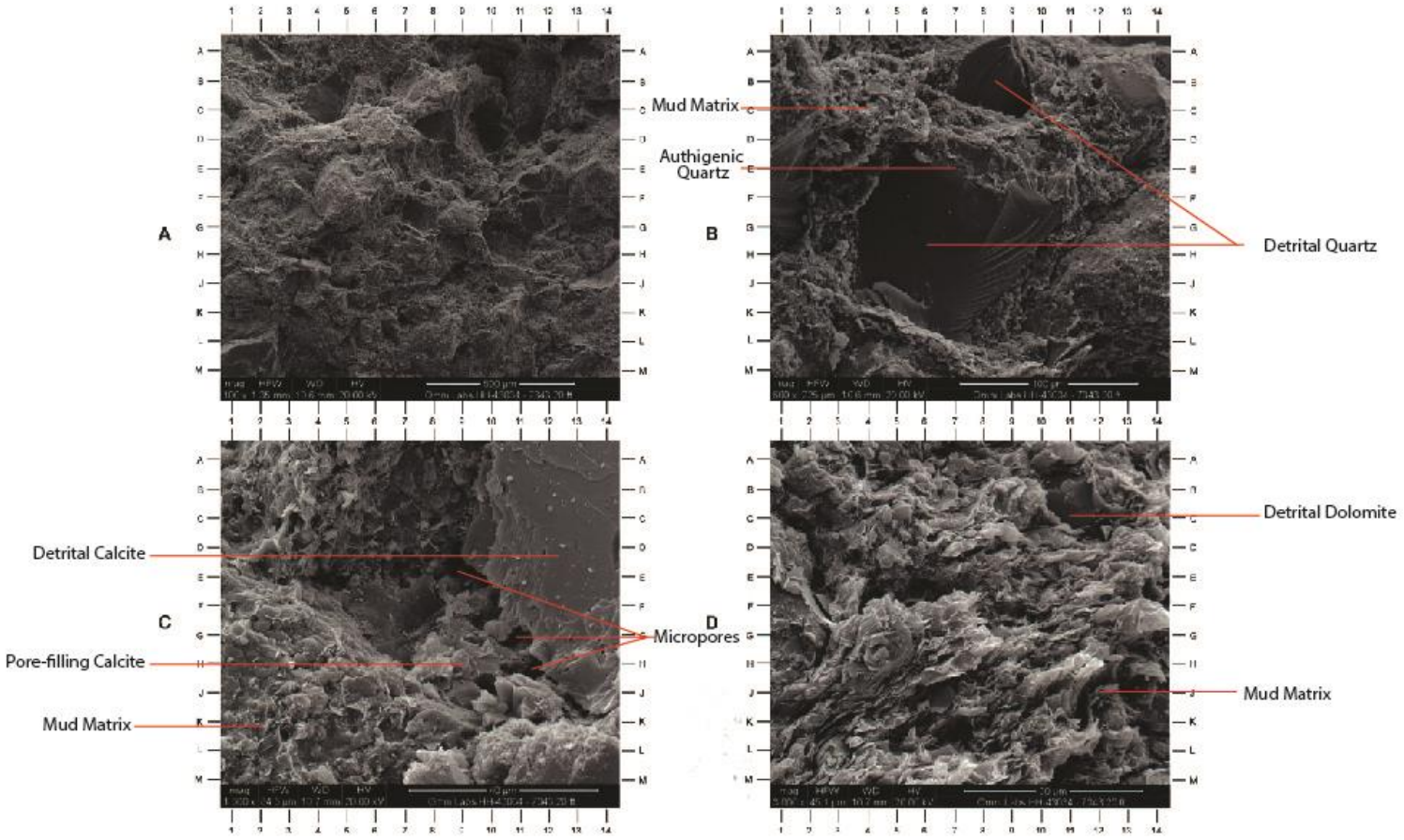

Fig. 2. Sample 2. SEM images of the thin section used in the photomicrograph at different magnifications.

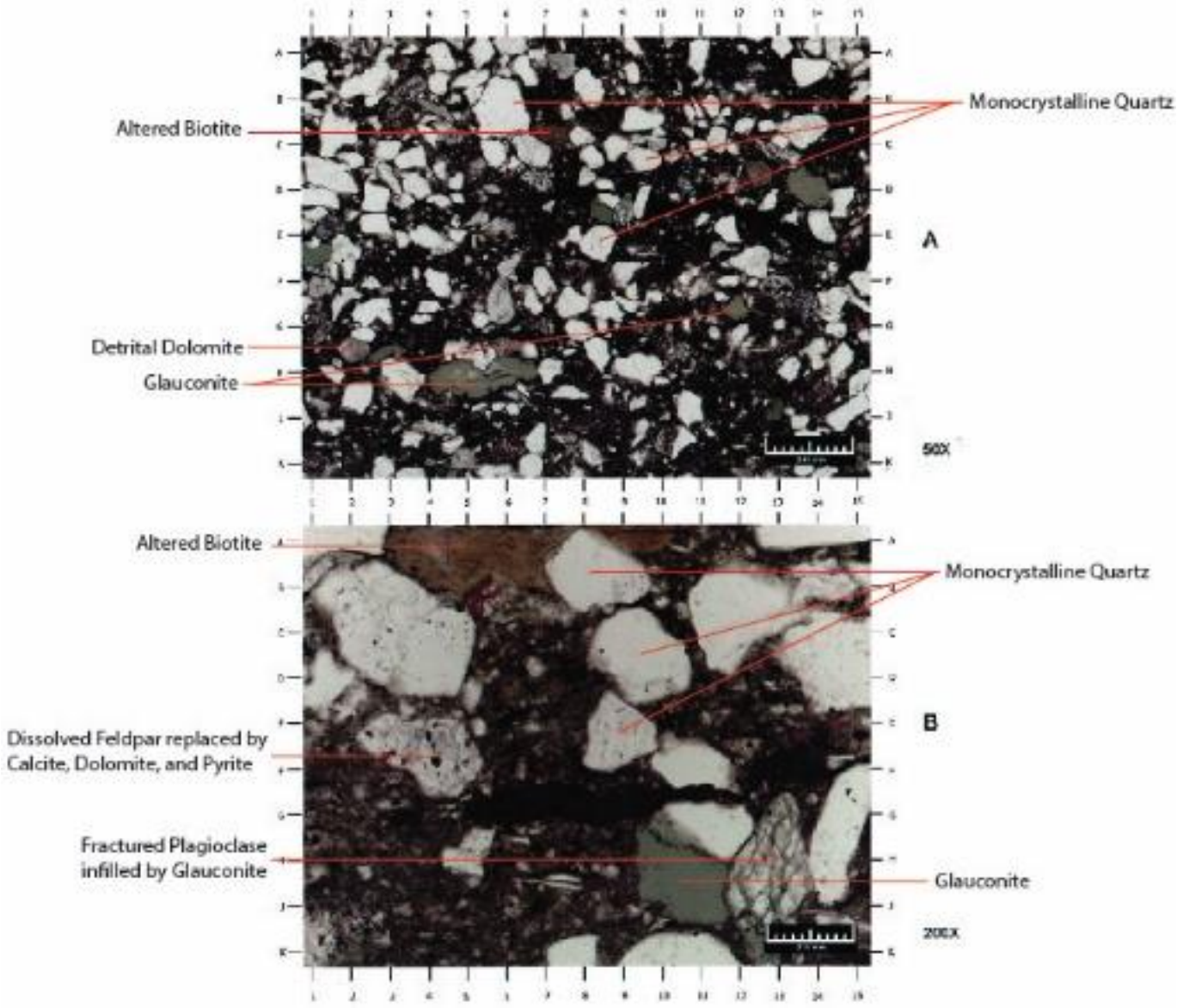

Fig. 3. Sample 3. Plain light photomicrographs of a thin section in parasequence 24. A general view is at the top and detailed view is at the bottom.

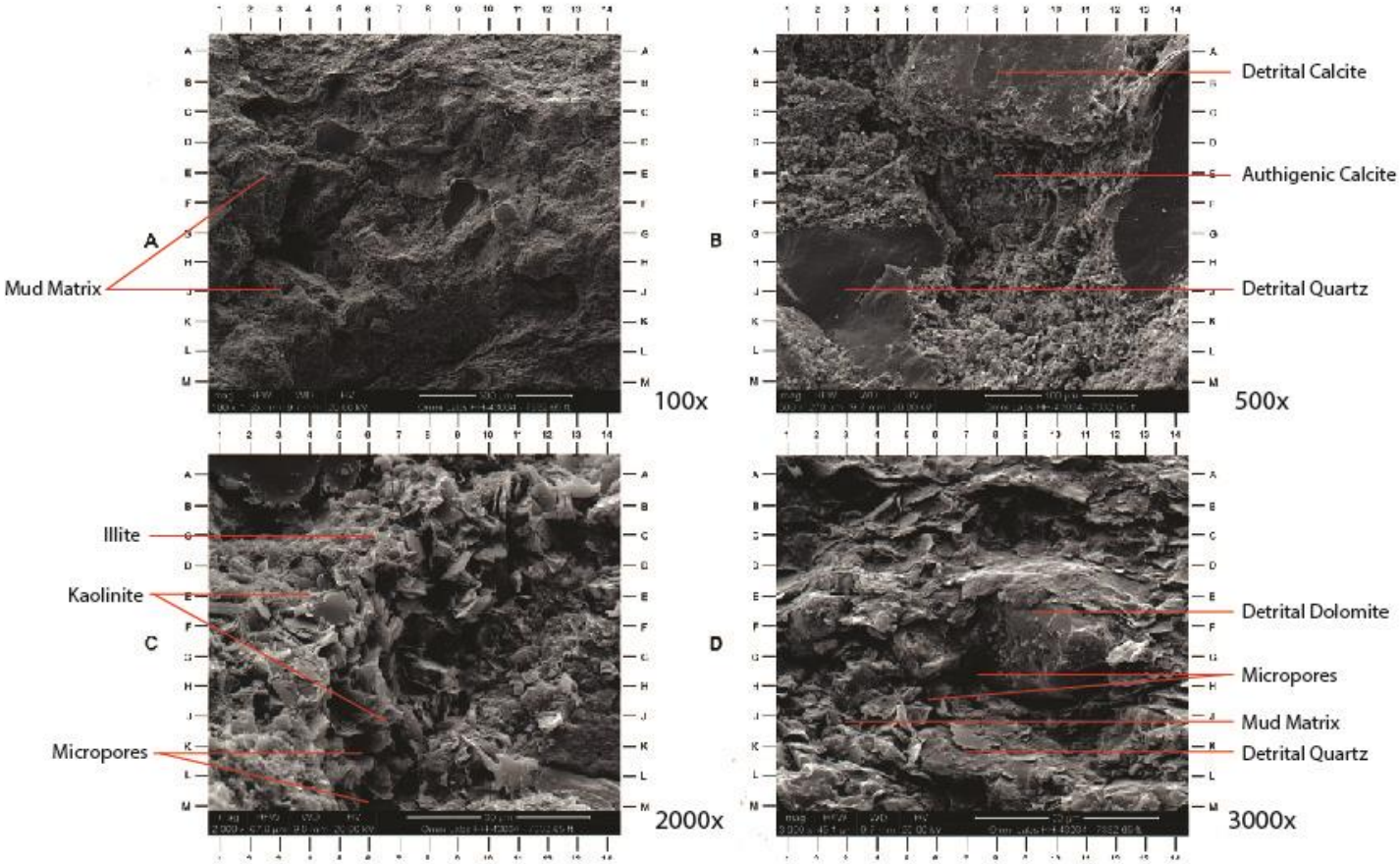

Fig. 4. Sample 3. SEM images of the thin section used in the photomicrograph at different magnifications

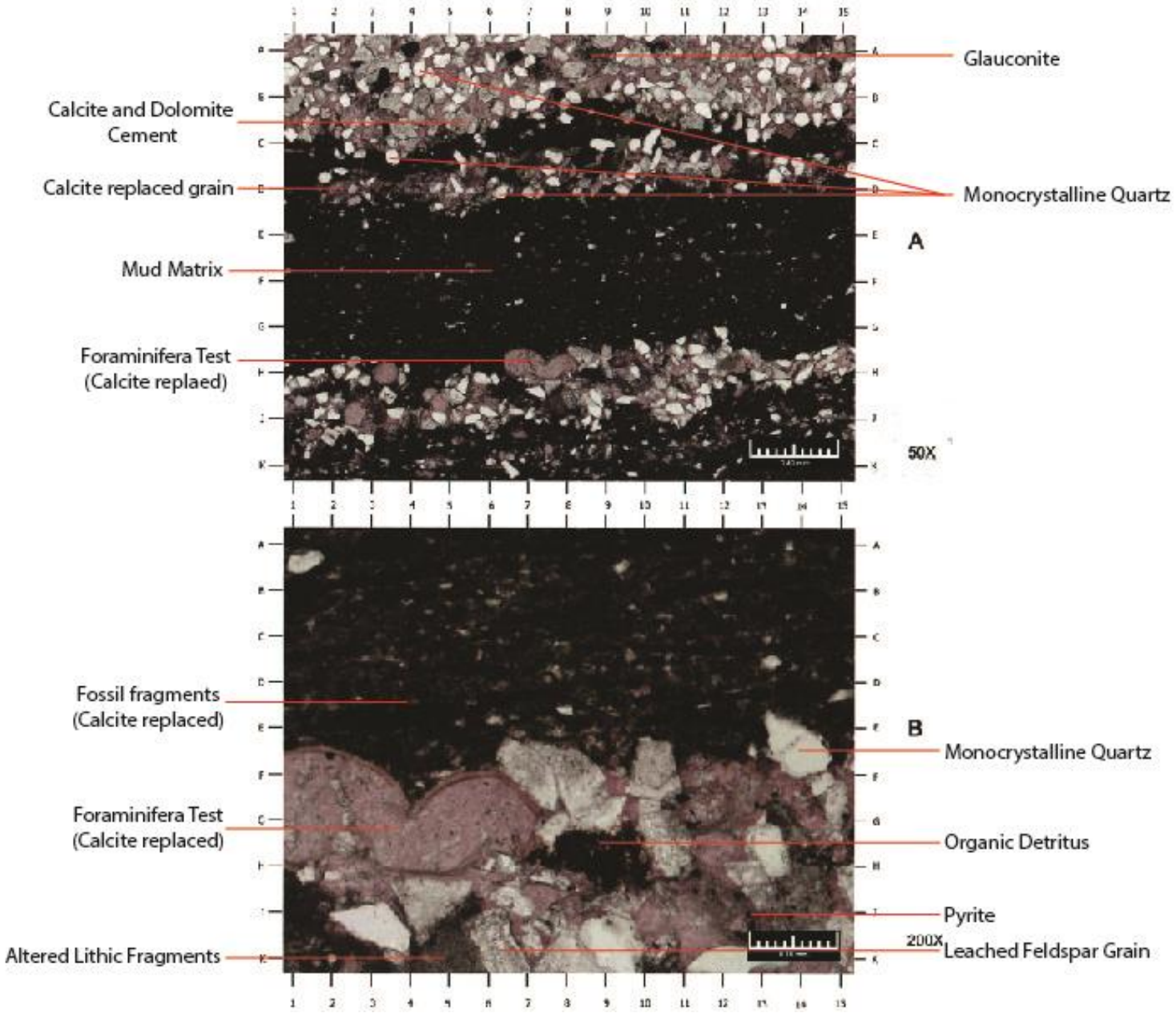

Fig. 5. Sample 4. Plain light photomicrographs of a thin section in parasequence 30. A general view is at the top and detailed view is at the bottom.

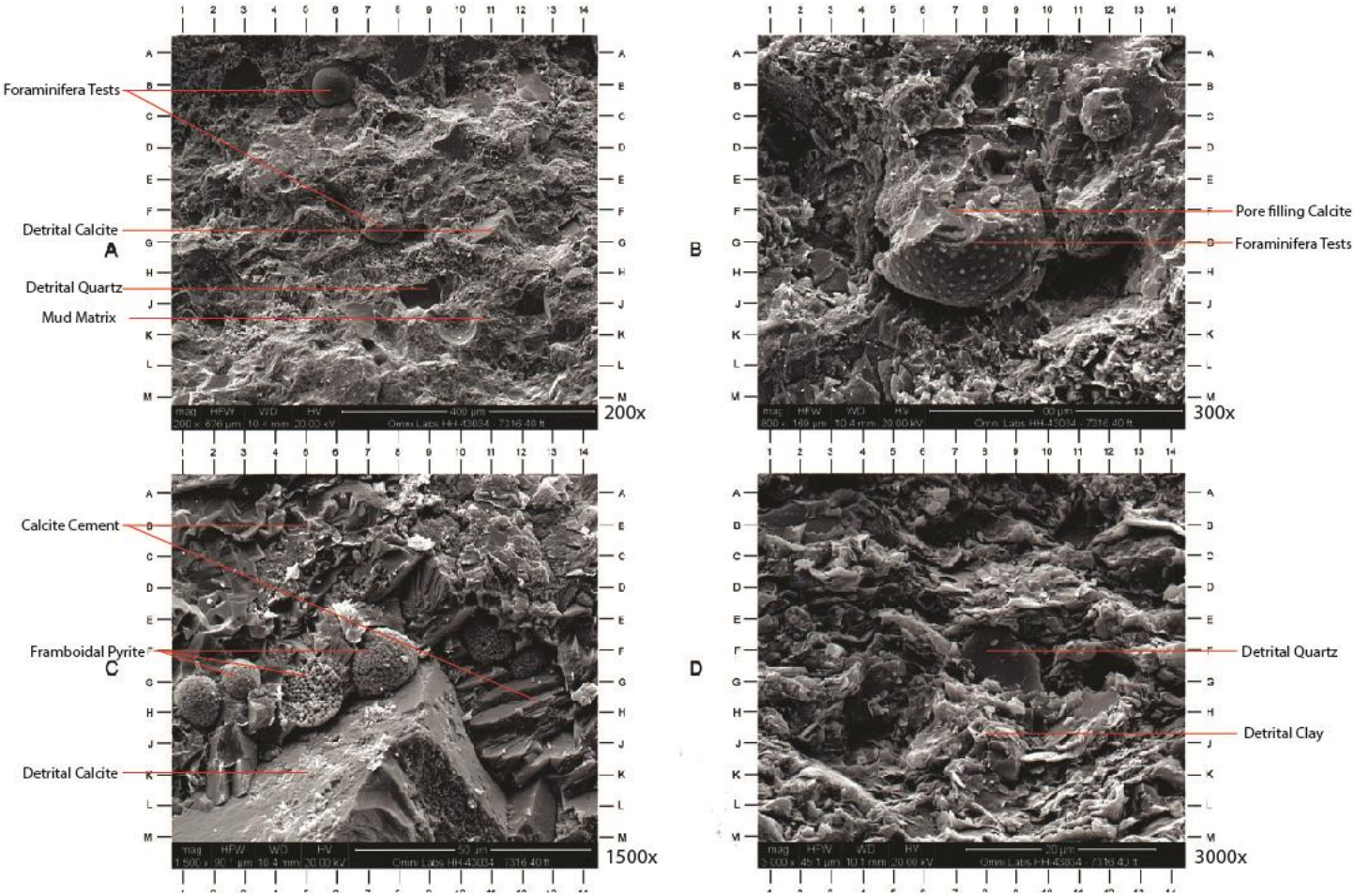

Fig. 6. Sample 4. SEM images of the thin section used in the photomicrograph at different magnifications.

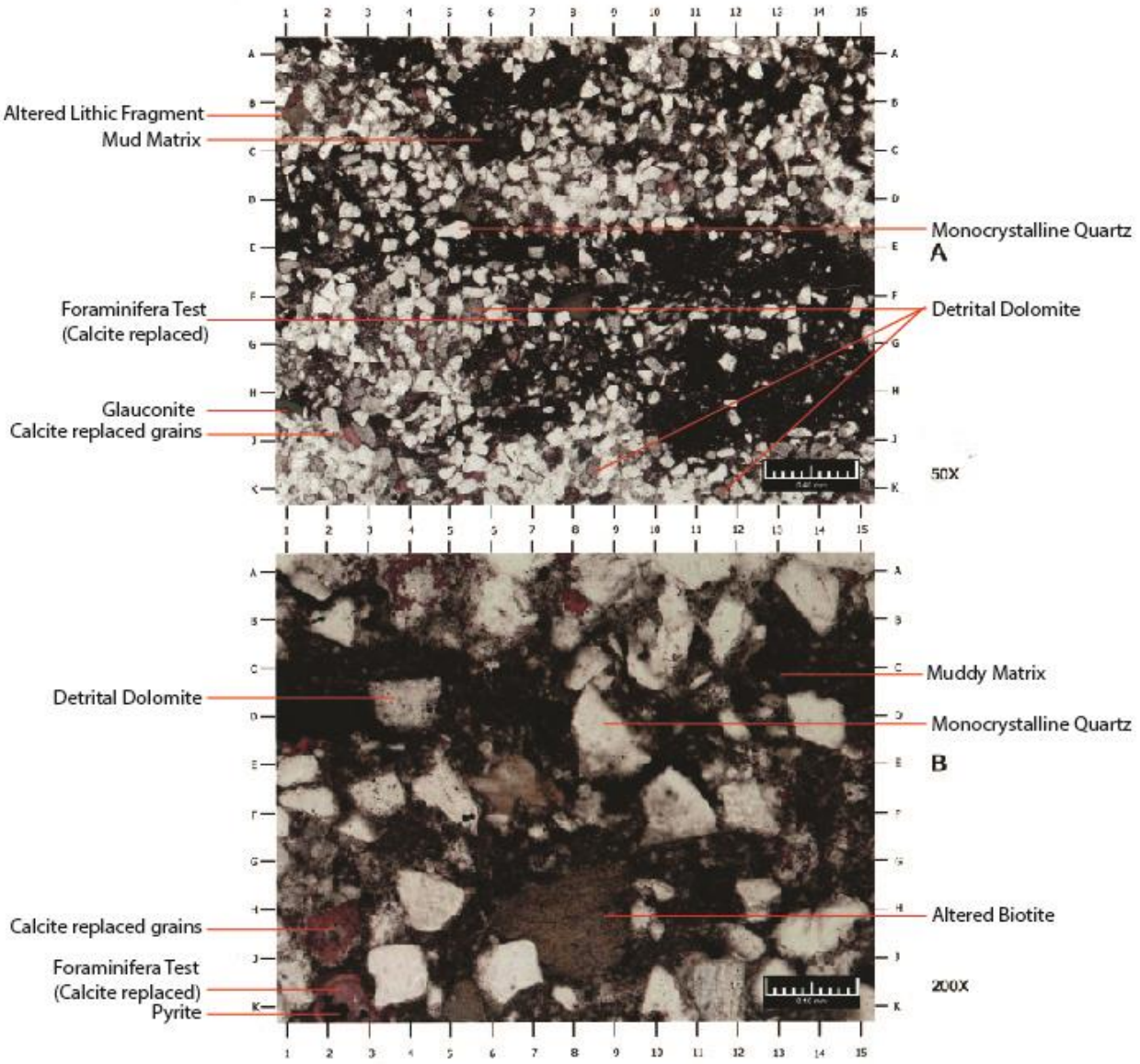

Fig. 7. Sample 5. Plain light photomicrographs of a thin section in parasequence 33. A general view is at the top and detailed view is at the bottom.

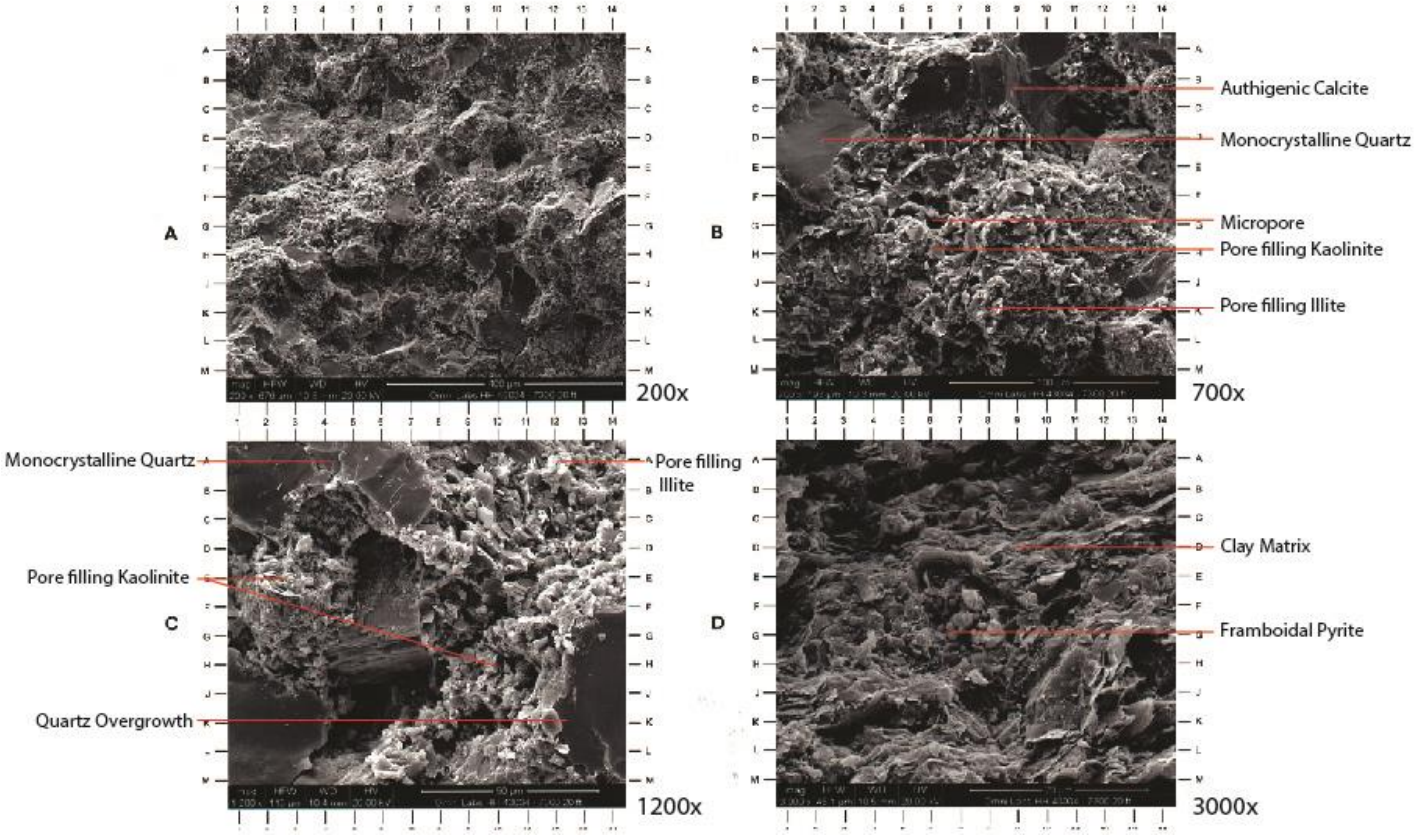

Fig. 8. Sample 5. SEM images of the thin section used in the photomicrograph at different magnifications.

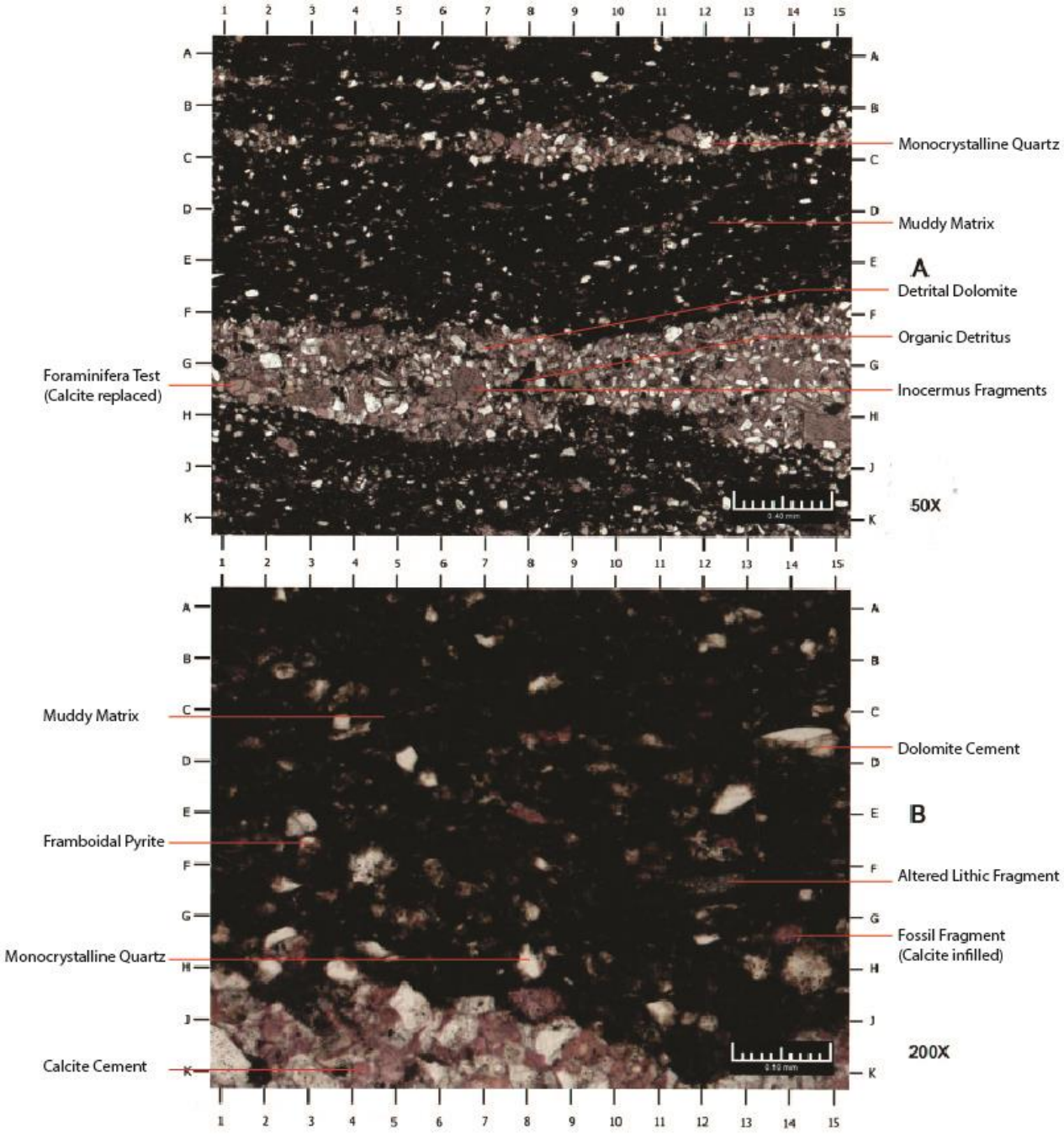

Fig. 9. Sample 6. Plain light photomicrographs of a thin section in parasequence 43. A general view is at the top and detailed view is at the bottom

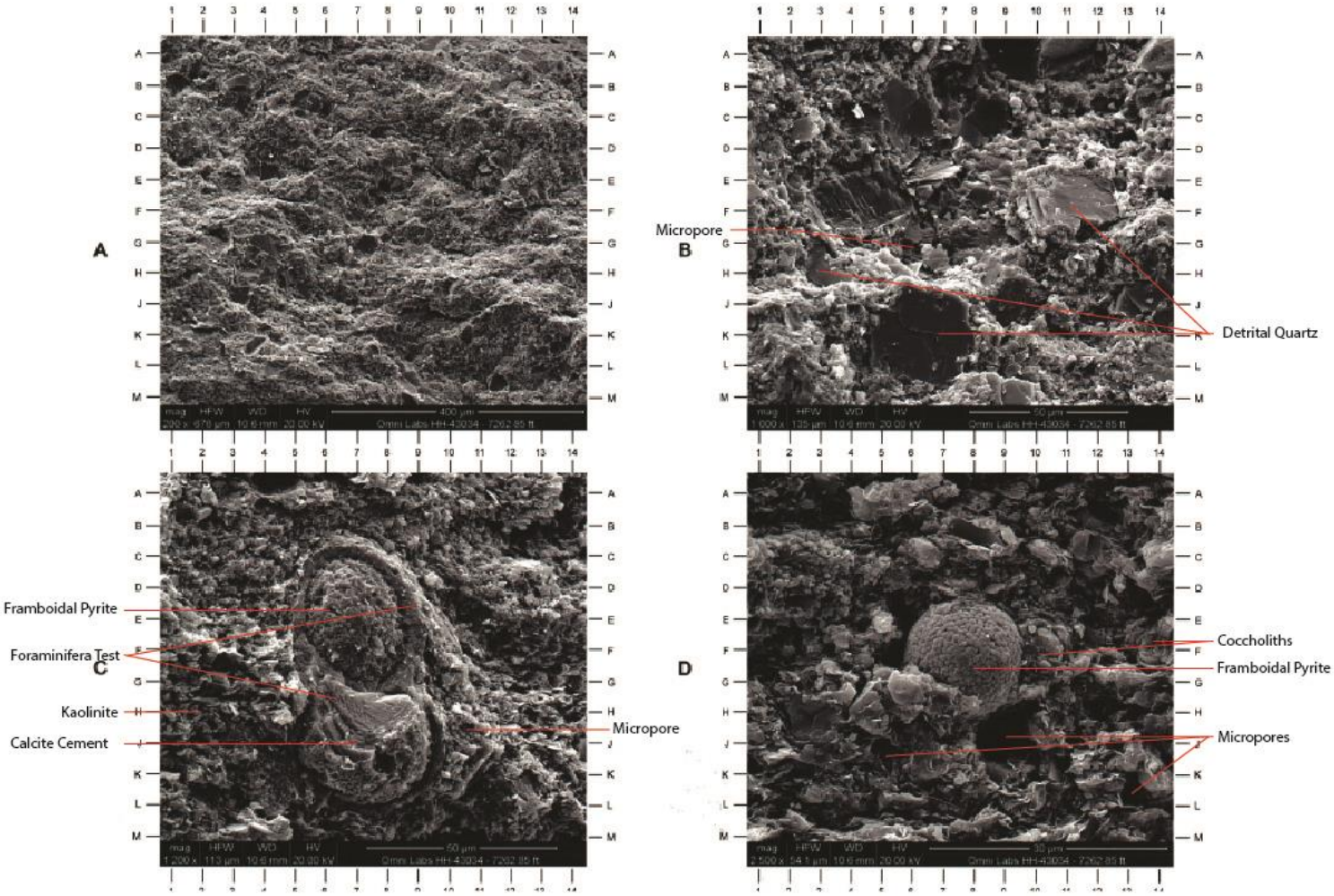

Fig. 10. Sample 6. SEM images of the thin section used in the photomicrograph at different magnifications.

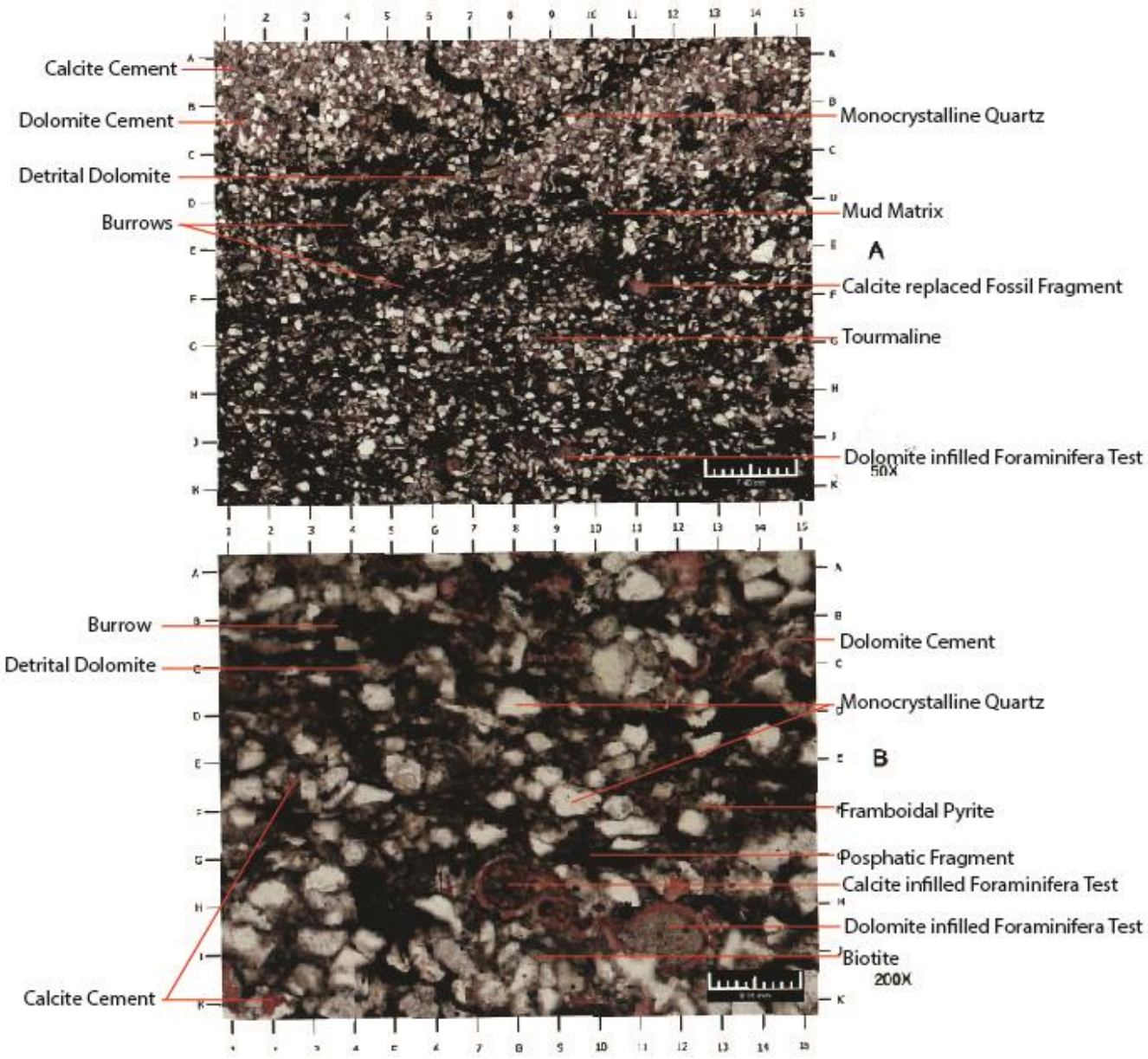

Fig. 11. Sample 7. Plain light photomicrographs of a thin section in parasequence 54. A general view is at the top and detailed view is at the bottom

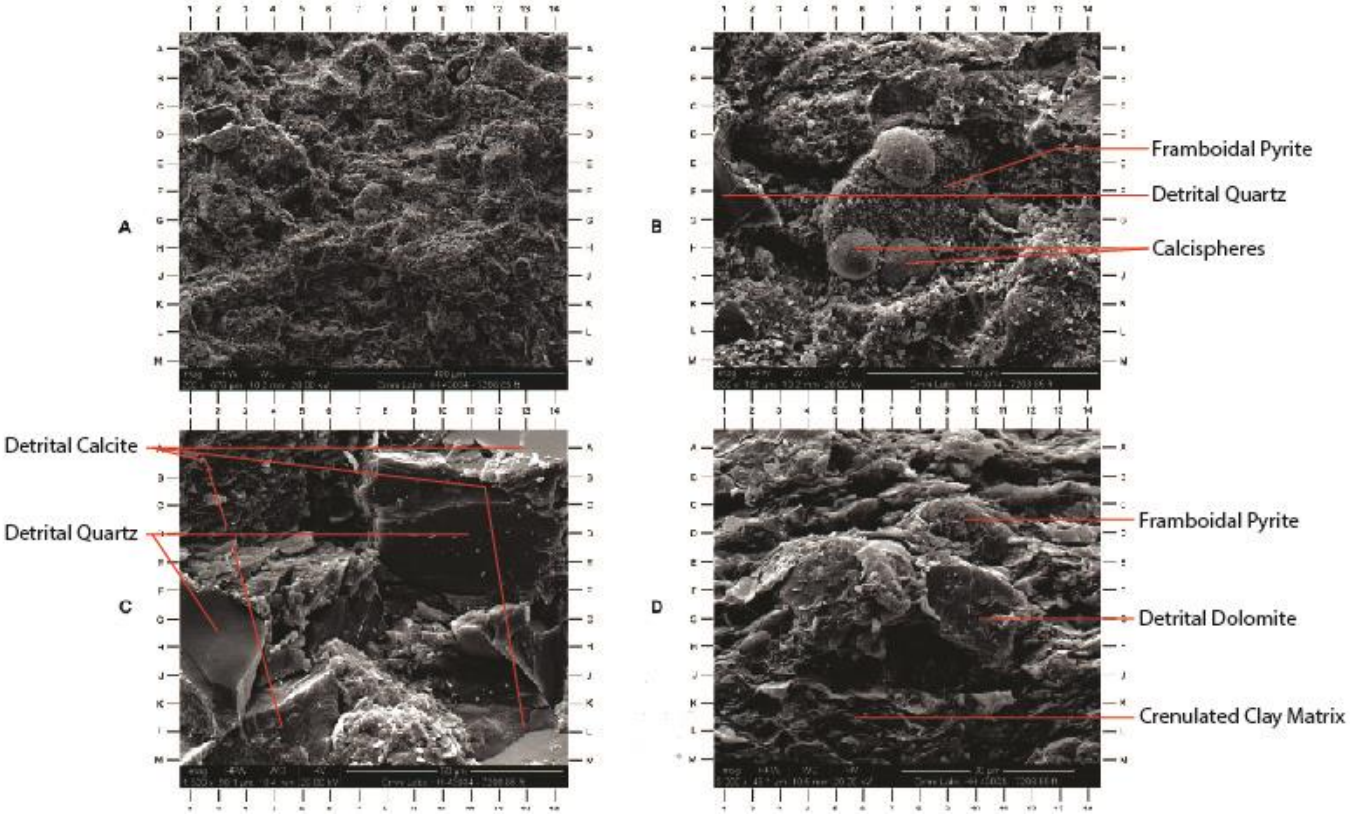

Fig. 12. Sample 7. SEM images of the thin section used in the photomicrograph at different magnifications.

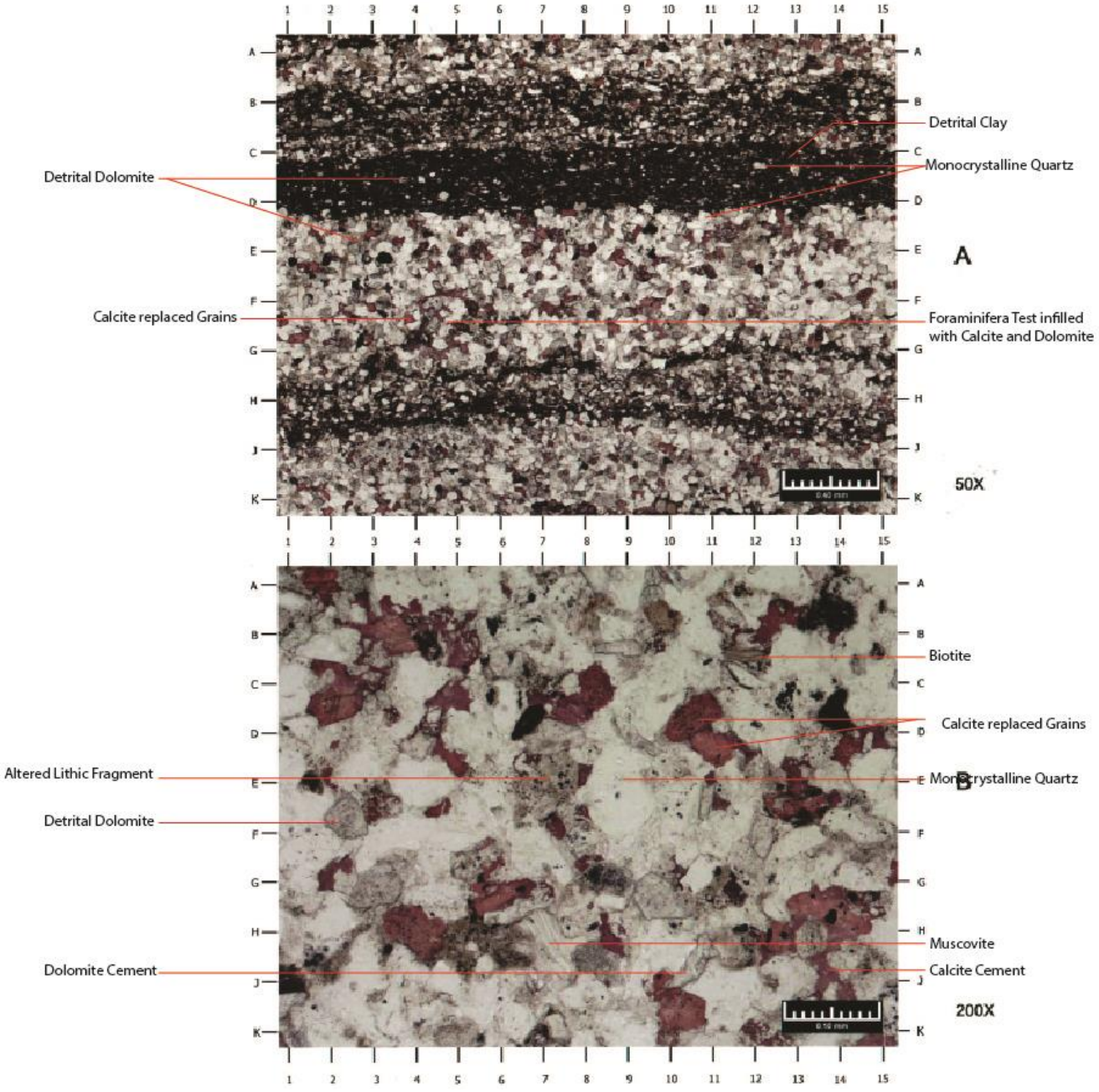

Fig. 13. Sample 8. Plain light photomicrographs of a thin section in parasequence 80. A general view is at the top and detailed view is at the bottom.

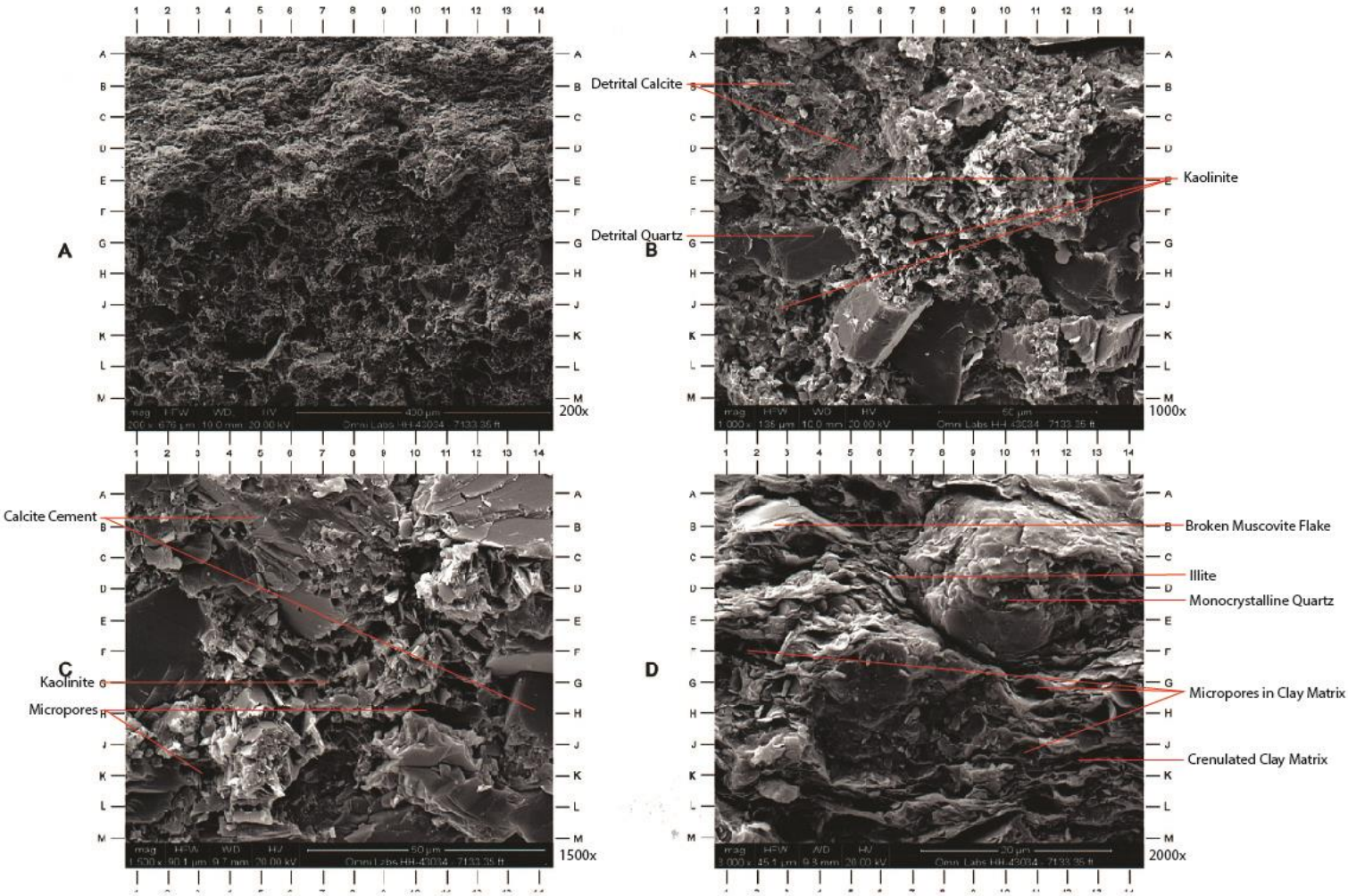

Fig. 14. Sample 8. SEM images of the thin section used in the photomicrograph at different magnifications

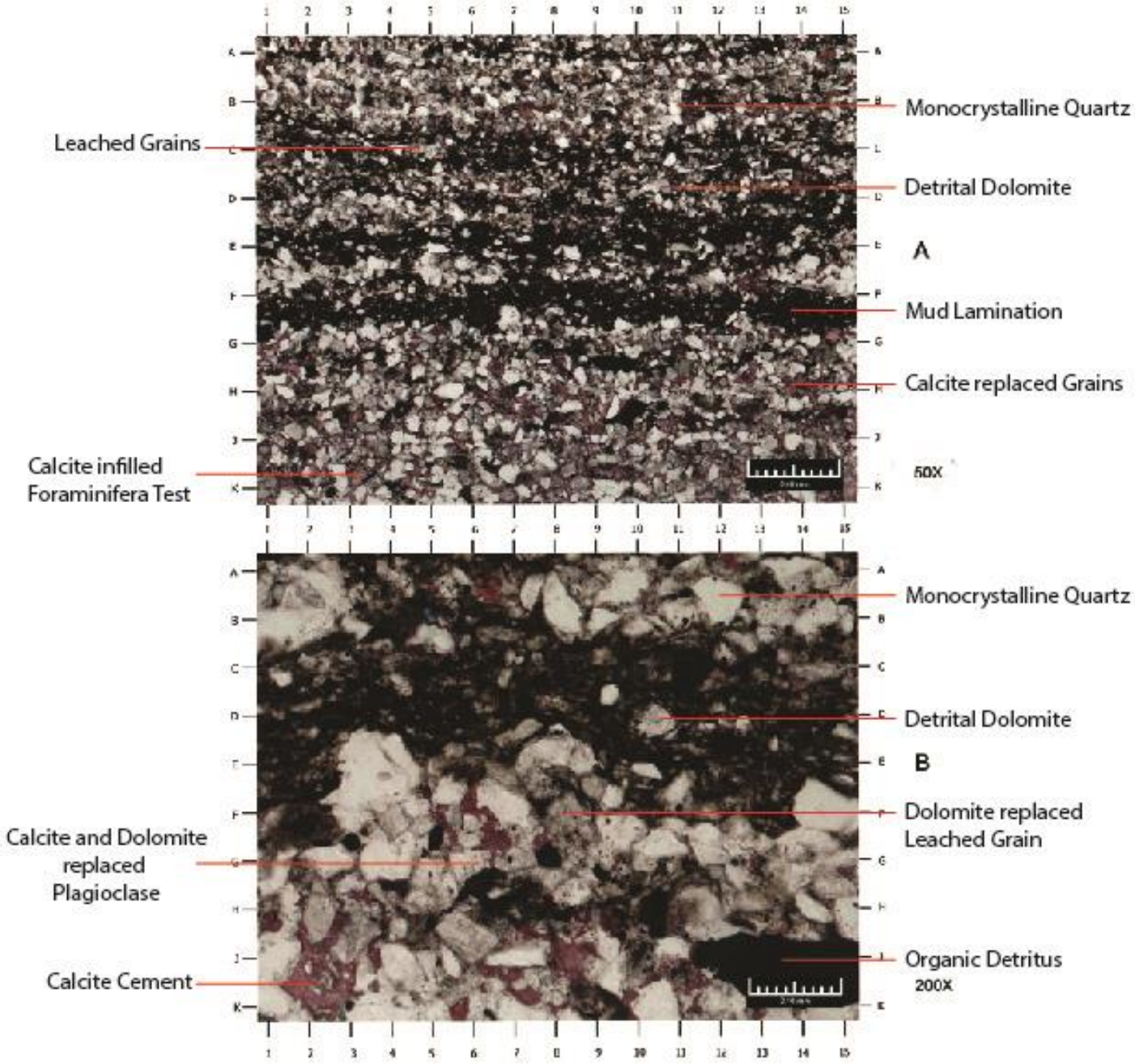

Fig. 15. Sample 9. Plain light photomicrographs of a thin section in parasequence 88. A general view is at the top and detailed view is at the bottom.

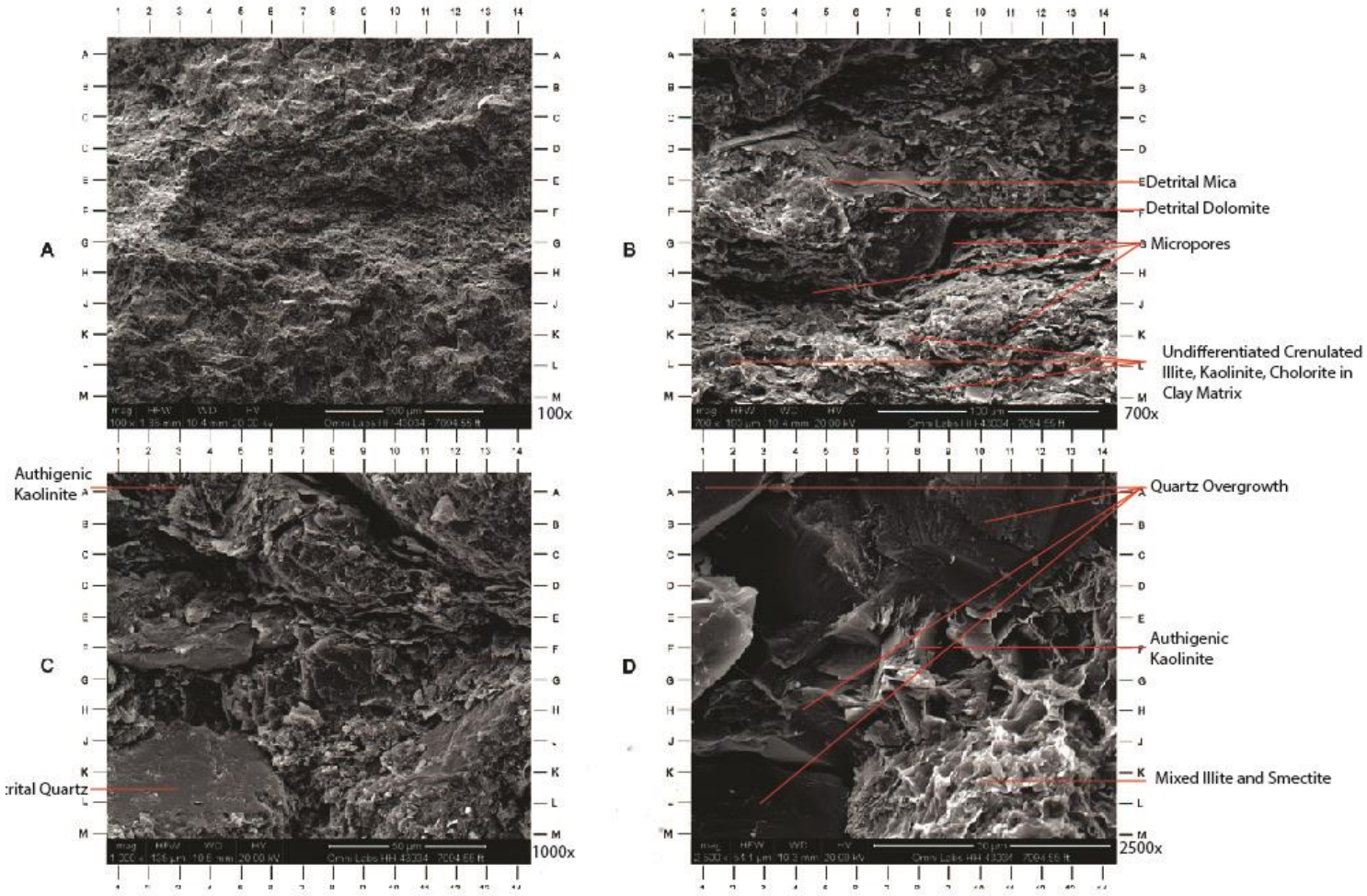

Fig. 16. Sample 9. SEM images of the thin section used in the photomicrograph at different magnifications.

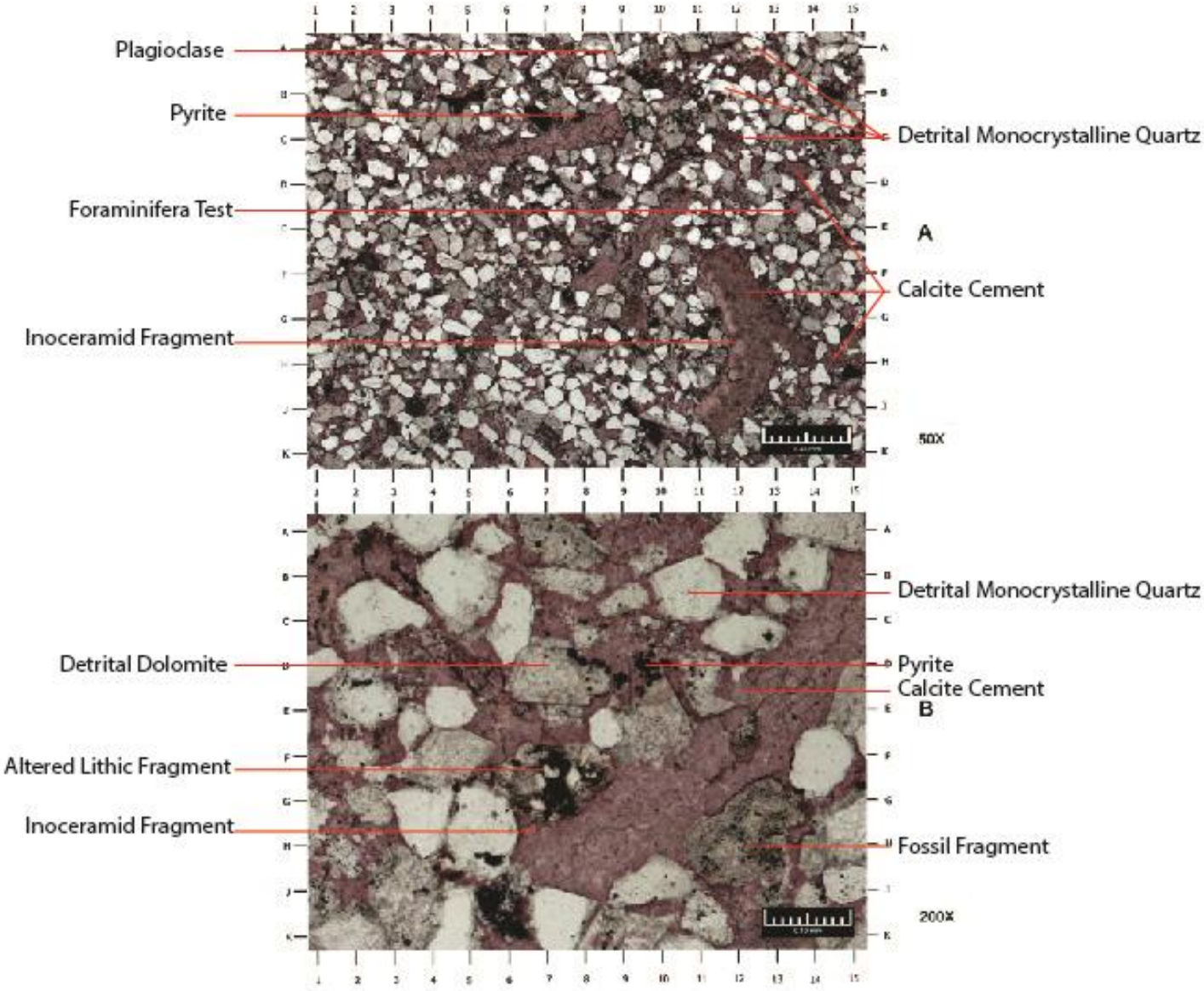

Fig. 17. Sample 10. Plain light photomicrographs of a thin section in parasequence 89. A general view is at the top and detailed view is at the bottom.

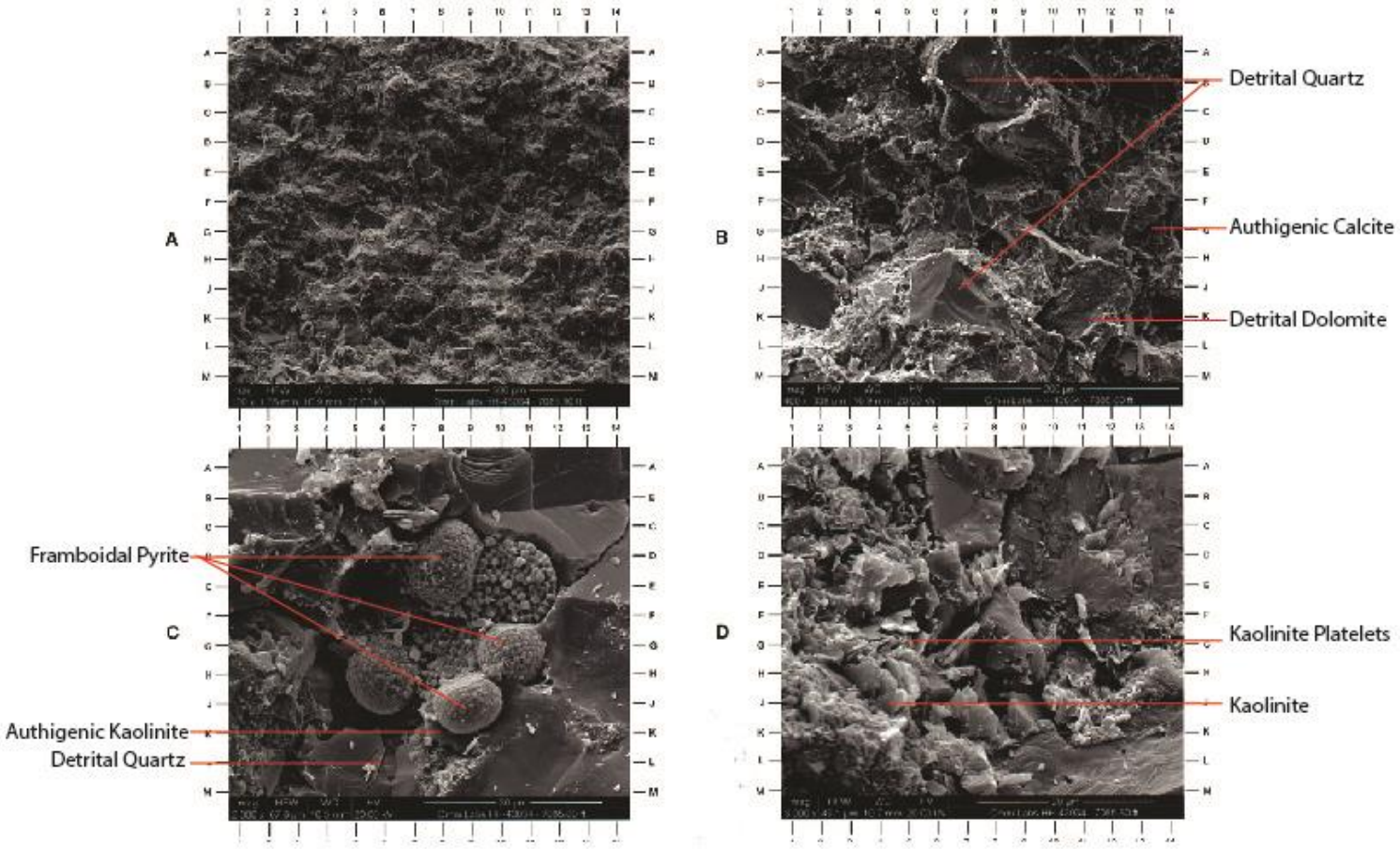

Fig. 18. Sample 10. SEM images of the thin section used in the photomicrograph at different magnifications.